UNIVERSIDADE ESTADUAL DE CAMPINAS
Instituto de Física Gleb Wataghin

Débora de Paiva Magalhães

Study and Characterization via Monte Carlo Simulation of Ionizing Radiation Damages in Hybrid Pixel Detectors

Estudo e Caracterização via Simulação Monte Carlo de Danos De Radiação Ionizante em Detectores de Pixel Híbrido

CAMPINAS
2018

Débora de Paiva Magalhães

Study and Characterization via Monte Carlo Simulation of Ionizing Radiation Damages in Hybrid Pixel Detectors

Estudo e Caracterização via Simulação Monte Carlo de Danos de Radiação Ionizante em Detectores de Pixel Híbrido

Dissertação apresentada ao Instituto de Física Gleb Wataghin da Universidade Estadual de Campinas como parte dos requisitos exigidos para a obtenção do título de mestra em Física, na área de Física Aplicada.

Dissertation presented to the Gleb Wataghin Institute of Physics of the University of Campinas in partial fulfillment of the requirements for the degree of Master, in the area of Applied Physics.

Supervisora/Orientadora: Alessandra Tomal

Este exemplar corresponde à versão final da dissertação defendida pela aluna Débora de Paiva Magalhães, e orientada pela Profa. Dra. Alessandra Tomal.

CAMPINAS

2018

Agência(s) de fomento e nº(s) de processo(s): Não se aplica.

Ficha catalográfica
Universidade Estadual de Campinas
Biblioteca do Instituto de Física Gleb Wataghin
Lucimeire de Oliveira Silva da Rocha - CRB 8/9174

M27s

Magalhães, Débora de Paiva, 1990-
Study and characterization via Monte Carlo simulation of ionizing radiation damages in hybrid pixel detectors / Débora de Paiva Magalhães. – Campinas, SP : [s.n.], 2018.

Orientador: Alessandra Tomal.
Dissertação (mestrado) – Universidade Estadual de Campinas, Instituto de Física Gleb Wataghin.

1. Transistores - Efeito da radiação. 2. Diagnóstico por imagem - Equipamento e acessórios. 3. Monte Carlo, Método de. I. Tomal, Alessandra, 1983-. II. Universidade Estadual de Campinas. Instituto de Física Gleb Wataghin. III. Título.

Informações para Biblioteca Digital

Título em outro idioma: Estudo e caracterização via simulação Monte Carlo de danos de radiação ionizante em detectores de pixel híbrido
Palavras-chave em inglês:
Transistors - Effect of radiation on
Diagnostic imaging - Equipment and supplies
Monte Carlo method
Área de concentração: Física
Titulação: Mestra em Física
Banca examinadora:
Alessandra Tomal [Orientador]
Eduardo Xavier Silva Miqueles
Varlei Rodrigues
Data de defesa: 23-03-2018
Programa de Pós-Graduação: Física

MEMBROS DA COMISSÃO JULGADORA DA DISSERTAÇÃO DE MESTRADO DE **DÉBORA DE PAIVA MAGALHÃES– RA 141204** APRESENTADA E APROVADA AO INSTITUTO DE FÍSICA "GLEB WATAGHIN", DA UNIVERSIDADE ESTADUAL DE CAMPINAS, EM 23 / 03 / 2018.

COMISSÃO JULGADORA:

- Profa. Dra. Alessandra Tomal – Orientadora – IFGW/UNICAMP
- Prof. Dr. Eduardo Xavier Silva Miqueles – CNPEM
- Prof. Dr. Varlei Rodrigues – IFGW/UNICAMP

OBS.: Informo que as assinaturas dos respectivos professores membros da banca constam na ata de defesa já juntada no processo vida acadêmica do aluno.

CAMPINAS
2018

Aknowledgements

I would like to thank prof. Dr. Alessandra Tomal for all the support, council, guidance and friendship through this work.

Prof. Dr. Jean Rinkel for suggestions and collaboration during the work.

Professors Varlei Rodrigues, Sandro Guedes and Mario Antonio Bernal Rodriguez for evaluating the project and the presentation during the previous phases of the master program.

The Brazilian Synchrotron Light Laboratory (LNLS), part of the Brazilian Center for Research in Energy and Materials (CNPEM) and funded by the Brazilian Ministry of Science, Technology, Innovations and Communications, and specially the X-ray Imaging Beamline staff and the Detectors Group and collaborators, which have provided the means for executing the experiments.

Rodrigo Massera, for the precious help with the experiment phase during the beam-time shifts, and various advice throughout the master's period.

My beloved friends and family for the emotional support and for reinforcing my belief in myself.

Resumo

Detectores de pixel híbrido vêm se consolidando como uma das melhores tecnologias para imagem de raios X, abordando técnicas de síncrotron e aplicações médicas. Em ambas aplicações, falhas do detector podem resultar em graves perdas de dados. No caso de energias mais altas, onde a eficiência do sensor é reduzida, a própria radiação incidente no sensor pode ser parcialmente transmitida, atingindo a eletrônica de leitura de cada pixel. No caso de aplicações síncrotron, a intensidade da radiação utilizada é cada vez mais alta, comprometendo a vida útil do detector. Este trabalho visou compreender os fenômenos relacionados ao efeito da radiação nas imagens, estabelecer padrões nas imagens, bem como relacionar quantitativamente a dose depositada com os danos nos dados fornecidos pelo detector. Dessa forma buscou-se estabelecer limites para garantia da qualidade dos dados para as diversas aplicações, bem como a frequência de possíveis procedimentos de manutenção periódica para garantir a melhor performance do detector.

A dose nas camadas de óxido dos transistores CMOS foi obtida via simulação Monte Carlo, utilizando o código PENELOPE. Essa grandeza foi escolhida uma vez que há um consenso na literatura de que o fenômeno relacionado aos danos na faixa de energia considerada de 2 a 100 keV corresponde à deposição de dose nessas camadas. O fenômeno de detecção por um detector pixelado foi modelado com detalhes no código, acrescentando efeitos de dispersão de cargas no sensor, para comparação com a imagem experimental e validação da simulação da dose. Esta correção permitiu uma comparação entre imagem e espectro obtidos experimentalmente com os resultantes da simulação Monte Carlo, comprovando a viabilidade do uso da dose depositada obtida através da simulação de Monte Carlo como uma estimativa do valor da dose depositada neste material.

Foram realizados experimentos de baixa dose (809 ± 6 Gy) e alta dose (6230 ± 20 Gy), utilizando como detector um chip Medipix3RX com sensor de silício de 200 μm. Foi possível estabelecer uma métrica para avaliação dos efeitos de doses baixas, que se provaram recuperáveis com o tempo e através de uma nova equalização. Para as altas doses foram reconhecidos 5 padrões visuais de danos e estabelecidas hipóteses para compreender seus diferentes comportamentos. Foi verificado um surgimento de danos visíveis a partir de 2616 ± 13 Gy, e calculada uma garantia de pelo menos 90% de pixels saudáveis até 3746 ± 23 Gy. Foi possível também obter uma estimativa quantitativa da escala de tempo da recuperação do detector: metade dos pixels saturados se recuperaram em 110.4 ± 1.3 minutos.

Palavras-chave: detectores de pixel híbrido, danos de radiação, simulação Monte Carlo.

Abstract

Hybrid pixel detectors are being consolidated as one of the best approaches for X-ray imaging techniques, addressing synchrotron and medical applications. In both applications, detector failures can result in severe data loss. The radiation incident on the sensor, in the case of higher energies and smaller efficiency, can be partially transmitted by the sensor, reaching the reading electronics of each pixel, which is located behind it. In the case of the modern synchrotron applications, this radiation tends to high intensities, compromising the detector's life cycle. This work aimed to understand the phenomena behind the effect of radiation on image data, recognize patterns among the possible effects and quantitatively relate the deposited dose with damages in the data provided by the detector, seeking to establish limits for a data quality assurance for the various applications, as well as the frequency of possible maintenance procedures to ensure the best performance of the detector.

The dose values in the oxide layers of the CMOS transistors were obtained through Monte Carlo simulation, based on the PENELOPE code. This parameter was chosen once there is a consensus in the literature that the phenomena related to damage in the considered energy range of 2 to 100 keV corresponds to dose deposition in these layers. The effects of charge dispersion in the sensor, which are relevant in pixelated detectors, were implemented in the code. This correction enabled a comparison between the experimentally obtained image and detected spectrum with the ones resulting from the Monte Carlo simulation. Thus, it was possible to verify their correlation and support the feasibility of using the deposited dose obtained via Monte Carlo simulation as an estimation of the deposited dose value.

Low dose (809 ± 6 Gy) and high dose (6230 ± 20 Gy) experiments were performed at a Medipix3RX single chip detector, bonded to a 200 μm thick silicon chip. It was possible to establish a metric to evaluate the low dose effects, which proved to be recoverable through time. For high doses, different damage patterns were verified and hypotheses were made to understand their different behaviors. Visible damages were verified starting at 2616 ± 13 Gy, and a guarantee of at least 90% healthy pixels until 3746 ± 23 Gy was calculated. It was also possible to obtain a quantitative estimation of the detector recovery time scale: half of the saturated pixels were recovered at 110.4 ± 1.3 minutes.

Keywords: hybrid-pixel detectors, radiation damage, Monte Carlo simulation.

List of Figures

List of Tables

Abreviations List

ASIC Application Specific Integrated Circuit

BEOL Back End of Line

CCD Charge-Coupled Device

CERN European Organization for Nuclear Research

CMOS Complementary Metal-Oxide Semiconductor

CXRO Center of X-ray Optics

FEOL Front End of Line

FWHM Full-Width at Half-Maximum

Gy Dose unit: 1 Gy = 1 $joule/kg$

IMX X-ray Image Beamline

LNLS Brazilian Synchrotron Light Laboratory

MTF Modulation Transfer Function

STI Shallow Trench Isolation

Contents

Introduction

Hybrid pixel detectors are being consolidated as one of the best approaches for X-ray imaging techniques, addressing synchrotron and medical applications. This technology was initially developed for High Energy Physics applications like charged particle tracking, where its excellent spatial resolution and high signal-to-noise ratio would allow accurate determination of charged particle trajectories and reconstruction of decay vertices [1]. It aimed at associating an integrated circuit to a pixelated sensor. The main challenge was limiting the electronic circuit to the microsized pixel surface, since the integrated circuit was expected to include a complete electronic chain for each sensor pixel. This problem was solved by the CMOS technology scaling in the past years [2].

The new detector technology ability to count single photons or other ionizing radiation, and its excellent sensitivity, linearity and dynamic range, have represented an industrial breakthrough in comparison to CCD or CMOS cameras, and triggered the attention of scientists working in material sciences and biology [2]. This enthusiasm pushed the development of hybrid pixel circuits fully dedicated to the detection of X-rays, like Pilatus, XPAD and Medipix [2]. The capability of such devices to select photon energy has also proven to be exploited in biological and clinical imaging [3–5].

The Medipix3RX chip is a hybrid-pixel detector, based on an application-specific integrated circuit (ASIC) bonded pixel-to-pixel to a semiconductor sensor. It has been designed by a collaboration of several laboratories formed in 2005 and hosted by the European Organization for Nuclear Research - CERN [6], aiming at medical imaging applications like computed tomography [7]. It is now used in several laboratories around the world, other then CERN itself [8–12], reinforcing the broad scientific interest on its characterization and improvement. Its vast applicability is related to its innovative attributes: it can count photons directly until 24 bits and eliminate completely the electronic noise by using energy thresholds; has a inter-pixel

communication for correcting charge dispersion effects in the sensor; has a competitive pixel size (55 μm square); can be configured in 4 different gain modes; discriminates photon energies in up to 8 channels; and has a continuous read-write mode, eliminating completely the readout time [13].

The Brazilian Synchrotron Light Laboratory - LNLS has taken part of the Medipix Collaboration by the end of 2012. It has become the main focus of the Detectors Group, founded at 2013 in order to bring to Brazilian community steps from the X-ray detectors chain production process. Besides, this group aim to deal with the challenges provided by the new Brazilian synchrotron light source currently in development, SIRIUS.

SIRIUS[1] is a synchrotron light source of 3 GeV, designed to be one of the most advanced in the world. It's ultra-low emittance (0.28 nm.rad) and high brilliance will drive the accomplishment of competitive experiments, opening new perspectives for research in fields like materials science, structural biology, nanoscience, physics, environmental and earth sciences, cultural inheritance, among others [14]. In Latin America, SIRIUS construction represents a jump for the future of synchrotron light.

The new source's high brilliance enables real time characterization techniques, to which is necessary a high time resolution detector, minimizing the readout time. Once it permits working with high energy ranges, it will make feasible macrometric sample applications, like rock tomography, that also demands larger detection areas and new sensor materials. Imaging techniques will demand higher spatial resolution, specially with the advent of coherent radiation. Due to its fast readout, small pixel size and other attributes, Medipix3RX chip was chosen for most part of the SIRIUS related applications. One of the challenges presented by the new source is dealing with high dose deposition in the detector. In hybrid pixel detectors, the electronics are necessarily connected behind the sensor, therefore faded to receive radiation dose. Also, smaller pixel sizes make the transistors more susceptible to charge trapping in the oxide layers, resulting from radiation ionization ("Narrow Channel Effect") [15].

Although Medipix3RX was developed considering a radiation-tolerant layout technique [16], significant transient and permanent errors were reported during synchrotron applications. Even transient errors are relevant to the synchrotron application, since such facility is required to

[1]The Sirius project is funded by the Brazilian Ministry of Science, Technology, Innovations and Communications.

work uninterruptedly. In medical applications, the main concern is to reduce the absorbed dose by the patient, a context in which fails and errors on images are inadmissible, once it would require the patient to be exposed twice [17]. Therefore, possible corrective solutions like annealing [18] and recovery periods don't fulfill the detectors main objectives.

This work aims to characterize and quantify radiation damages and their impact on image data, being part of a bigger context of knowledge building and detector's limitations definition, heading to the possibility of an overcome in order to explore this technology to its maximum.

The dissertation was divided in four main topics. Chapter 1 presents all the physical concepts and theory absorbed from the literature and applied to the project. Chapter 2 describes the methodology adopted for the work development, including the simulation of the detector, the experimental procedure and the parameters adopted for evaluating the damage. Chapter 3 shows the results, including the simulation validation and the experimental data. The fourth and last chapter exhibits the conclusion of the work, its application and suggestions of further research and implementations.

Chapter 1

Bibliographic Review

1.1 Principles of Radiation Interaction with Matter

The operation of a radiation detector relies on the interaction of the radiation with the detector material. The understanding of the response of a specific detector requires an analysis of the energy deposition of the radiation in matter.

The context of this work is focused on X-ray detection by hybrid pixel detectors. X-rays are an indirectly ionizing electromagnetic radiation: their energy range is limited above the minimum energy necessary to ionize an atom. The X-ray beam can also be described by the particle nature, being constituted by photons, quantized packets of light with no mass, but defined energy and momentum. There are mainly four interaction possibilities of X-rays in matter: photoelectric absorption, Rayleigh scattering, Compton scattering and pair production [19]. Figure 1.1 illustrates the four processes.

The photoelectric absorption effect is an X-ray interaction of a photon with a tightly bound orbital electron of an absorber atom. If the incident photon energy surpasses the bounding energy of an atom, it will be able to eject an electron, generating a free **photoelectron**, and disappearing in the process. The resulting vacancy from the emission of the photoelectron will be filled by a higher shell electron and the energy difference can be emitted as a characteristic photon or as an Auger electron [21].

The Rayleigh scattering is an elastic process: the X-ray photon interacts with an electron and is re-emitted with different momentum, but the same energy. This process does not transfer any energy to the irradiated material.

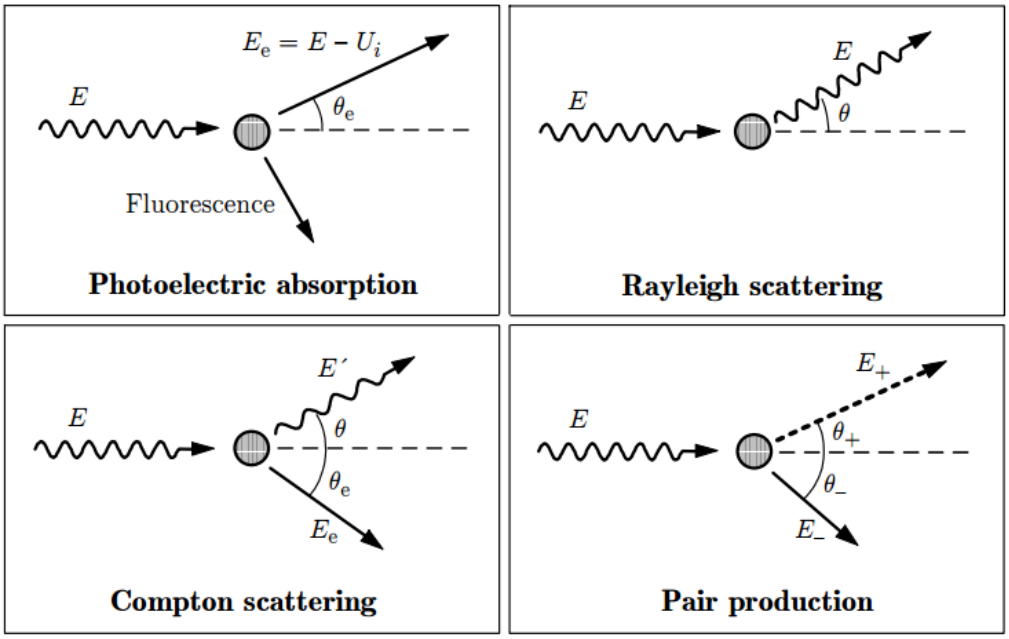

Figure 1.1: Four electromagnetic radiation interaction processes with matter. Obtained from [20].

The Compton scattering, on the other hand, is an inelastic collision. It implicates in partial energy loss to the recoiling electron in the form of kinetic energy, and the emitted photon will present a smaller energy than the incident photon.

The pair production phenomenon is characterized by the creation of an electron and a positron from the radiation incidence, and is energetically possible only if the incident energy exceeds twice the rest-mass energy of an electron (1.02 MeV) [19], even though the probability of this interaction remains very low until the incident energy reaches several MeV.

All the interaction processes, except for Rayleigh scattering, result in partial or complete energy transfer from the radiation to the charged particles in the material, generating detectable events [19] and being then relevant to the detection of radiation. Also, the application of this work will be focused on the X-ray range up to 100 keV, which do not contemplate the photon energy needed for electron-positron pairs generation effect.

The Beer-Lambert law, described in equation (1.1.1) relates the attenuation of radiation to the properties of the material through which it is traveling. The radiation intensity transmitted by the material is a function of the incident radiation intensity I_0 and an exponential function of the product between the linear attenuation coefficient of the material, $\mu(cm^{-1})$ for this specific radiation energy, and the thickness of matter being crossed, δ (cm). This law is an

approximation for the radiation transport through the material and does not consider secondary particles generated in the process.

$$I = I_0 \times e^{-\mu \times \delta} \tag{1.1.1}$$

The mass attenuation coefficient, defined as μ/ρ, where ρ is the mass density (g/cm^2), depends only on the composition of the material and is a normalized quantity for analyzing the material attenuation disregarding its density, being related to each interaction process:

$$\frac{\mu}{\rho} = \frac{(\sigma_{pe} + \sigma_{coh} + \sigma_{incoh})}{uA} \tag{1.1.2}$$

where σ_{pe} corresponds to the photoelectric cross-section, σ_{coh} to the coherent scattering cross-section (Rayleigh), σ_{incoh} to the incoherent cross-section (Compton), u is the atomic mass unit and A is the relative atomic mass of the target material [22]. The equation was simplified to include the expected interaction process for the 2 to 100 keV energy range.

The mass attenuation coefficient as a function of the photon energy for silicon is presented in Figure 1.2, obtained from the XMuDat software (Nowotny, 1998) with interaction cross section data from Boone and Chavez (1996). The contributions of each interaction process are specified by the individual cross-section, according to equation (1.1.2), which are related to their probability of occurrence.

For low photon energies, the main interaction process is the photoelectric interaction. The Compton scattering contribution becomes more important as the energy increases, overcoming the photoelectric contribution for energies above 60 keV. The total attenuation decreases drastically for higher energies, limiting the use of this material for detection of energies higher than 100 keV, where heavier materials (high-Z sensors) like cadmium telluride are applied [8, 23].

1.2 Principles on X-ray Detection

Although there are many different materials used for X-ray detection, like gas detectors or scintillators, this project application will focus on semiconductor sensors.

Materials can be classified in terms of their ability in conducting charge by the filling pattern of their energy bands. Metallic materials have a partially filled band, being able to constantly transport current. These electrons are weakly bonded to the surface by their work function,

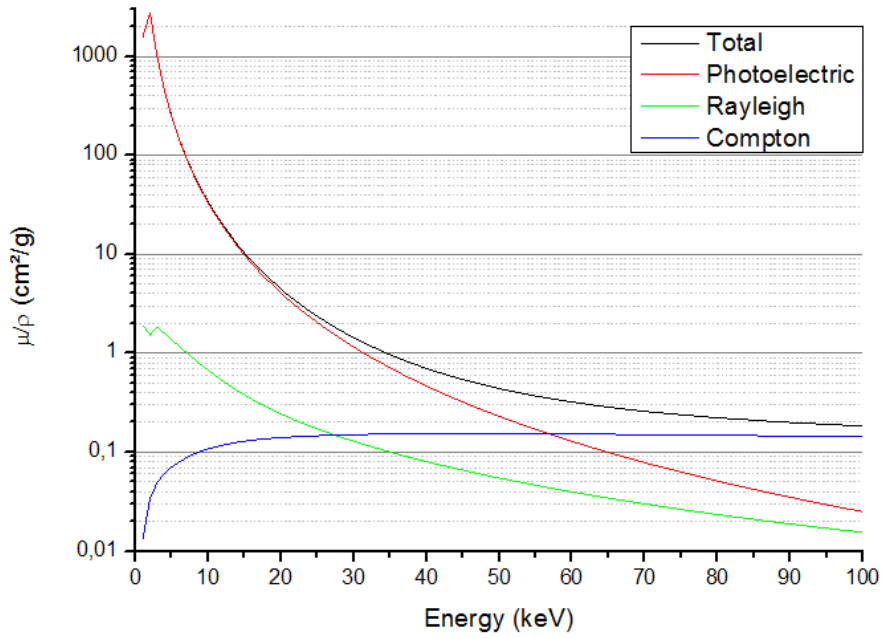

Figure 1.2: Log-scale graph of mass attenuation coefficient as a function of energy for Silicon, obtained with the XMuDat software (Nowotny, 1998) with interaction cross section data from Boone and Chavez (1996).

favouring the photoelectric event. In insulator materials, there is no band partially filled of electrons able to transport current at zero temperature. They are characterized by an energy gap E_g between the last completely filled band and the first completely empty band, called valence band and conduction band, respectively [24]. Semiconductor materials are a specific group of insulators, characterized by an energy gap smaller than possible thermal excitation energies, becoming therefore conductive at high temperatures. One example of semiconductor material used for radiation detection is Silicon: it's typical energy gap at environment conditions (T = 300K) is 1.11 eV [25]. Silicon is characterized by having an indirect bandgap: the higher valence band level is not represented in the same momentum level (**k** value) as the lower conduction level. A quantum of momentum (phonon) of wavevector **q** is generated in the process, in order to create an electron-hole pair [24], as illustrated in Figure 1.3.

The energy for generating an electron-hole pair in a semiconductor material can be accounted for by a sum of three contributions: the intrinsic bandgap (E_g), optical phonon losses and the residual kinetic energy $(\frac{9}{5}) \times E_g$ [26]. For Silicon, the value of this energy is experimentally established at 3.62 eV at 300 K [27].

The silicon sensor is usually produced using a doping process, where impurities are added

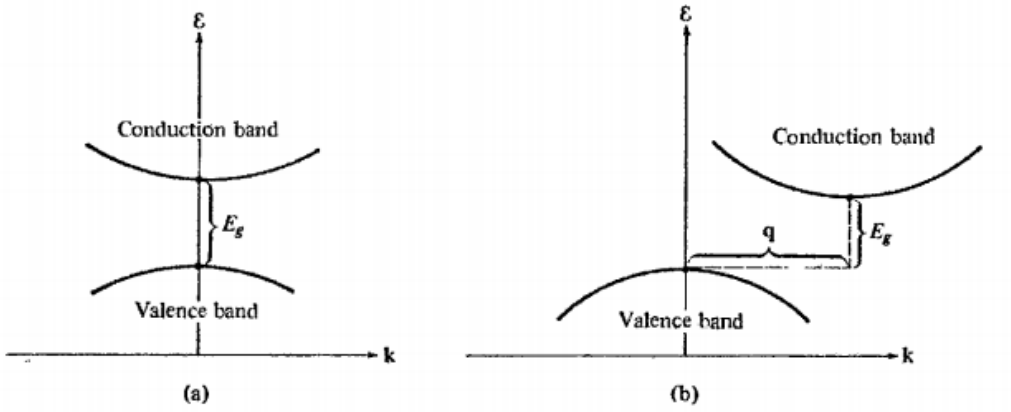

Figure 1.3: Comparison of (a) a direct and (b) an indirect bandgap, illustrating the phononic contribution needed for producing an electron-hole pair. Obtained from [24]

and replace a silicon atom in the crystal lattice, in order to change its electrical behaviour [25]. Each atom of silicon makes four covalent bonds with its neighbour atoms to crystallize in the diamond structure. If the added impurity is an atom containing five electrons in its valence band, like phosphorus, one valence electron will be remaining, taking the crystal lattice to a donor state. The resulting crystal is called a n-type silicon. The other possibility is doping the lattice with trivalent impurities, or acceptor atoms. The impurity atom will establish three covalent bonds with the neighbour silicon atoms, and one silicon bond will be missing. This results in reminiscent vacancies in the lattice, taking the crystalline silicon to a p-type category. Both doping types increase the semiconductor conductivity, as reminiscent electrons or vacancies can move from one impurity to another in the lattice [25].

Doping two different regions of a silicon crystal with donors and acceptors will form a *p-n* junction. Some charge carriers diffuse through a thin region around the interface, leaving the p-side negative with ionized acceptor atoms and the n-side positive with ionized donor atoms, creating an electric field that inhibits further diffusion. The immediate interface region is free from charge carriers, since they are recombined, and receives the name of depletion region [25].

When an ionizing photon interacts within the depletion region and transfers part of its energy to a charged particle, it generates a cascade of charge carriers, which are attracted to opposite sides according to the intrinsic electric field of the junction. This movement results in a measurable electric current related to the deposition of radiation energy, corresponding to a detection process, as illustrated in Figure 1.4.

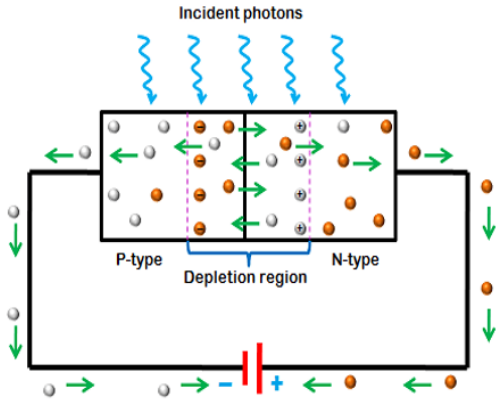

Figure 1.4: Representation of a reverse biased *p-n* junction being used for radiation detection, evidencing the charge carriers movement through the material. Obtained from [28].

By applying an external electric field by connecting a negative voltage to the p-side and a positive voltage to the n-side of the junction, like demonstrated in Figure 1.4, the charge carriers will be attracted. This will reduce the recombination probability, increase the width of the depletion region, and consequently enhance the junction efficiency on radiation detection. This assembly is denominated a photodiode, since the electric current generated by the incident photons is conduced in one direction only [29]. The silicon sensor used for Medipix3RX is a *p-n* junction reversely biased, behaving as a photodiode.

1.2.1 Detector Readout Electronics

P-n junctions can be attached for constructing devices of different behaviours. The modern microelectronics are based on transistors, devices containing two junctions in sequence, being possible both PNP or NPN sequences. Such device is called bipolar junction transistor. Other types of transistors may involve association to different materials, like metal and oxide layers, for enhancing the desired behaviour of the component.

Among the different assembly possibilities, the metal-oxide-semiconductor field effect (MOSFET) transistors present the advantages of being scalable to smaller sizes, having a high-speed operation and smaller leakage current, being less noisy than current-controlled transistor types. It has become nowadays the most common transistor type, contained in most of the integrated circuits, and being the base of the Medipix3RX ASIC device and other hybrid pixel detectors. Figure 1.5 illustrates the basic concept of a MOSFET. The three doped semiconductor parts of the MOSFET device are called source, gate and drain, respectively.

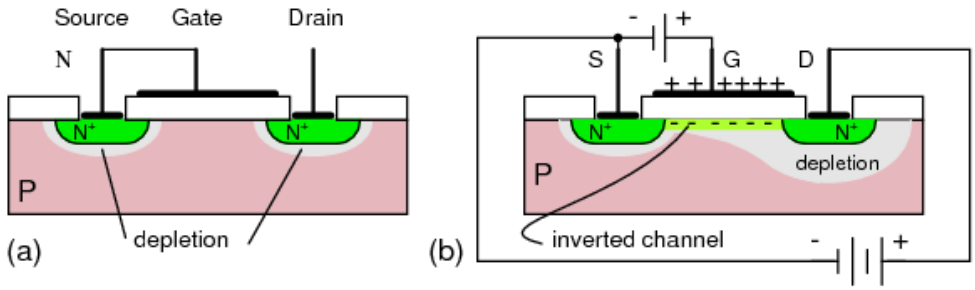

Figure 1.5: An example of a *n-channel* MOSFET transistor, (a) for a 0V gate bias and (b) positive gate bias. Obtained from [30].

MOSFETs are mainly characterized for an indirect control of the gate energy barrier, by means of a field plate. The charge is induced at the doped gate by a sheet of charge on a metal or polysilicon layer, separated from the semiconductor device by a thin layer of silicon dioxide insulator (oxide) [30], behaving as a MOS capacitor. The charge carriers are attracted by the biased top plate, creating an inverted channel under the oxide. A depletion region isolates this channel from the bulk silicon substrate. This operation allows controlling high current outputs with low input power. Without applied voltage, two depletion junctions are formed at the interfaces of the different doped materials, and electric current cannot be driven through the device. However, for the n-type MOSFET illustrated in Figure 1.5, a positive well-controlled bias voltage V_{GS} applied to the p-type gate will unbalance the charge carriers equilibrium, repelling holes and attracting electrons, creating a conducting channel; electrons can now flow from source to gate.

Once at the gate, these electrons can either recombine with the p-type gate positive charge carriers, or be drifted through the other junction, towards the drain device. Since the gate layer is commonly very thin and lightly doped, the recombination probability is usually very low [31]. This device works as a current amplifier, controlling the large drift current i_D by adjusting the gate voltage.

1.3 Hybrid Pixel Detectors and Medipix3RX

The most recent and popular X-ray imaging detector approach is based on the hybrid-pixel technology [2, 16, 32, 33], due to its advantages to usual charge-coupled devices (CCDs) and

complementary metal-oxide semiconductor (CMOS) cameras, like the absence of background noise and possibility of energy discrimination and wider dynamic range. The hybrid-pixel detector is composed by a photodiode and a CMOS circuit.

The doped and biased semiconductor sensor behaves as a photodiode, and is bump-bonded pixel-to-pixel to a readout CMOS ASIC, which is responsible for handling with the generated charge. An illustration of this assembly is exhibited in Figure 1.6.

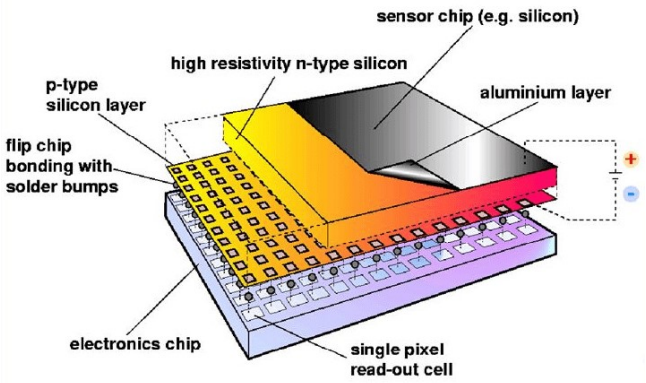

Figure 1.6: Overview of the hybrid pixel detector layers. Obtained from [34]

By the photoelectric effect, the X-ray photon will transfer all its energy to charged particles of the material, and they will generate electron-hole pairs along its path inside the sensor. The collected charge will be amplified, shaped, discriminated and digitalized into photon counts by the readout ASIC. The popularity of this technology relies in the possibility of filtering the background noise with a discriminator threshold, increasing its signal-to-noise ratio. It also can be composed into large areas, and allows fast readouts, which represents a crucial advantage for time-resolved applications [9, 10].

With the advances of the CMOS technology and the decrease of their size, smaller pixels could be reached, increasing the hybrid-pixel detectors competitiveness with indirect detectors like CCDs and silicon photo-diode arrays.

In this context, the Medipix Collaboration was founded, aiming medical applications for this technology. Medipix1 was the first large area single photon counting CMOS imaging chip, developed in 1998 with a pixel size of 170 μm square in a 64x64 pixel array. Its second version, Medipix2, was launched in 2002, using a 0.25 μm CMOS technology that allowed a decrease of the pixel size to 55 μm. The third version relied on a 0.13 μm CMOS technology, but maintained the pixel size in order to increase the pixel electronics functionality. A simplified

scheme of the Medipix3RX electronics is exhibited in Figure 1.7. The bump-bond connection to the sensor is represented by the red hexagon.

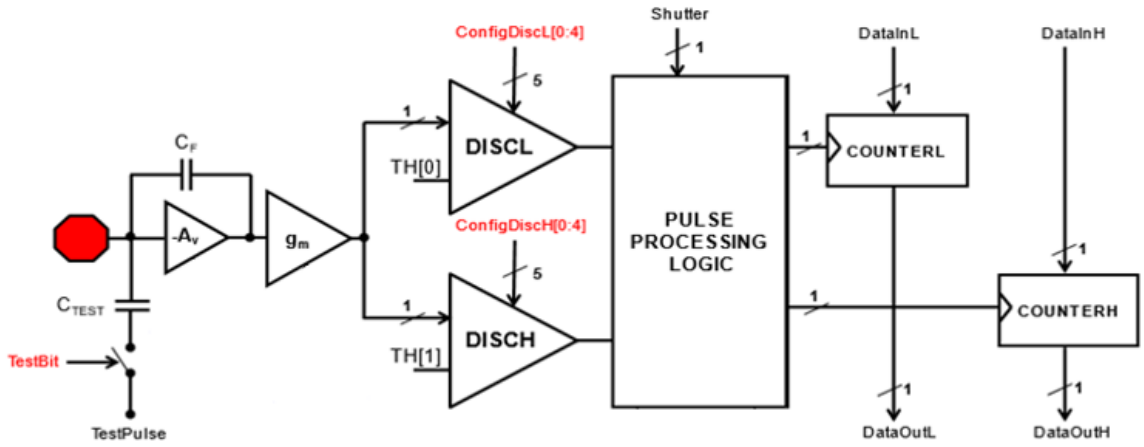

Figure 1.7: A simplified view of Medipix3RX electronics embedded in each pixel of the ASIC. Adapted from [6]

The analog circuit is composed by a charge-sensitive amplifier circuit, a shaper circuit, and two discriminators. The amplifier allows a selection among four feedback capacitance values, resulting in four possibilities of gain modes. The optimal gain value changes with the energy range of the detector application.

The generated voltage pulse goes through a first order semi-gaussian shaper circuit, that limits the pulse width at 120 ns and clears DC components of noise, other than converting the voltage pulse into a current pulse. The latter is than compared to a threshold current value set by the user at the discriminator circuit, becoming a digital count of 1 if its current overcomes the threshold. Medipix3RX has two discriminators per pixel (DISCL and DISCH), allowing the imaging of two different energies simultaneously[1]. Each discriminator has a 5-bit pixel level fine adjust of their threshold values, in order to equalize the pixel gains (identified as *ConfigDiscL* and *ConfigDiscH* in Figure 1.7).

This fine adjust is done by loading an equalization matrix of five bit values to the pixel counters [16, 35]. This is a common procedure for reducing the effect of electronic differences between the pixels and improving image quality [16, 32, 36]. Previous studies have already

[1]The Spectroscopic Mode combines pixels into clusters of four and allows measuring up to 8 energy channels simultaneously, to the detriment of the spatial resolution. This mode of operation requires specific bump-bonding from fabric, and will not be contemplated in this project.

related the need of a periodical update of the equalization matrix [35], due to detector noise increase under X-rays exposure.

The result of each discriminator is computed at the 12-bits respective counters. The counters are based in shift-registers and have a pseudo-random behaviour, requiring further interpretation to the real photon count value [16]. The pixels counters of each type are connected with the column neighbours, as shown in Figure 1.7, until the bottom periphery, where the pixel matrix data is read after the acquisition of an image. In case of a single energy measurement, and consequently the use of a single discriminator, the two counters can be combined in one counter of 24 bits [13], increasing each pixel's counting capability and expanding its dynamic range to $[0,1.7 \times 10^7)$ counts. Another possibility is the continuous read-write mode [13]: one of the pixel counters can be read while the other is used for accumulating counts during an acquisition. This nulls the matrix readout time, being extremely useful for real time events.

Specially for equalization and testing purposes, a charge input for simulating photons in the ASIC can be enabled individually per pixel. This entrance is identified in Figure 1.7 as Test Pulse. A voltage sequence of pulses goes through a 5 fF capacitance, generating charge that can be read by the preamplifier as if provoked by real photons. This feature has proven to be specially useful at the procedure of generating the equalization matrix [35].

According to Ballabriga [16], the analog and the digital parts of each pixel circuit are isolated from each other by a guard ring, and their power sources are also distinct. Another consideration is that a hard-by-design approach was adopted for some transistors at the analog circuitry: the charge-sensitive amplifier was designed to use the Enclosed Layout Transistor layout technique, an annular shape design that increases the device tolerance to radiation. An example of such design is illustrated in Figure 1.8. Due to these considerations, the digital circuitry is the main part of the pixel electronics expected to be damaged by radiation.

Medipix3RX was designed including the possibility of an inter-pixel communication: one of the pixel's discriminator circuit is used for identifying the pixel where occurred the highest energy deposition among the closest neighbours, which means, the taller current pulse. The so-called Charge Summing Mode [13] is used for correcting the charge dispersion effect on the sensor, but it has as detriment the lost of one of the discriminators and one of the counters. The mode without this correction is named Single Pixel Mode.

The charge dispersion or charge sharing effect in a pixelated detector is an interference of the

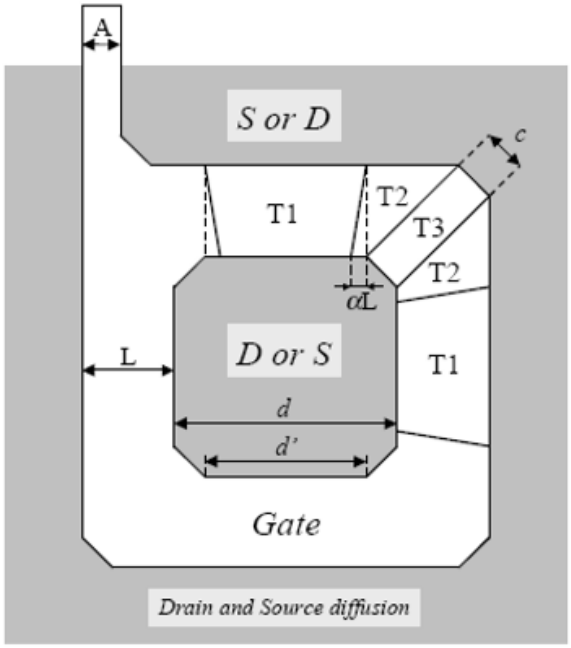

Figure 1.8: Design of the type "Enclosed Layout Transistor", used in part of the preamplifier circuit on Medipix3RX ASIC. Obtained from [16]

detection phenomenon at the image quality [13, 16, 37, 38], and varies with the Bias depletion voltage applied to the semiconductor sensor, the radiation energy to be detected, the sensor thickness and the pixel size. The charge sharing effect is illustrated in Figure 1.9. This effect enables the charge generated by the ionizing particle in a pixel to be collected by neighbour pixels. This effect becomes more important as the pixel dimensions decrease [16], deteriorating the energy resolution of the spectroscopic detector and affecting the image quality.

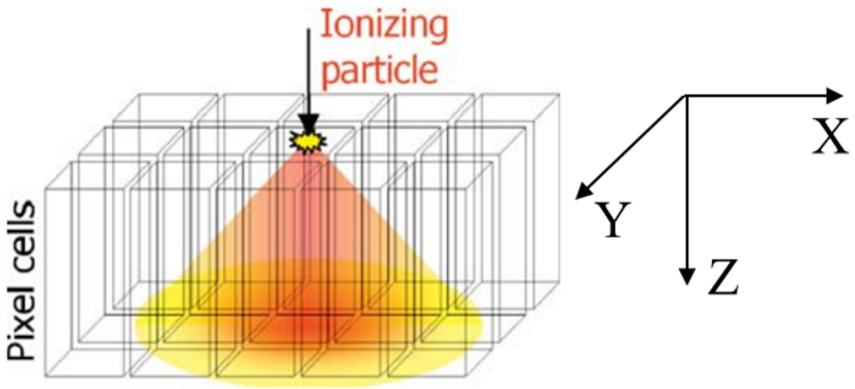

Figure 1.9: Representation of the charge-sharing effect on a pixelated detector. Adapted from [38].

1.4 Ionizing Radiation Damage in CMOS Oxides

In hybrid pixel detectors, the readout circuit is inherently connected behind the measuring sensor. Therefore, higher X-ray energies that will not be completely absorbed by the sensor can deposit energy at the active electronic layers of the ASIC. This process can result in damages to the image readout [18].

There are two kinds of possible radiation damage to electronic devices: bulk damages and surface damages [18, 39]. Bulk damages affect the silicon crystal, and are due to high momentum incident particles, like neutrons, electrons and X-rays above 300 keV [40], being out of the energy range of the applications approached by this work. Surface damages, on the other hand, are generated by ionizing energy loss of low momentum particles, like low energy X-ray photons [18, 39]; the radiation affects the SiO_2 layers present in electronics, provoking a build up of trapped charges on the oxide and on the oxide-silicon interface. This kind of damage will be the focus of this work.

Radiation induced effects have traditionally been an issue for military and space electronics technology development [39, 41, 42]. With the advance of the process technologies, motivated by Moore's law, the CMOS form factor was drastically reduced, and the development of X-ray hybrid pixel detectors became possible and competitive, bringing the MOS transistors to a new radiation environment. Specially when considering high radiation intensities like provided by synchrotron sources [18], the electronic radiation damage and consequently the detector's lifetime become an important issue.

It has been known for many years that MOS devices (metal-oxide semiconductors) are extremely sensible to ionizing radiation [41, 42]. Defects electrically loaded on oxide layers can alter the transistor switching features and also provoke an increase on leakage currents. Figure 1.10 illustrates such effect on a gate oxide layer [41]: A) shows the normal operation of a MOSFET, biased by a V_G voltage that forms a conducting channel between source and drain, allowing the current to flow; and B) illustrates a MOSFET damaged by radiation, presenting leakage current even without an external bias voltage ($V_G = 0$), due to trapped charges built up in the oxide.

The oxide charging process induced by radiation can be complex, since different events of different time scales can take place. Oldham & McLean [41] have divided the radiation response

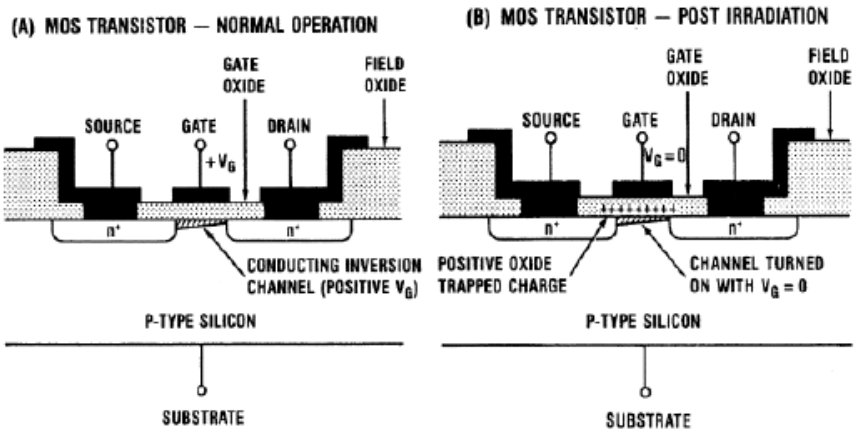

Figure 1.10: A) Illustration of an operational biased MOS transistor, evidencing the oxide layers and the conducting channel formed at the silicon by the applied gate voltage. B) a post-irradiation MOS transistor, exhibiting trapped charges in the oxide and a consequent conducting channel even without any gate voltage. Obtained from [41]

in four major events. First, the ionizing photon interaction generates cascading electron-hole pairs in the oxide: the energy of 17 ± 1 eV has been experimentally determined for an electron-hole pair creation in SiO_2 [43]. The electron mobility is much higher than the hole's. The electrons are drifted towards the bias voltage direction and leave the oxide in the order of picosseconds, while holes mostly remain near their generation site. Besides, a small fraction of the electron-hole pairs are recombined. This process is illustrated in Figure 1.11 in a biased gate oxide layer.

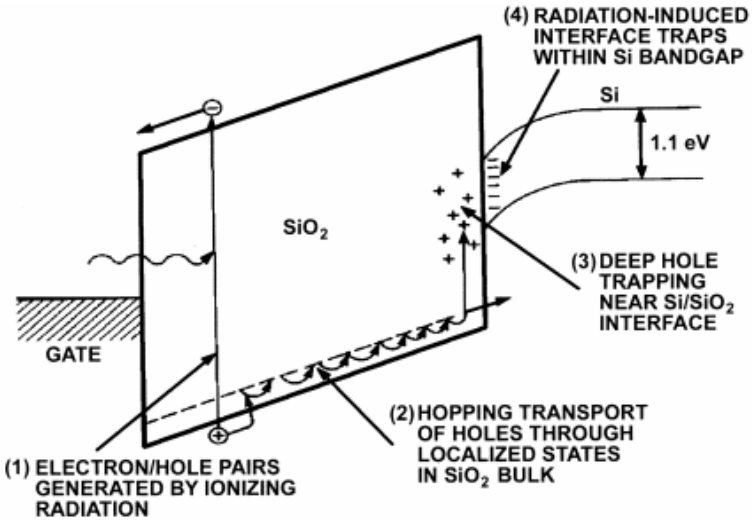

Figure 1.11: Ionization effects on the readout electronics oxide layer: mechanisms of trapped charges formation (N_{ox}) and interface defects N_{it}). Obtained from [41]

The second event describes a process which occurs in the order of seconds, where the holes are drifted in the direction of the oxide-silicon interface. This is interpreted as a recovery effect.

In the third event, some of the holes that reach the Si-SiO_2 interface are trapped into oxygen vacancies, becoming stable positive charges at the oxide layer, which can persist for hours or even years [41].

The fourth process is the buildup of interface traps. The hole transport or trapping through the oxide is believed to release hydrogen protons [42]. Those protons are drift to the interface by the bias voltage, where they may break the hydrogenated silicon bonds at the interface, producing dangling silicon bonds: interface traps. These traps have energy levels distributed throughout the silicon band gap [18]. At a long term state, negatively charged interface traps may compensate the trapped holes, provoking a super-recovery effect [41].

The fraction of generated electron-hole pairs that do not recombine is highly dependent on the bias electric field and the incident radiation type and energy. The applied voltage acts in order to separate the charge carriers, being a positive factor on this fraction. Figure 1.12 exhibits a summary of experimentally obtained recombination results for different types of incident particles and as a function of the applied electric field. The 10 keV X-ray source, which is the most representative of the energy range used in this work, presents a high fraction of unrecombined holes.

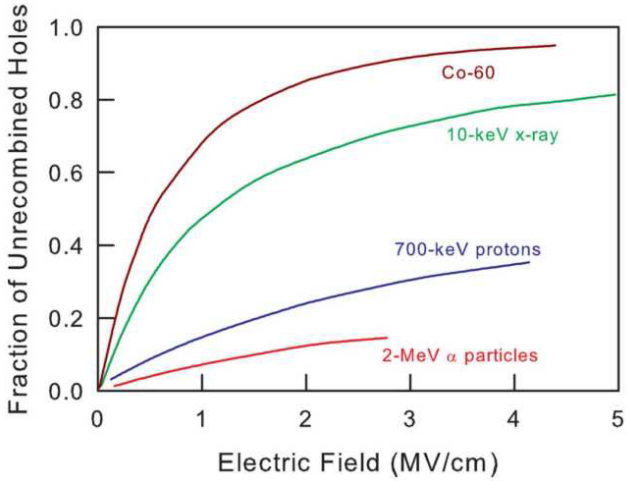

Figure 1.12: Illustration of the recombination rate dependency of electron-hole pairs generated in the oxide with electric field and radiation type. Obtained from [41]

The experimental results from Figure 1.12 were presented in 1983, and it is reasonable to

consider that the CMOS scaling process from the past years and the consequent oxide layer thinning played a significant role on increasing the radiation tolerance of the system [39, 44]. Medipix3RX was designed based on the 0.13 μm CMOS technology, which present gate oxide thickness of 2.2 nm. Thus, even for electric fields up to 4 MV/cm applied to the gates [16], effects of oxide trapped charge are expected to be minimal, since the oxide thickness has reached values smaller than the approximate distance for high probability electron tunneling from the adjacent materials ($\approx$ 3 nm) [45]. On the other hand, the CMOS scaling has reduced on-chip capacitances, increasing the electronics vulnerability to the called soft errors [46]. A failure of a system is characterized as a soft error if the stored data are corrupted, but the device itself is not damaged, as opposed to permanent device failures (hard errors). These nomenclature is primarily applied to false data state induced in microprocessor logic or memories [47] by an ionizing radiation event.

For the Medipix3RX ASIC, these soft errors are expected to affect the 12 bit shift-registers that form the counters of each pixel, responsible for storing the incident photon counts. This kind of failure can damage the whole data set and be a problem for both synchrotron and medical applications [17]: its understanding and characterization becomes essential in X-ray detector analysis.

The gate oxide, however, is not the only oxide layer present in the chip: the 130 nm CMOS devices are normally designed with a dielectric isolation between adjacent transistors, in order to avoid cross-talk, named Shallow Trench Isolation (STI). It has been reported that the trapped charges at the STI layer respond for most of the radiation effects on the modern CMOS devices performance [44, 48], since its thickness is normally higher than the gate oxide. The ionization damage is responsible for the creation of a leakage path between neighbouring transistors, through the four major processes described above.

1.5 The Monte Carlo Simulation Tool: PENELOPE

PENELOPE is a well documented tool for simulating the transport of electrons, photons and positrons in materials, based on the Monte Carlo method and developed in Fortran 90 [20], which stands out by a detailed description of the physical processes. It embraces energies from 50 eV to 1 GeV, enables the elaboration of complex geometries and has a vast database of

materials, including 99 elements and 181 substances; the user can also add new composite materials to the list. This database includes information like cross sections for different radiation types, density, ionization energies and form factors. Other than this, the materials are considered electron clouds for the simulation purposes, not including energy bandgap information or crystalline structure effects.

PENELOPE is complemented by a "Main" program, that guides the simulation and receives inputs from the simulation source file **penelope.f** and subprograms like **pengeom.f**, responsible for interpreting the geometry of the material bodies, and **penvared.f**, which includes variance reduction tools. The package also includes auxiliary programs like *gView* for visualizing and debugging of the geometry, and **material.f** for creation of database of fundamental quantities for describe the radiation interaction.

The Monte Carlo method is based on the random numbers sampling and known probability distributions for obtaining statistic results. It can be used for describing mathematically the phenomena considered stochastic, where each event is independent. The radiation transport through materials is a stochastic process, being able to be described by Monte Carlo simulation [20].

The main problem of Monte Carlo method is the simulation time, once it simulates each particle individually. In this context the variance reduction techniques come in hand, reducing the need of simulating a large amount of histories [20].

There are different "Main" programs for PENELOPE. In this work the PenEasy 2015, a modular and general-purpose program was chosen. It allows the user to select only the data outputs that provides the desired information, decreasing the simulation time. Its modularity also reduces the programming cost in case of the need to perform application specific alterations in the code.

The *PenEasy* simulation possible outputs are named "Tallys", which can be individually selected. In this study, the main tallys to be used are Energy Deposition, Pulse Height Spectrum and Pixelated Imaging Detector:

- The Energy Deposition tally provides the deposited dose in each determined material of the geometry, in $eV/history$ units, and will be used to obtain the deposited dose at the oxide layers.

- The Pulse Height Spectrum provides the deposited dose spectrum at the chosen material, in $1/(eV.history)$ units.
- The tally Pixelated Imaging Detector divides the detector material into pixels, which size is inputted by the user. It simulates a detector response for three different modes:
  - The Energy Integrating Mode computes the energy deposited at each pixel area per history. The output is a pixelated image of $eV/cm^2.history$ values. It simulates the response of indirect integrating detectors like Charged-Coupled Devices and photodiodes.
  - The Photon Counting Mode computes the number of photon counts per pixel, per history. A photon count is considered when the deposited energy at the pixel exceeds an energy threshold value defined by the user. The output is a pixelated image of $counts/cm^2.history$ values. This mode is the closest simulation of a direct photon-counting detector behaviour, such as Pilatus [32] and Medipix3RX [13].
  - The Energy Discriminating Mode computes a pulse height spectrum per pixel. The initial energy, final energy and the number of energy bins are parameters provided by the user. The output is in $counts/cm^2.eV.history$ units. This mode allows the convolution of the simulated spectrum with an energy resolution function, allowing inclusion of detection artifacts and better comparison with the experimental results.

The 2015 version of *PenEasy* also includes a Source Box Isotropic Gauss Spectrum algorithm: the user can configure a rectangular box in which the particles will be generated, by defining its three sizes in X Y and Z directions. Gaussian distributions of intensity in X and Y directions can be configured by entering Full-Width at Half Maximum values in centimeters for each. This possibility helps modeling the source accordingly, and was used for the modeling the intensity shape of the synchrotron white beam coming from a bending magnet source.

1.6 The Experimental Source: Synchrotron

A synchrotron source is a powerful tool for scientific development. It is a type of particle accelerator, providing accelerated particles of well controlled properties and parameters, defined

accordingly to the desired application. Different than particle collider accelerators, like the Large-Hadron-Collider at CERN, it accelerates and collimates electrons at relativistic speeds in order to generate the synchrotron light, which is an electromagnetic radiation [49]. This radiation is many orders of magnitude more brilliant than X-rays produced in conventional X-ray tubes, which means it provides more photons at a focused beam, enabling, for instance, scanning samples with nanofocus photon beams. Other than improvements in energy range and intensity, the synchrotron source presents interesting features like polarization selection based on the source, used for investigating magnetic reactions on materials [50]; and the possibility of producing coherent radiation, enabling techniques like coherent diffraction imaging [51].

A synchrotron source is composed by four major features: the linear accelerator (LINAC), an energy ramping ring (booster), a storage ring and the tangential beamlines. Figure 1.13 presents a general diagram of the current Brazilian UVX Synchrotron for exemplification.

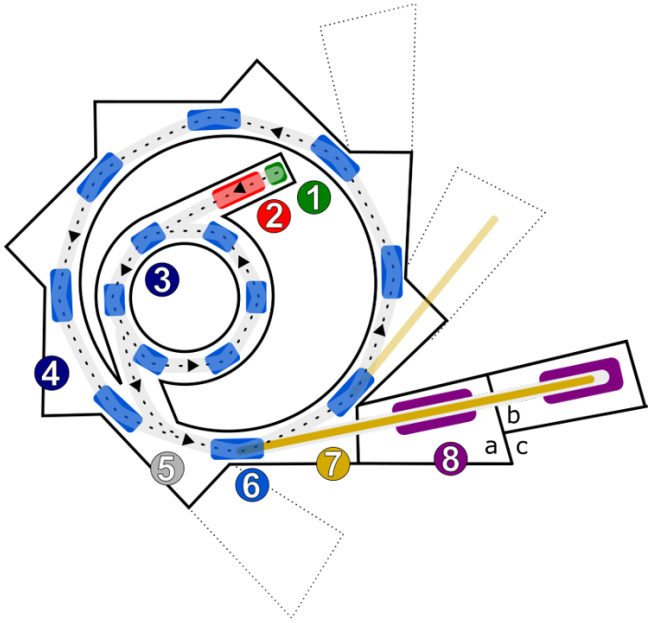

Figure 1.13: General diagram of Brazilian UVX Synchrotron, as an example. The electrons generated by the electron gun (1) gain energy through the linear accelerator at the center of the ring (2), which conduces the electrons to a smaller ring, named booster (3) inside the effective storage ring (4), where they are accelerated to near light speed. The outer storage ring contains straight sections (5) where the electrons are accelerated by electric fields. The blue rectangles (6) are magnets that bend the beam, provoking the synchrotron radiation generation, which is directed to the tangential beamlines (7) and their final application (8). LNLS/CNPEM Public Release.

The linear accelerator is the electron input. Electrons from a filament are ripped by thermionic effect, grouped into bunches and accelerated to hundreds of MeV, before being

directed to the booster. The latter is responsible for accelerating the electrons until a few GeV before injecting them into the storage ring. This system is operated for injecting electrons and maintaining the electron current at the main storage ring; at UVX, the current Brazilian synchrotron light source, the injection procedure is performed twice a day [52].

At the storage ring, electrons are pilled up until hitting the desired current. The electron beam travels through the ring for hours in relativistic speeds, inside a ultra-high vacuum tubes. However, current losses due to random single-particle collisional processes [53] provoke an exponential decay of this current along the day, as exemplified in Figure 1.14.

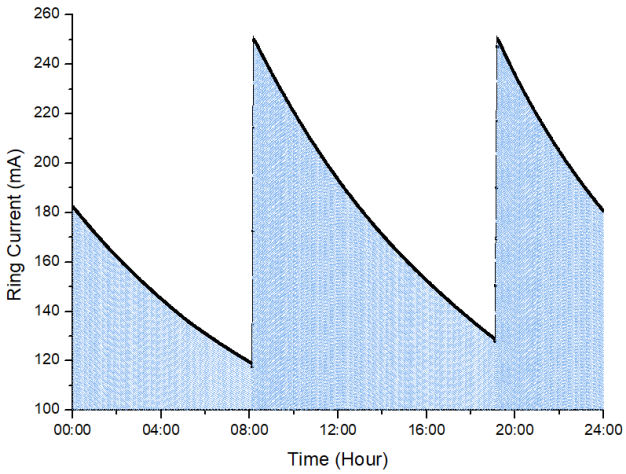

Figure 1.14: Example of the Brazilian UVX synchrotron ring current decay along a day of experiment. Obtained from `https://status.lnls.br`, adapted.

The electrons are deflected by magnets along their trajectory; when moving through a dipole they are accelerated centrifugally, emitting the synchrotron radiation [54]. Similar effects are provoked by more efficient magnets, like the undulators and wiggler systems that characterize the third generation synchrotron laboratories [55]. As the electron beam decays, so does the intensity of the synchrotron light [53]. Therefore, the source effects need to be known and taken into account by the scientific user when elaborating the experiment at the beamlines.

Chapter 2

Materials and Methods

This chapter describes the materials and methods adopted in this work. It was divided in two main sections: materials and methods for the Monte Carlo simulation, and for the experimental phase. The Monte Carlo simulation was used for obtaining the deposited dose at the oxide layers of the ASIC. The ASIC layers and their specific thicknesses were obtained. The chip geometry was modelled at the *penGeom* tool, making use of the planar symmetry of the object. The detection process through the sensor was analyzed, and the original code was modified and validated for including charge dispersion effects, to obtain a more accurate image and spectrum of the deposited energy at the sensor and relate to the experimental data. The dose at the oxide layers was calculated based on the simulation result of energy deposition in each material. At the experimental section, a procedure for the experiment was proposed, dividing the irradiation into steps and including characterization of the damage between the steps. Three experiments were performed: a low dose measurement reaching 809 ± 6 Gy, and two high dose measurements reaching 6178 ± 29 Gy and 6228 ± 19 Gy, with different dose rates. Different parameters were proposed for evaluating the dose effects on the image and spectrum data coming out of the detector.

2.1 Chip Materials Proportion

The oxide layer thickness between gate and source of transistors varies with the chip technology generation. Medipix3RX was designed for 130 nm CMOS technology, with an oxide layer thickness of 2.2 nm [16]. At this technology, it is common to electrically isolate neighbouring

transistors with an oxide layer (STI). An illustration of this concept is exhibited in Figure 2.1.

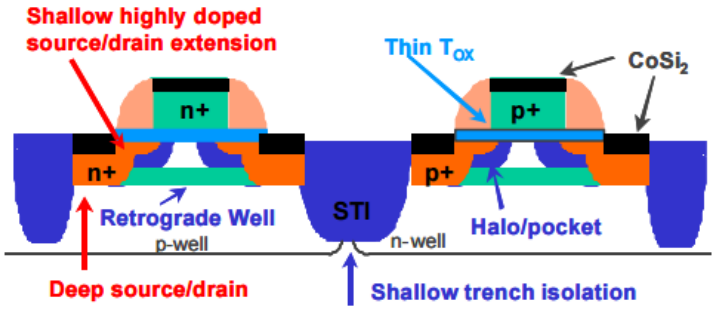

Figure 2.1: Drawing of a 130 nm CMOS cross-cut section, illustrating the oxide layer between transistors and the STI oxide. Obtained from [56].

Other than the active electronics, that compose the Front End of Line (FEOL) of the CMOS manufacture process, the Back End of Line (BEOL) includes 5 to 8 metal layers, separated by oxide insulation layers, of varying widths, as illustrated in Figure 2.2(a) and testified by a Scanning Electron Microscopy of a cross-cut wafer in Figure 2.2(b).

The layer widths and the number of metal layers vary with the manufacturer and the application. Information regarding the specific values for the Medipix3RX ASIC design are stealthy and were obtained directly with the chip designer, Rafael Ballabriga [16]. These data were considered for modeling the chip geometry at the simulation tool, aiming at the most precise deposited dose value at the layers of interest.

In order to simplify the geometry and reduce the simulation time, the FEOL layers, such as the polysilicon gate, the gate oxide itself and the STI layer were estimated to uniform continuous surfaces. The doped semiconductor sensor and the bulk of the chip were considered pure silicon. For the calculus of the deposited dose, it was considered both the dose at the gate oxide layer and at the STI layer.

2.2 Monte Carlo Simulation

For this work the PENELOPE package version of 2014 was used, complemented by the main program *penEasy* version of 2015, both developed at Fortran 90 [20].

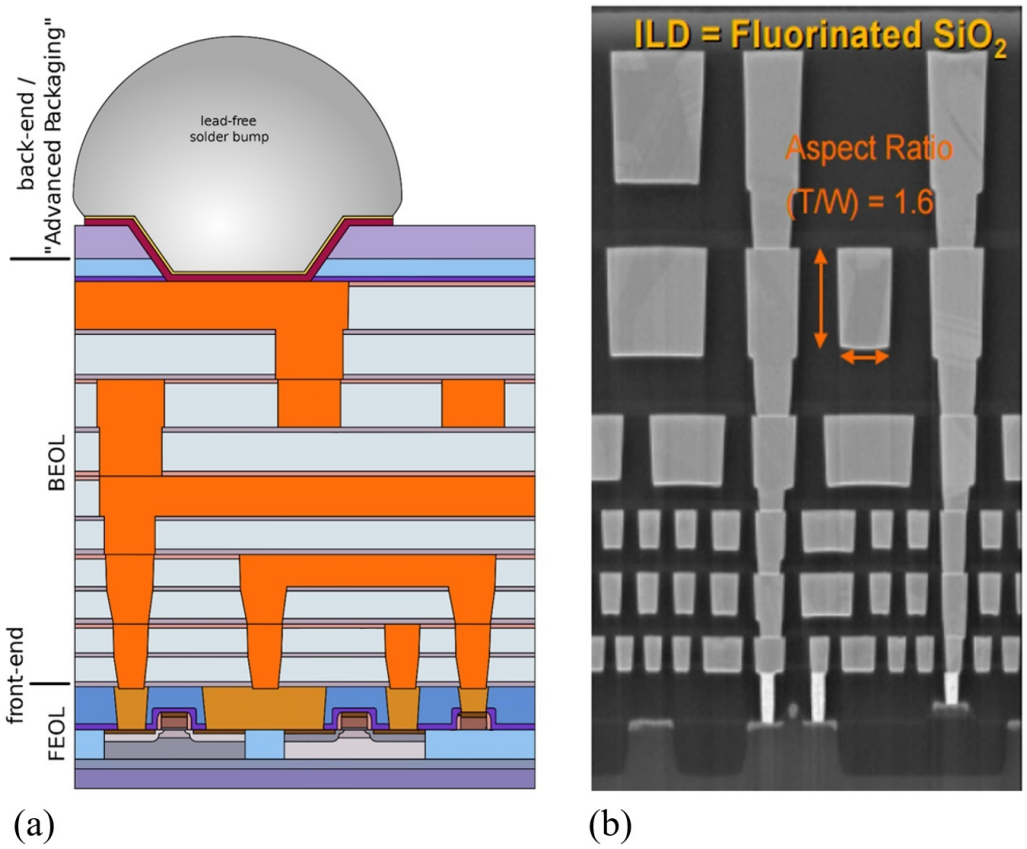

Figure 2.2: A) Scheme of a CMOS cross-cut section, evidencing the various possible layers; B) SEM image of a 130 nm CMOS cross-cut processed wafer. Obtained from [56], adapted.

2.2.1 Geometry

The Silicon sensor bump-bonded to the Medipix ASIC device was created at the PENGEOM platform, considering the detailed material layers obtained for this design and CMOS technology. The planar symmetry of the device was used to simplify the geometry. A comparison between (a) a scheme of the cross-cut section of a hybrid pixel detector [16] and (b) a picture of the geometry designed at PENGEOM, obtained with *gview2d* software [20], can be observed in Figure 2.3. The sensor is identified in purple, covered by a thin layer of Aluminum (green) for the Bias voltage connection; the bump-bonds are represented in blue, connecting the sensor to the ASIC pixels, presented with its metal and oxide layers (yellow and red respectively) and the silicon bulk (orange). A tridimensional representation of the same geometry obtained with *gview3d* software [20], for better visualization, is presented in Figure 2.4.

Since the X-ray radiation energy range mainly considered for this detector application is not significantly transmitted by the ASIC silicon bulk of 650 μm, the electronic layers beneath

the ASIC were not included in the simulation.

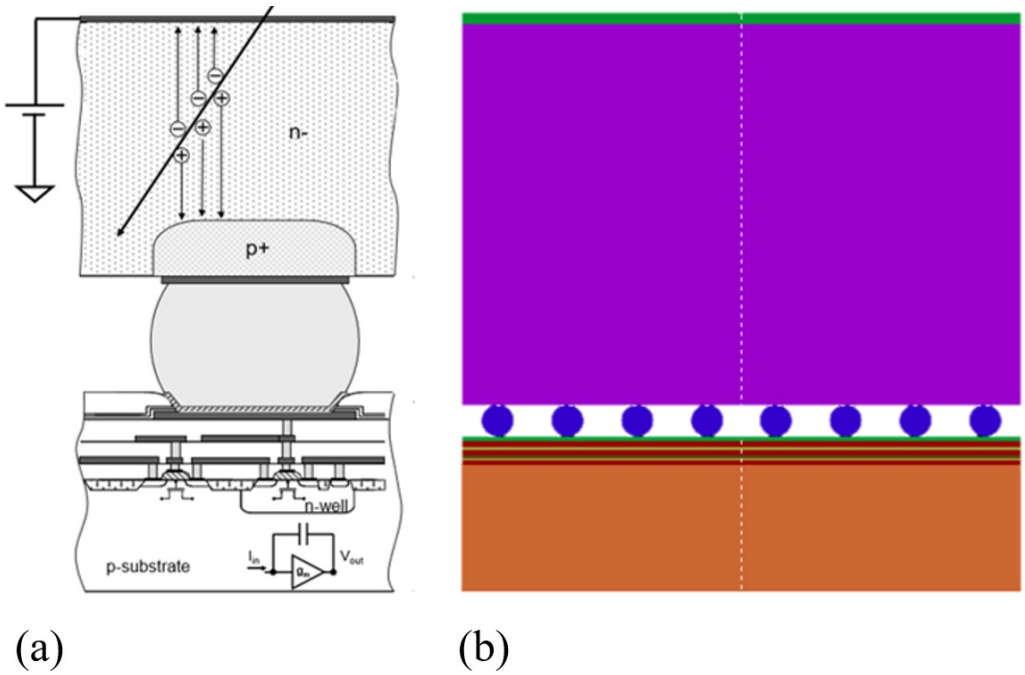

Figure 2.3: (a) Scheme representing the cross-cut section of a hybrid pixel detector single pixel, obtained from [16]. (b) Cross-cut section of the geometry created for Penelope simulation, exhibiting the sensor (purple), the bump bonds connecting the sensor to each chip pixel (blue spheres) and the metal and oxide layers (in yellow and red respectively). The silicon bulk is considered pure Silicon, in orange. This figure was obtained with the *gview2d* software [20].

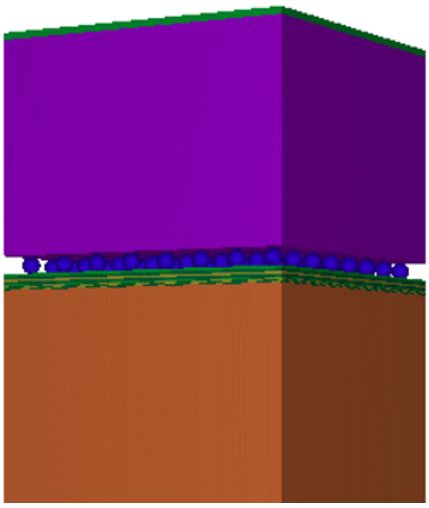

Figure 2.4: Representation of the full detector geometry created at the PenGeom software.

2.2.2 Inclusion of Electric Field Effects

The effect of charge dispersion inside the silicon was modeled considering the energy deposited by the interaction and the position of the interaction. In a first approach, an algorithm filtering the photoelectric interactions inside the detector and modeling the charge generation according to the depletion voltage was elaborated.

The behaviour of the charge dispersion can be described by the bi-dimensional Gaussian equation (2.2.1):

$$f(x,y) = Z \exp\left(- \frac{(x-x_0)^2 + (y-y_0)^2}{2\sigma^2} \right) \tag{2.2.1}$$

where:

- Z is the height of the interaction in the sensor: value of $f(x,y)$ for $x = x_0$ and $y = y_0$
- x_0, y_0 are the interaction coordinates on the pixel (XY surface)
- x, y are the coordinates of the position at the pixel surface
- σ is the Gaussian standard deviation (which is considered symmetric around Z axis).

The standard deviation, σ, is the quantity that describes the charge dispersion inside a material, and was estimated using the carrier diffusion in a semiconductor material based on the dispersion width Δx at 37% of the peak value (Z), as defined in equation (2.2.2) [38]:

$$\Delta x = 4\sqrt{D_n \tau} \tag{2.2.2}$$

In equation (2.2.2), D_n is the diffusion coefficient for charge carriers in the sensor, and $\tau = \frac{d}{v_d}$ is the drift time, being $v_d = \mu_e \times E$ the drift velocity, μ_e is the charge carrier mobility on the sensor material, and E the applied electric field (Bias).

The diffusion coefficient can be defined by the Einstein equation (2.2.3):

$$D_n = \frac{\mu_e k_B T}{e} \tag{2.2.3}$$

where k_B is the Boltzmann constant and T stands for the sensor temperature. Considering the bi-dimensional Gaussian equation, $\frac{f(x,y)}{Z} = 0.37$ for $x = x_0 \pm \frac{\Delta x}{2}$ and $y = y_0$. The σ value can

be obtained by equation (2.2.4):

$$\sigma \approx \sqrt{\frac{2D_n Z}{\mu_e E}} = \sqrt{\frac{2k_B T Z}{eE}} \tag{2.2.4}$$

The input data for the sensor dispersion modeling are: the primary photon interaction coordinates (X_0, Y_0, Z) and the electric field applied for depletion. The generated photoelectron and Auger electron will move by drift in the electrode direction, generating electron-hole pairs. The pair cloud has a dispersion defined by the bi-dimensional Gaussian equation.

The deposited charge at each pixel is proportional to the Gaussian volume determined by the pixel limits. The total generated charge, in electron counts, can be obtained using equation (2.2.5):

$$Q_{Total} = \frac{E_{ph}}{E_{pair}} \tag{2.2.5}$$

where E_{ph} is the primary photon energy, and E_{pair} is the necessary energy for a electron-hole pair production in the semiconductor (3.62 eV for silicon [57]).

The simulation of the charge dispersion effect was based on the *Tally PenEasy Imaging*, developed by Andreu Badal for simulating imaging systems for medical applications, mainly scintillator detectors [58], where optical (visible-range) photons are generated from the primary photon energy. This Tally was modified to adapt the variables and functions to the most recent version of Penelope 2014 and PenEasy 2015 codes. Since the optical photons also behave according to a Gaussian distribution, their modeling was adapted for the electron-hole pairs analytical generation at the semiconductor sensor.

The *Tally Imaging* code included the Poisson's dispersion on the number of generated optical photons and the application of the Box-Müller method [59] for sampling the new coordinate (x, y) of each optical photon, which were adapted for the electron-hole pairs application. The Box-Müller method takes the two-dimensional Gaussian distribution as boundary, with mean and variance provided as input [59]. A schematic of the algorithm is illustrated in Figure 2.5.

The code including the charge dispersion is 35% more time demanding compared with the original one, which was an expected result, once it includes a Monte Carlo simulation for each electron-hole pair generated per each photoelectron and Auger electron deposited in the sensor.

The implementation of the charge dispersion was based on primary interaction inside the sensor areas, and the generation of electron-hole pairs was based on the energy deposited in

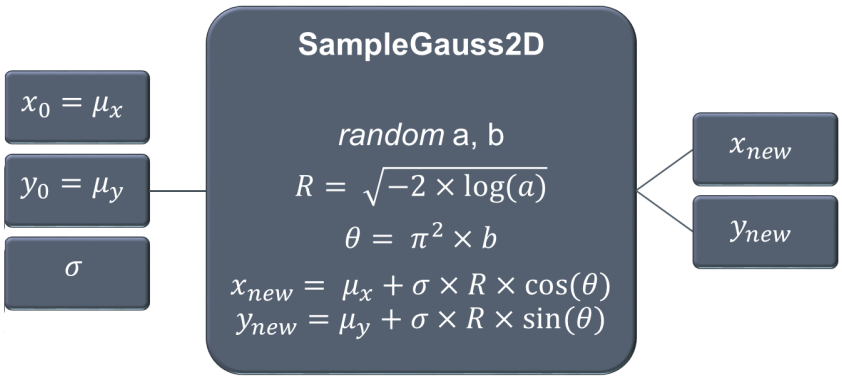

Figure 2.5: Representation of the Box-Müller method application for distributing the electron-hole pairs

sensor. For this purpose, the history of each particle was followed and its related labels were monitored [20]:

- NHIST: history number (number of the generated primary photon)
- KPAR: type of the particle (1 for electrons, 2 for photons, 3 for positrons)
- MODE: interaction mechanism that will occur to this particle
- ARG: particle energy
- ILB(1): particle generation (1 for primary particles, 2 for secondary particles, etc)
- ILB(2): type KPAR of the mother particle, if ILB(1)>1
- ILB(3): interaction mechanism ICOL that generated this particle
- ILB(4): identifies particles emitted by atomic relaxation (e. g. Auger eletrons)

Table 2.1 exhibits some examples of detected particles and their labels. At the first row, a primary (ILB(1) = 1) photon (KPAR = 2) of 8 keV (ARG = 8000) was generated and interacts through photoelectric effect (MODE = -3). The two rows in sequence show two secondary (ILB(1) = 2) electrons (KPAR = 1) generated by this photon (NHIST = 1, ILB(2) = 2), that deposit their energy in the material (ARG < 0). The ILB(4) label of the second row identifies this electron as Auger, resulting from atomic relaxation events, while the third row electron is the photoelectron (ILB(3) = 3). It was considered the sum of the two electrons energies at the dispersion input, once the two phenomena are simultaneous.

The fourth row exhibits the generation of a new primary photon, that generates a photoelectron and a characteristic photon, that provokes a tertiary electron generation. The subsequent lines show Auger electrons of different energies, therefore coming from different bands, and photoelectrons of the same energy. The sum of the generated particles energies is always smaller than the mother-particle energy.

Table 2.1: PENELOPE labels for a few particles of the Simulation

Mode	NHIST	ARG	KPAR	ILB(1)	ILB(2)	ILB(3)	ILB(4)
-3	1	8000	2	1	0	0	0
-99	1	-1612.54	1	2	2	3	14010404
-99	1	-6156	1	2	2	3	0
-3	2	8000	2	1	0	0	0
-99	2	-1739.98	2	2	2	3	14010400
-99	2	-1739.98	1	3	2	3	0
-99	2	-6156	1	2	2	3	0
-3	3	8000	2	1	0	0	0
-99	3	-1663.32	1	2	2	3	14010205
-99	3	-6156	1	2	2	3	0
-99	3	-2196.71	1	3	1	3	0

The new code was inserted as an option on the Tally Pixel Image Detector already existent in PenEasy 2014. The choice to enable or disable the dispersion is available to the user at the input file of PenEasy, as shown in Figure 2.6.

```
[SECTION TALLY PIXELATED IMAGING DETECTOR v.2017-02-17]
 ON              STATUS (ON or OFF)
 1               DETECTION MATERIAL
 0               FILTER PHOTON INTERACTION (0=NOFILTER, -1=UNSCATTERED, 1=RAYLEIGH,
                 2=COMPTON, 3=SECONDARIES, 9=MULTISCATTERED)
 1               INCLUDE DISPERSION EFFECTS (0=NO, 1=YES)
 1000            BIAS ELECTRIC FIELD FOR DISPERSION EFFECTS (V/cm)
 0.0055  4       X-PIXEL SIZE(cm), No. X-PIXELS (ENTER 0 IN EITHER FIELD FOR AUTO)
 0.0055  4       Y-PIXEL SIZE(cm), No. Y-PIXELS (ENTER 0 IN EITHER FIELD FOR AUTO)
 2               DETECTION MODE (1=ENERGY INTEGRATING, 2=PHOTON COUNTING, 3=PHOTON
                 ENERGY DISCRIMINATING aka SPECTRUM)
 1.0e3           ENERGY DEPOSITION THRESHOLD (eV) FOR MODE=2 (IGNORED FOR OTHER
                 MODES)
 0.0  1.0e4  100 EMIN,EMAX(eV), No. OF E BINS FOR MODE=3 (IGNORED FOR OTHER MODES)
 0.0  0.0        ENERGY RESOLUTION, ENTER A(eV^2),B(eV) FOR A GAUSSIAN WITH
                 FWHM[eV]=sqrt(A+B*E[eV])
 2               REPORT FORMAT (1=COLUMNAR, 2=MATRIX, 3=BINARY)
 0.0             RELATIVE UNCERTAINTY (%) REQUESTED
[END OF IMG SECTION]
```

Figure 2.6: Tally Pixel Imaging Detector modified input, evidencing the option of including or not the dispersion effects, and for choosing the electric field (Bias)

2.2.3 Simulation Performance Comparison

For the same cut-off energies and history number configurations, the original Tally performed 5.298×10^2 histories/second, while the modified tally, including the dispersion effects for a $1000 V/cm$ electric field, performed 3.935×10^2 histories/second, in a Intel Core ® i5 4200U 1.60 GHz processor, with 2 nuclei and 4 threads, 8 GB RAM memory, Windows 10. Considering a Monte Carlo simulation that includes a new modeling and additional sampling to the radiation transport, this speed reduction was expected.

The sum of photon counts at the image for the same source, threshold and number of histories was 40% higher using the charge dispersion modeling. This difference was expected, since the same photon will be counted more than once when it reaches a pixel edge [33, 60].

2.2.4 Simulation Validation

The new code was validated by checking its response to alterations of parameters like the electric field value, the incident photon energy, the pixel size, the beam position and the detector's energy threshold in the resulting image or spectrum, and comparing to the expected behaviour. The impact of the simulated charge dispersion on the detector's spatial resolution was also investigated.

2.2.5 Dose Simulation

An experiment proposal was submitted for using the IMX beamline at LNLS. This beamline was chosen for its easy procedure of removing the monochromator from the front of the beam, allowing direct access to the bending magnet beam, and therefore increasing the deposited dose to the detector. The proposal experiment was divided into two steps: a preliminary step, aiming to verify subtle effects generated by lower doses; and a further step for higher doses. These experiments are described in details in section 2.3.

The proposed experiment setup was simulated, in order to estimate the deposited dose at the oxide layers of the ASIC as a function of incident fluence. The energy spectrum generated by the bending magnet was obtained analytically through the software XOP, developed by the Argonne National Laboratory (ANL) and widely used in synchrotron sources [61]. The software takes as inputs the synchrotron ring characteristics, like its magnetic field, current,

electron energy, and also the bending magnet horizontal divergence, and provides the number of photons provided by the source in discrete steps of energy, considering 0.1% of bandwidth.

The attenuation of the radiation through the optical elements until reaching the detector was calculated analytically considering: beryllium windows of 250 μm, 95.7 cm of atmospheric air and possible additional silicon filtration. The transmission data used to obtain the final spectrum reaching the detector were obtained from the Center of X-ray Optics database [62], by applying the Beer-Lambert law to each discrete step of energy. The beamline sketch with the crossed elements was provided by the beamline staff [63] and can be checked in Figure 2.7.

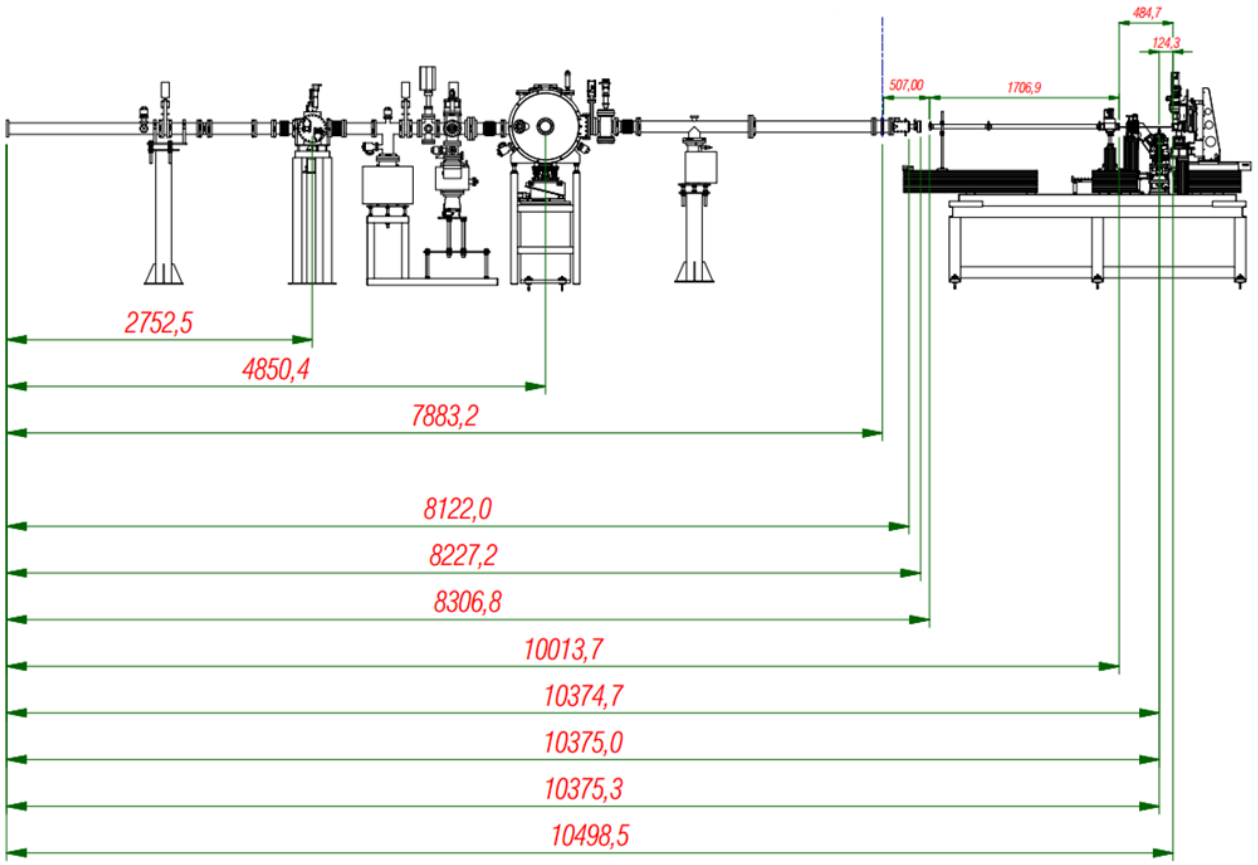

Figure 2.7: IMX beamline sketch, indicating the source-to-detector distance, the air gaps and other materials crossed by the beam. Provided by [63]. Distances in millimeters.

The simulated energy spectrum reaching the detector and going through the beamline elements, but without considering further filters, is shown in Figure 2.8.

The Gaussian spatial distribution of the beam in the vertical axis (Figure 2.9) is expected as an effect of the bending magnet polarization, and was considered in the simulation. The

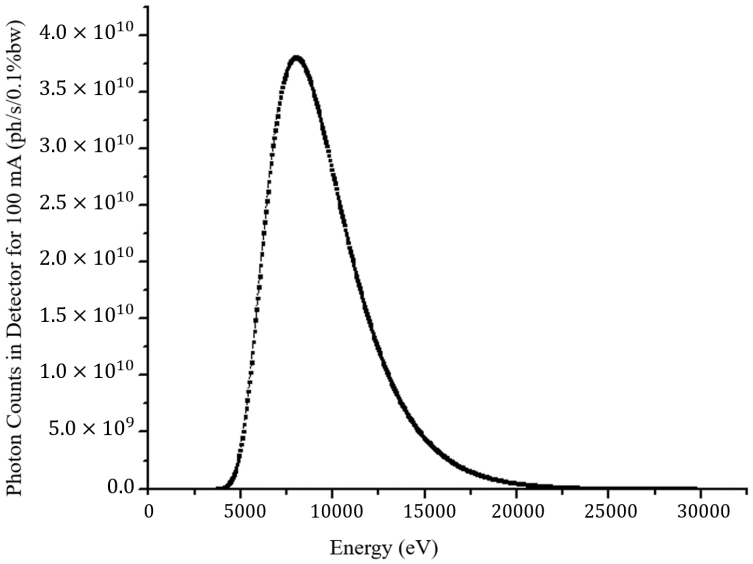

Figure 2.8: Simulated energy spectrum expected at the detector position, without further filters.

full-width at half maximum (FWHM) was measured from an image of the beam obtained experimentally with a Medipix3RX single chip detector and adjusted to a Gaussian, resulting in 3.05 ± 0.06 mm. In the horizontal axis the beam was considered uniform. This information was used as an input to the Source Box Isotropic Gauss Spectrum section from *PenEasy*. The source was modeled with horizontal size 6.05 mm, with the vertical Gaussian distribution defined by a FWHM of 3.05 mm and 0 mm thickness. Even though the beam does not present an uniform intensity along the irradiated area, the whole intensity in the defined area was considered for the dose calculation, in order to increase the pixel statistics for the damage measure.

The calculus of the dose deposited at the oxide layers of the ASIC provided by the simulation was used as an estimation of the real deposited dose value, being validated by a comparison between the experimental data provided by the detector with the simulated data. The white beam coming from the bending magnet X-ray Imaging beamline with 4.05 mm silicon filters was used as a photon source to generate an image and an energy spectrum.

The spectrum was obtained with a threshold scan procedure with a Medipix3RX single chip bonded to a 200 μm n-on-p silicon sensor, configured to 12 bits counters and Single Pixel Mode. The detector was modeled at the simulation tool, and the simulation data was obtained as a result from the modified tally *Pixelated Imaging Detector* for inclusion of charge dispersion effects. The Photon Counting Mode provided the detected image of the beam, and the Energy

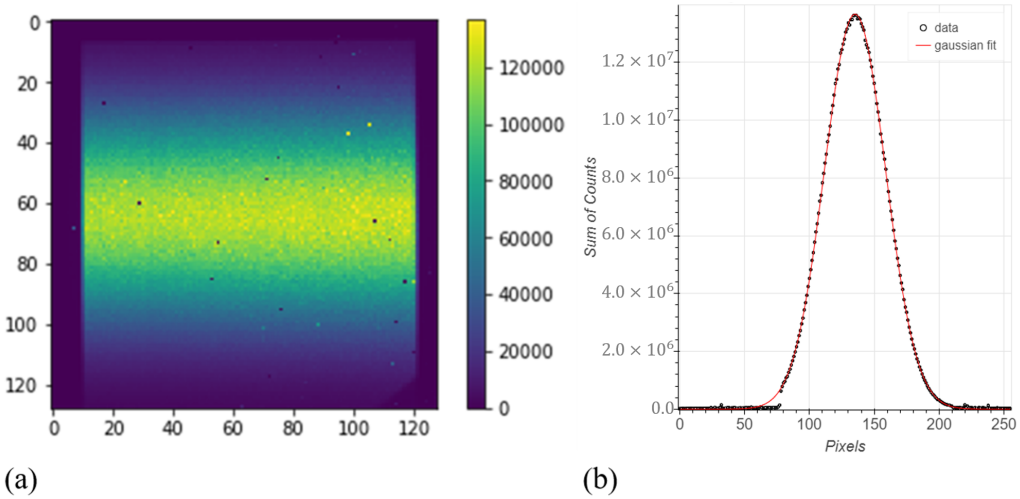

Figure 2.9: (a) Measured image of the IMX beam cut by slits on the horizontal axis, obtained with the Medipix3RX detector; (b) Beam intensity profile in the vertical axis, fitted by a Gaussian function (red).

Discriminating Mode provided the energy spectrum. The comparison results are presented in section 3.1.6.

In order to simulate correctly the deposited dose at the oxide layers of the chip, and to optimize simulation time, the photon beam was simulated with the source energy spectrum considering analytically the attenuation by the possible additional filters.

At the oxide and metal layers of the ASIC, the cut-off energies for electrons ($EABS(e-)$) and photons ($EABS(ph)$), which means, the smallest energy for generating daughter particles considered by the algorithm, under which a total absorption is imposed [20], were configured to the smaller value possible: 50 eV. This is necessary due to these layers thickness of few nanometers. The deposited energy by a particle traveling through them can be very low, but cannot be overlooked.

Similarly, the W_{cc} parameter, which determines the cut-off energy for losses in collisions, the W_{cr} parameter, which limits energy losses by photons, as well as C1 and C2 parameters, which limit the average energy loss per particle step [20], were set to zero for these materials.

These modifications increase the detail level of the simulation, and consequently increase the simulation time. Therefore, the initial simulations for defining the additional filtration and controlling the dose rate were performed with a smaller detail level, for 15 different possibilities of filter thicknesses, underestimating the dose. The 3 mm thick filter of Silicon was chosen for the low dose experiment, depositing 2.36±0.05 Gy per second for a maximum ring current of

250 mA. The 1.25 mm thick Silicon filter was selected for the high dose experiment, since it corresponded to 23.3±0.5 Gy per second for the maximum ring current. Only then detailed simulations were performed to these specific setups.

The dose rate was computed using the equation (2.2.6), adapted from Attix, 2008 [64] based on the PENELOPE's output *Tally Energy Deposition*, which provides the energy deposition per body material E_{dep}, in eV per simulated history:

$$\dot{D}_{SiO_2(PENELOPE)}(\frac{Gy}{s}) = \frac{10^3 \times 1.602 \times 10^{-19} \times \varphi_{Total} \times E_{dep}}{\rho \times \delta \times S} \tag{2.2.6}$$

where the 10^3 factor is an unit conversion from grams to kilograms, 1.602×10^{-19} is the conversion factor from eV to Joules; ρ is the material density, in g/cm^3; δ is the total thickness of material, in this case, the oxide layer thickness (cm); S is the irradiated area and φ_{Total} is the total number of expected photons per second incident on the sensor, obtained from the simulated spectrum (Figure 2.14), taking into account analytically the filters transmission. To obtain this value, the spectrum was integrated through the Trapezoidal Rule approximation [65], and divided by the bandwidth of energy (0.1% of the energy step).

The total dose of each irradiation, in Gy, can be obtained by equation (2.2.7):

$$D_{SiO_2}(Gy) = \dot{D}_{SiO_2(PENELOPE)} \times t \times f \times I_{ring}(mA) \tag{2.2.7}$$

In equation (2.2.7), the simulated deposited dose rate is multiplied by the irradiation time, t, by the ring current at the irradiation time, and by a beam distribution factor f, that corrects the simulated beam intensity to take into consideration the beam's vertical distribution. The beam was considered horizontally uniform, and the intensity was considered proportional to the relation between the slits horizontal gap (6 mm) and the horizontal size the beam would be at this position without any optical elements, just considering its theoretical horizontal divergence.

Figures 2.10 and 2.11 illustrate the beam distribution factor calculation. Figure 2.10 exhibits a normalized intensity map, considering only the horizontal slits opening of 6 mm, and considering the total sum of intensities at the image equals 1. Figure 2.11(a) simulates the vertical slits opening of 3 mm on the intensity map, and 2.11(b) shows a real beam image with these slits configurations at the experiment day, for comparison. The sum of pixels intensities of the selected area corresponds to $f = 75.2\%$ of the total beam.

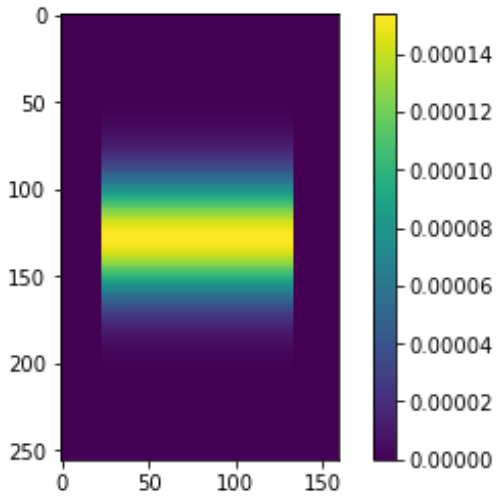

Figure 2.10: Map of IMX beam intensity per pixel, normalized, considering an horizontal definition of slits to a 6 mm gap and full opening in the vertical axis. Each pixel value corresponds to the normalized number of photons that would hit it.

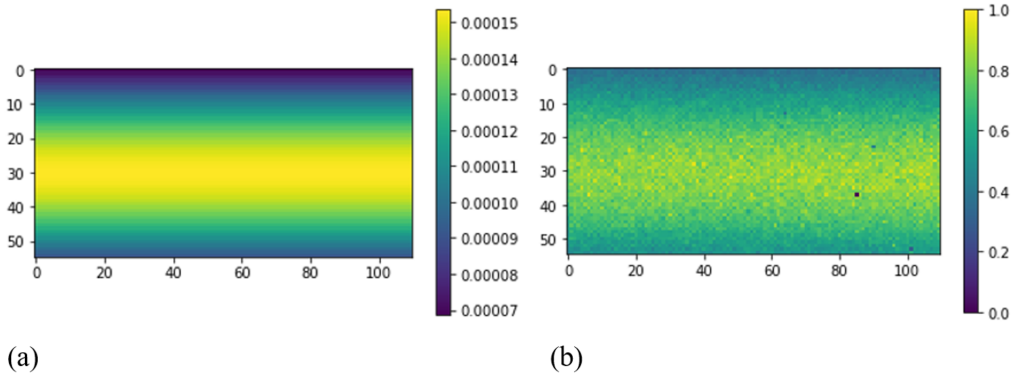

Figure 2.11: (a) Cut of the intensity map considering the vertical slits defining a 3 mm gap. (b) Normalized image of the IMX beam measured with Medipix3RX, for comparison. The defined area contains 75.2155% of the intensity, corresponding to the f factor applied in the dose calculation.

2.3 Experimental Studies

The experimental evaluation of the damage to the detector data was performed in two sets of measurements: low dose and high dose, controlling it by the defined sets of filters: 3 mm of silicon for the low dose and 1.25 mm of silicon for the high dose set. Two beamline days were scheduled for each set of measurements. In both sets a Medipix3RX single chip bonded to a 200 μm silicon sensor was used. The detector was configured to the default operation mode: Single Pixel Mode (without charge-sharing correction), operating with one discriminator and one 12-bits counter per pixel. The measurements were taken one month apart. A photographic

register of the experimental setup is exhibited in Figure 2.12.

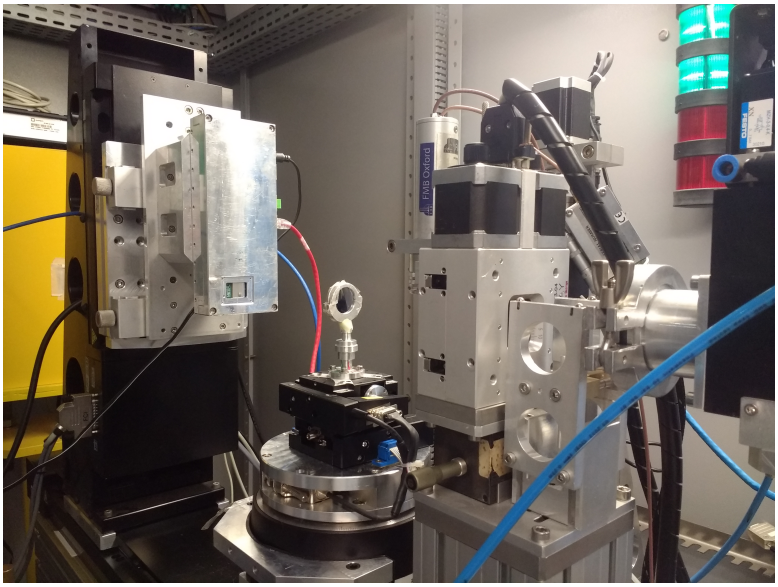

Figure 2.12: Photographic register of the beamline experimental setup for the dose measurements, evidencing the filters and the Medipix3RX single chip system.

The irradiation steps at each set were controlled by limiting the exposure time to the polychromatic bending magnet beam (white beam). Each white beam irradiation step was followed by a detector's performance characterization with monochromatic beam:

- The shutter was opened and the selected area is irradiated with the white beam for a controlled amount of time. Notes on the ring current are taken;
- The beamline was set to monochromatic mode (mono beam): the monochromator is placed in front of the beam, the detector is moved so the monoenergetic beam can hit exactly the same pixels; the energy of 8.33 keV is selected. A set of 350 μm silicon filters is placed in front of the beam;
- Images of the mono beam were taken with the detector, in order to obtain data for the noise characterization;
- An energy spectrum of the mono beam was obtained with the detector, by scanning the threshold current value, for the spectrum characterization;
- The beamline was set back to the white beam configuration for the next irradiation step.

Different regions were irradiated for each set of measurements, so their effect could be analyzed separately. The low dose experiment contemplated 30 irradiation steps of variable exposure times, reaching 809 ± 6 Gy. The steps were splitted into two shifts, separated by a 700 minutes recovery break. The first shift contemplated 12 steps in a dose rate of 0.53 ± 0.03 Gy/minute, and the second shift contemplated the last 17 steps with a 0.57 ± 0.02 Gy/minute dose rate.

The high dose experiment was also divided into two shifts; however, the detector has presented serious damage fast. A different position of the pixel array was selected for the second shift, which opened the possibility of comparison and endorsement of the observed effects. The first position has reached 6178 ± 29 Gy in 40 dose steps; the second position reached 6228 ± 19 Gy in 51 steps. The dose rate was greatly varied in the first position. A dose rate of 12.8 ± 0.6 Gy/minute was adopted for the first 9 steps; a break of 96.7 minutes was taken, including characterization measurements without white beam irradiation for recovery analysis. The next 9 steps were performed with a 4.6 ± 0.3 Gy/minute rate, followed by a second break of 224.4 minutes. The last 20 steps were performed in sequence with a 5.2 ± 0.1 Gy/minute dose rate. A characterization measurement was taken 327.4 minutes after the last white beam irradiation step for recovery studies. At the second position, an average of 5.84 ± 0.07 Gy/minute was maintained throughout the shift without significant time breaks. Figure 2.13 exhibits the calculated dose as a function of the experiment timeline for the three exposed regions.

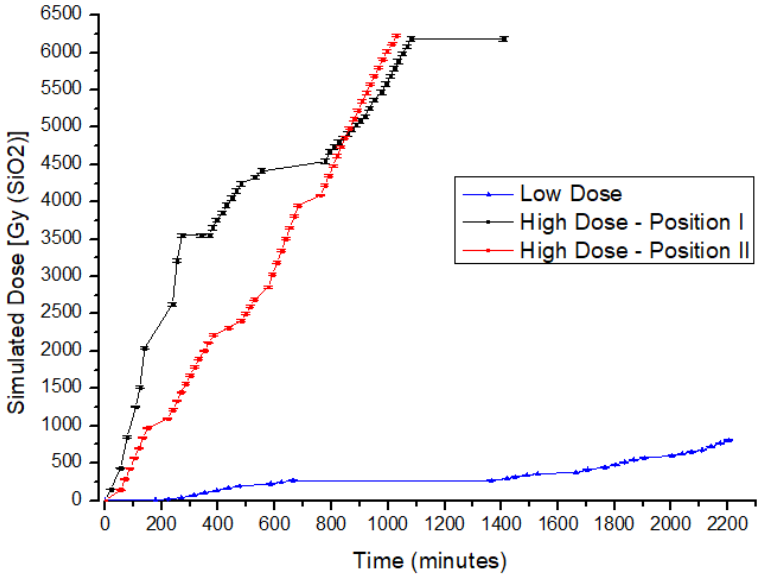

Figure 2.13: Dose evolution with time for the three experiments.

2.3.1 Parameters for Data Damage Evaluation

The detector data damage using image analysis was evaluated with different parameters, for comparison. The damage to the observed image was analyzed according to the relative noise on a monochromatic beam flatfield and its evolution with dose.

Relative Noise and Contribution of Structural Noise

Evans *et al.* [66] have presented a noise modeling for X-ray CCD detectors with medical applications. At this work, an extension of this model to the hybrid-pixel detector type was considered.

According to Evans *et al.* [66], an image detector noise can be divided into three major sources, with different behaviours: the electronic noise, the quantum noise and the structural noise. The three contributions can be distinguished according to the standard deviation of the pixel values evolution with the average pixel value.

The quantum noise evolution with counts is described by the Poisson statistics, being approximately defined by $\sigma = \sqrt{\mu}$ [19]. This contribution is related to the stochastic process of the photons incidence, and should not be expected to have an influence on the detector electronic process.

The electronic noise is usually associated to thermally generated electrons in the electronics [16, 66]. It is expected to be a low energy additive noise source, independent of the average counts.

The structural noise is related to spatially fixed variations in the gain between pixels of the imaging system [66]. For the hybrid-pixel detector, this refers to inherent differences between the pixel electronics, which effects are reduced by the equalization matrix [16, 35] and/or flatfield masks. It is described as a linear function of the average counts [66].

The normalized standard deviation $\frac{\sigma}{\mu}$ as a function of the average μ can be adjusted to equation (2.3.1):

$$\frac{\sigma}{\mu}(\mu) = \sqrt{\frac{k_e^2}{\mu^2} + \frac{k_q^2}{\mu} + k_s^2} \tag{2.3.1}$$

This equation provides coefficients determining the influence of each noise contribution to the total standard deviation. For a photon-counting hybrid pixel detector, the electronic

noise coefficient k_e is expected to be near zero, once every electronic noise should be under a determined energy threshold. The quantum noise coefficient k_q should be closer or equal to 1 for a Poisson noise. The structural noise k_s is the one expected to contribute mostly to the detector effect on image quality, as the detector response degrades with the dose increase.

It has been reported that the equalization matrix optimization is modified with the noise level [35]. In fact, it is expected that the dose deposition will provoke alterations in the irradiated pixels electronics. The structural noise contribution to the image and its evolution with dose was chosen for evaluating the radiation damage.

The noise characterization between dose steps was made varying the acquisition time from 0.001 seconds to 4 seconds, obtaining a curve of the standard deviation over average ratio $\frac{\sigma}{\mu}$ as a function of the average counts μ and comparing it to a previously obtained curve for a "zero dose" reference.

An example of $\frac{\sigma}{\mu}$ curve is presented in Figure 2.14, obtained from images taken with Medipix3RX and a X-ray generator source. Data was fitted with the OriginPro 8.5 ® software (OriginLab, Northampton, MA), for the whole Medipix3RX detector area of 256 × 256 pixels.

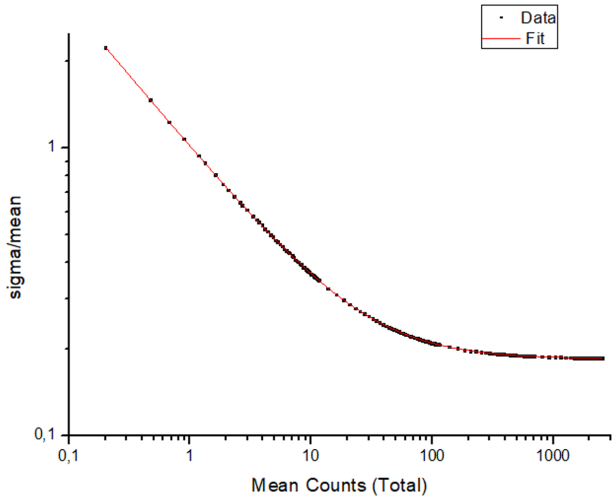

Figure 2.14: Measured noise $\frac{\sigma}{\mu}(\mu)$ before the dose experiment, obtained with a Siemens X-ray Generator source; and its fit to equation 2.3.1, in red.

For the experimental dataset, a faster data treatment was applied. A python3 routine was elaborated, using the SciPy library [67] for the curve fit and iteration through the dose steps. The same monochromatic beam was used to obtain the noise (σ) and average (μ) values for all

the dose steps, so possible non-uniformities of the beam intensity can be considered as a fixed background influence on the $\frac{\sigma}{\mu}$ factor.

Relative Noise and Euclidean Distance

An usual metrics for measuring differences between images is the Euclidean distance, due to its simplicity [68]; it is characterized for being highly sensible to small perturbation on images. This metric was also considered, for comparison. The distance was measured from the initial flatfield image of the beamline monochromatic beam for a zero dose step, using equation (2.3.2):

$$d_{Euclidean} = \sqrt{\sum_{i,j} (imgDoseX_{i,j} - imgDose0_{i,j})^2} \tag{2.3.2}$$

where $imgDoseX_{i,j}$ represents the photon count value of pixel (i, j) for the $X - th$ dose step, and $imgDose0_{i,j}$ represents the value of the same pixel (i, j) at the reference image for dose equal to 0.

Effects on the Measured Energy Spectrum

Pixels can also have their count value shifted by the radiation, due to leakage currents in the electronics and transistors driven to continuous active states [41, 69]. Histograms of the pixel counts and their evolution with dose increases can also provide interesting information and a possible pattern recognition of the damage response.

As for the effect on measured spectrum, the pixel analog gain variations are expected to alter the threshold current relation to the incident photon energy, due to leakage current effects; for a monochomatic beam of fixed energy, the spectrum peak position read by the detector would change with the deposited dose. Also, due to extra inequalities between pixels generated by dose deposition, not corrected by an outdated equalization matrix, the Gaussian width of the spectrum is expected to enlarge, once its main component is the threshold mismatch between pixels [16, 35].

The spectra were obtained from the threshold current scans. The sum of the pixel counts at the irradiated area for each image is plotted as a function of its threshold current. The derivative of this plot provides the Gaussian spectrum of the monochromatic beam, added to a charge dispersion effect, which can be approximately modeled by an error function [70]. An

example of the expected shape of the spectrum is presented in Figure 2.15.

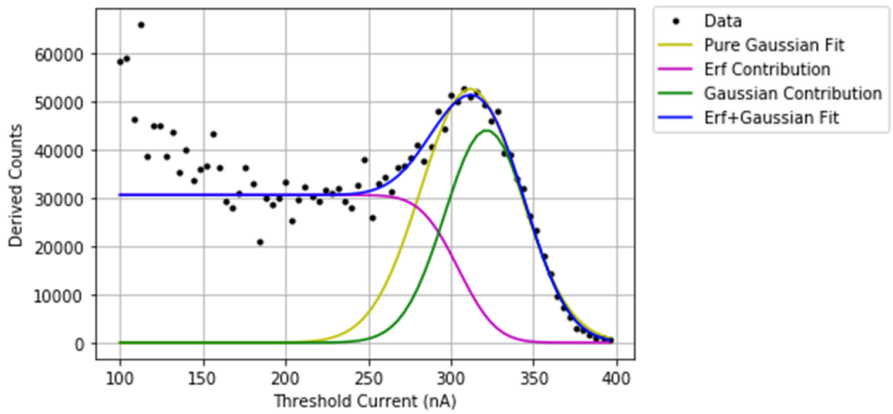

Figure 2.15: Example of obtained spectrum from Medipix3RX, scanning the threshold current of the detector. The blue curve is a fit considering the charge dispersion effect in the sensor, by summing a Gauss error function (pink) with a Gaussian peak (green). The yellow curve corresponds to a pure Gaussian fit considering one side of the peak, for comparison.

In Figure 2.15, the experimental data is plotted as black dots; data was fitted to the sum (blue) of an error function (purple), modeling the charge dispersion, and a Gaussian (green), representing the real photons spectrum contribution convoluted with the detector energy resolution. A Gaussian fit considering only the high energy side of the peak was plotted for comparison. The fitting algorithm to this function was elaborated in Python3, using the SciPy library [67]. It was assumed that charge dispersion in the sensor does not vary with the deposited dose in the oxide layers. Therefore, the parameters for the error function were obtained for the zero dose spectrum and fixed for the other steps.

Chapter 3

Results and Discussion

This chapter presents the results of this work and their interpretation. As the previous chapter, it was also divided in two groups: results of the Monte Carlo simulation validation of the charge dispersion inclusion, and experimental results of the damage measurement as a function of the deposited dose. The inclusion of the dispersion effects in the Monte Carlo simulation was validated by comparing the expected effect of this physical phenomena with the obtained at the simulation output. Variations on the photon energy, the bias electric field on the sensor and also the detector energy threshold and pixel size, and the impact of this variations was observed and compared to the expected changes in image and spectrum, based on the literature. The modulation transfer function, a typical evaluation of a detector spatial resolution, was also measured for an experimental image and for the image obtained by the simulation. The experimental results are divided in three experiments: a low dose experiment and two positions of the high dose experiment, which differs in dose rate. The results of the experiments are shown, discussed and compared. The impact of a new equalization matrix is presented, radiation limits for the detector are obtained and a comparison of these limits with the expected dose rate for synchrotron and medical applications are presented.

3.1 Detector Simulation

3.1.1 Variation with Electric Field

The implemented algorithm for modelling the charge dispersion was validated in order to ensure it corresponds to the expected physical behaviour. Figure 3.1 exhibits a photon-counting image obtained from the original tally, without considering charge dispersion effects, for a punctual-size beam hitting a pixel corner (marked by an X signal). Figure 3.1(b) presents the same image in logarithmic scale, to enhance visualization of small charge migrations on the sensor.

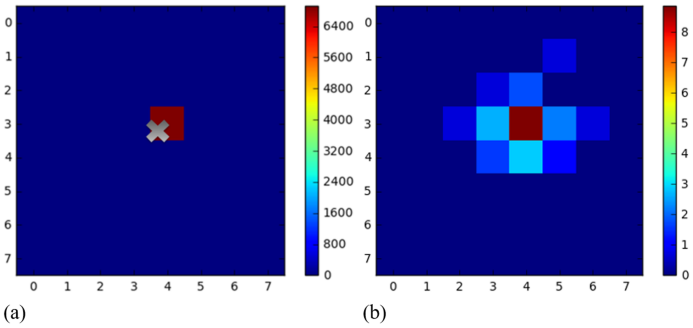

Figure 3.1: Image obtained from PENELOPE simulation using the original Tally Pixelated Imaging Detector code, using (a) linear and (b) logarithmic scale, for visualization of electron scattering effects.

After including the charge dispersion and drift related to the applied electric field, a higher count of photons in the neighbour pixels from left and below is observed for the same punctual beam in the pixel corner, as shown in Figure 3.2. Images from the photon-counting mode of Tally Pixelated Imaging Detector were obtained with the modified tally, for electric fields of 10, 100 and $1000 V/cm$. Maps of the generated electron-hole pairs counts per pixel were also obtained and are exhibited in Figure 3.3.

The electric field variation effect can be seen more distinctly in Figure 3.3. This can be due to the threshold energy of 1 keV selected in the photon-counting image, since pixels that didn't detect enough electron-hole pairs to reach 1 keV didn't present any counts. It is possible to conclude that the simulation of charge dispersion related to electric field behaved like expected: the smaller the field, smaller the drift, and larger the dispersion, according to equation (2.2.4).

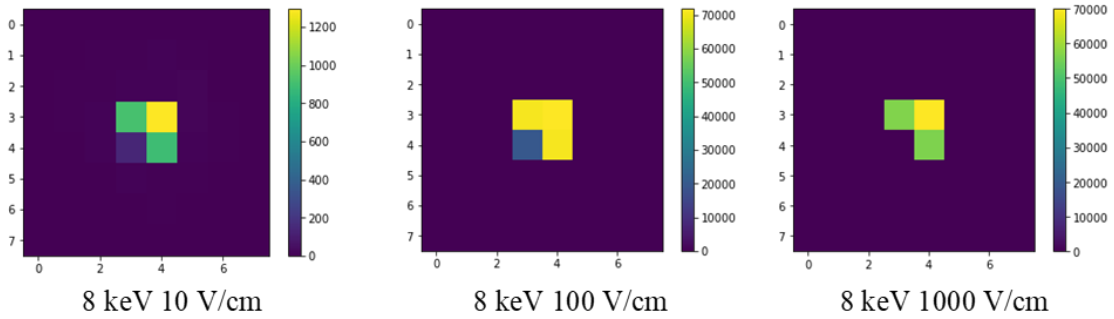

Figure 3.2: Images of the sensor in the photon-counting mode of the Tally Pixelated Imaging Detector modified for the inclusion of dispersion effects, for different values of electric field.

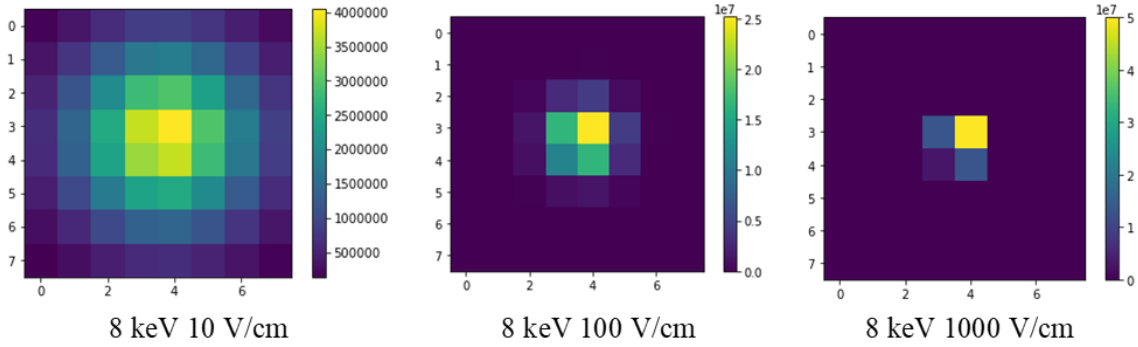

Figure 3.3: Images mapping the number of electron-hole pairs assigned for each pixel, for different values of electric field.

3.1.2 Variation with Energy

The Gaussian dispersion width depends of the interaction height Z, which is related to the photon energy: the higher the energy, the deeper will be the interaction, and smaller will be the Z value to be crossed by the photo-electron until the anode. Therefore it is expected that the charge dispersion increases with the decrease of the photon energy. Simulations were performed with 4, 6 and 8 keV photons, maintaining an electric field of 1000 V/cm. Images for the photon counting mode outputted from the tally and the electron-hole pairs map obtained for each energy are shown in Figure 3.4.

When comparing the photon-counting image to the electron-hole pairs map, a variation with the beam energy is observed only in the former, and almost none in the latter. This agrees with the hypothesis that the observed variation is more related to the applied threshold, evidencing the dispersion in higher energies. Based on the electron-hole pairs map, it is observed that Z height did not vary significantly. Indeed, the Z variation is limited from 0 to the sensor thickness, which in this case corresponds to 300 μm, consequently having a low impact on the

physical effect described by equation (2.2.4).

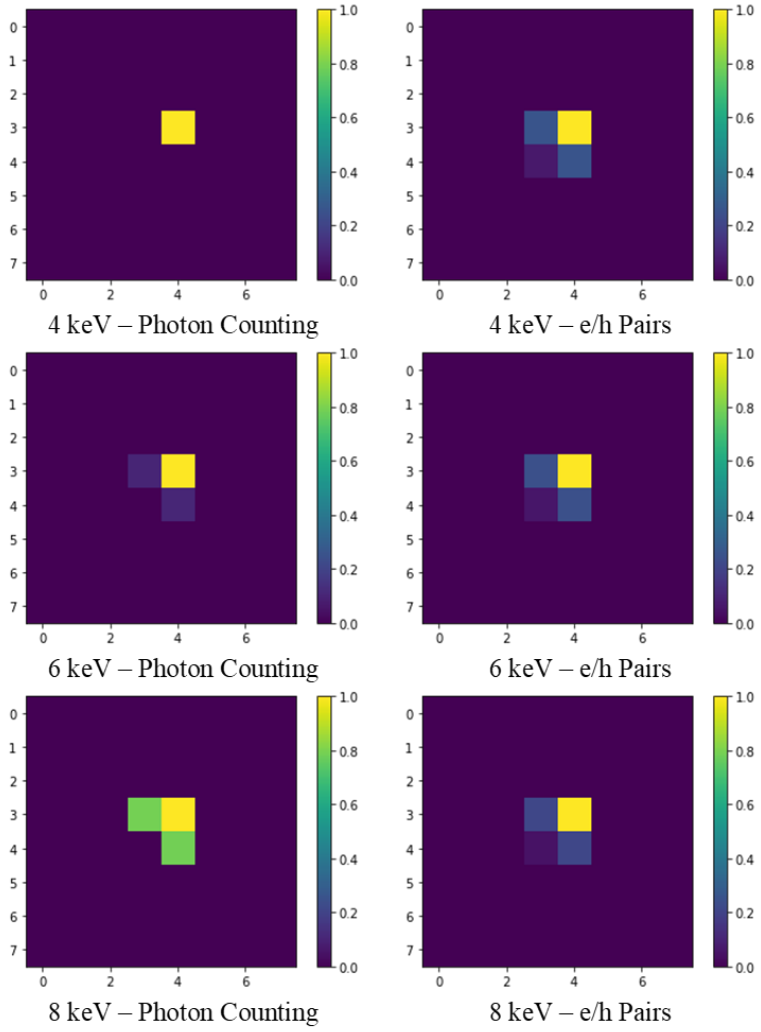

Figure 3.4: Images of the photon-counting mode and of the number of electron-hole pairs assigned for each pixel, for different values of photon energy.

3.1.3 Variation with Position and Beam Size

A pixel scan with a pencil beam was simulated, based on the tests performed by Marinho & Akiba [37]. The beam position was scanned from the center of the pixel to the center of its neighbour (-27.5 μm to 27.5 μm); a comparison was made for different beam diameters (0, 5 and 10 μm) and different thresholds. The main pixel count and the total number of counts were monitored. The results are shown in Figure 3.5. The beam energy was fixed at 8 keV.

The observed result presents a behaviour similar to the results from Marinho & Akiba [37],

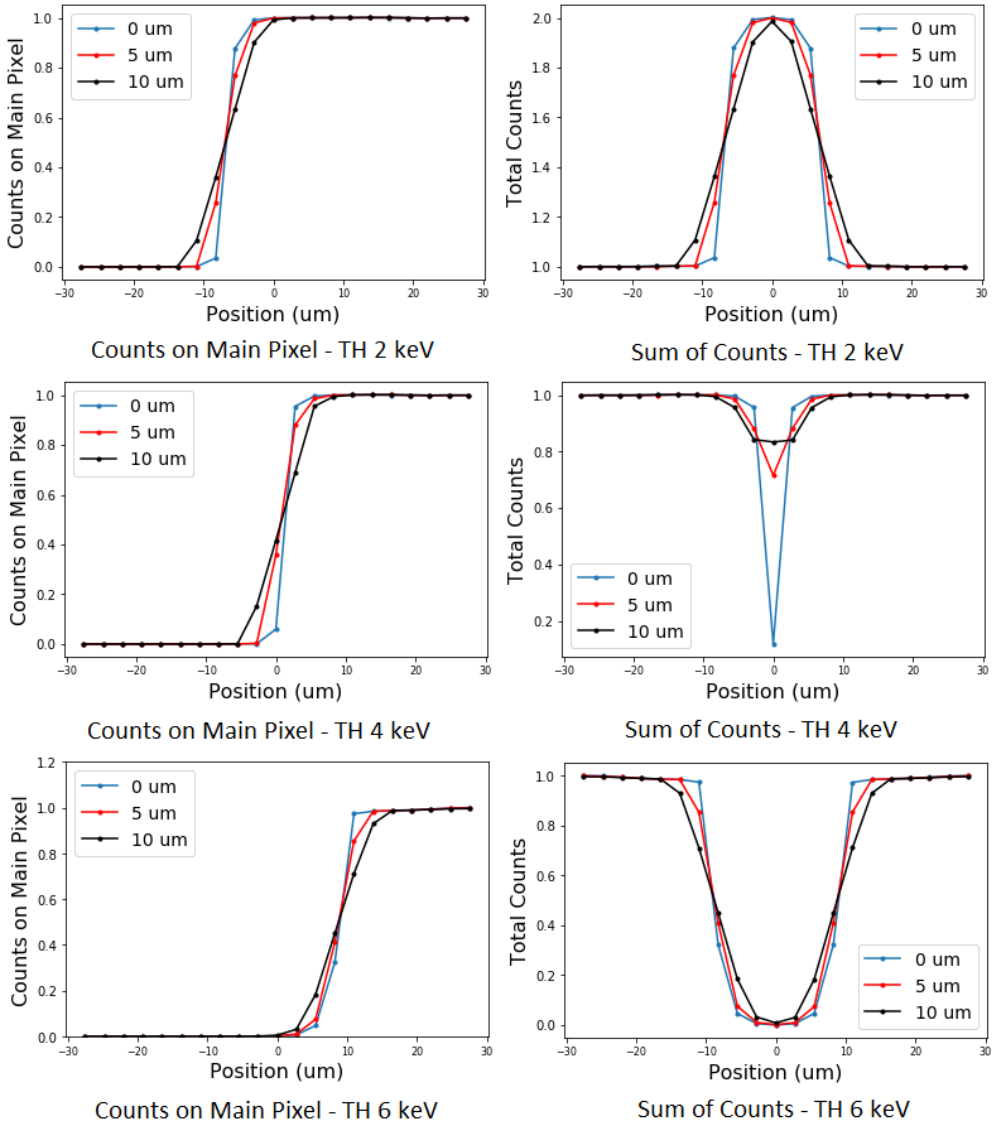

Figure 3.5: Normalized counts as a function of the position in a pixel, scanning from the center of a pixel to the center of the neighbour pixel, varying the beam diameter (0, 5 and 10 μm)

obtained for the GEANT4 simulation code, which are presented in Figure 3.6, for comparison. These results are also compatible to the experimental data presented by Gimenez *et al.* [71].

Figure 3.5 points out the threshold influence on the photon counting measurement, corroborating what was observed in sections 3.1.1 and 3.1.2. The optimal threshold for reducing the charge dispersion influence to the image is 4 keV, or half the photon energy. Higher thresholds decrease the pixel counting area due to charge dispersion to neighbour lateral pixels, and lower thresholds result in a super-estimation of the counts. Even though hits in the pixel corners can provoke a dispersion of the charge between three or four pixels, dividing the deposited energy

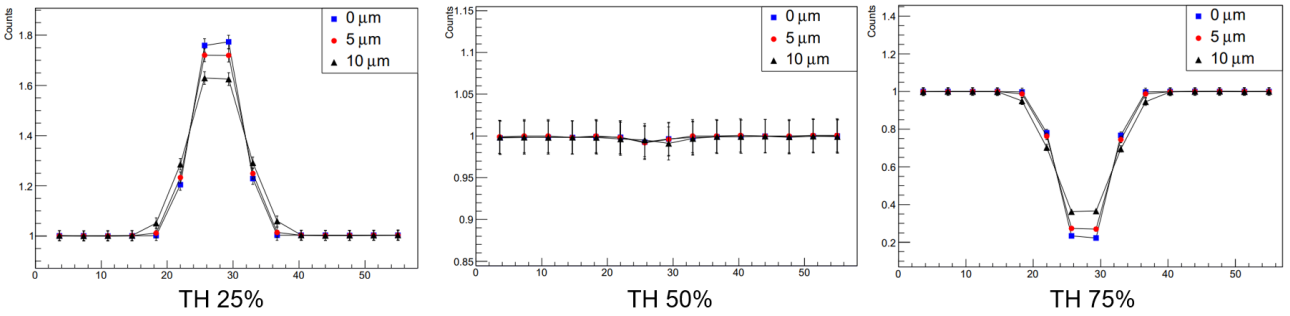

Figure 3.6: Measurements of a similar verification, varying the beam position, size and the detector threshold, for a code implemented for Geant4 simulation tool [37], for comparison.

into lower then half-energy values, such events are less likely. This result is in agreement with the literature description for hybrid pixel detectors, that affirms the optimal threshold is equal to half the photon energy [32, 71, 72].

3.1.4 Pixel Size and Spectrum Evaluation

The main effect of the charge dispersion on the measured energy spectrum is the inclusion of low energy counts, as described by Ballabriga [16], Marinho & Akiba [37] and Frojdh *et al.* [73]. This effect is expected to have a greater impact for smaller pixel sizes.

Simulated spectra were obtained by setting the *Tally Pixelated Imaging Detector* to the photon energy discriminating mode, for an incident 8 keV monochromatic photon beam. In order to evaluate the pixel size impact on the spectrum, simulated beams illuminating 55×55 μm^2 for a pixel size of 55 μm and for a pixel size of 110 μm were compared. The resulting spectra is presented in Figure 3.7. The detection effect on the pulse width was taken into account.

The impact of the pixel size on the spectra is accorded to the expected. A double-sized pixel presented less charge dispersion impact, decreasing the dispersion plateau for lower energies, which is compatible to the experimental data presented by Frojdh *et al.* [73]. The differences between the experimental data and the simulated spectra increases for low energies and can be interpreted as related to the electronic noise.

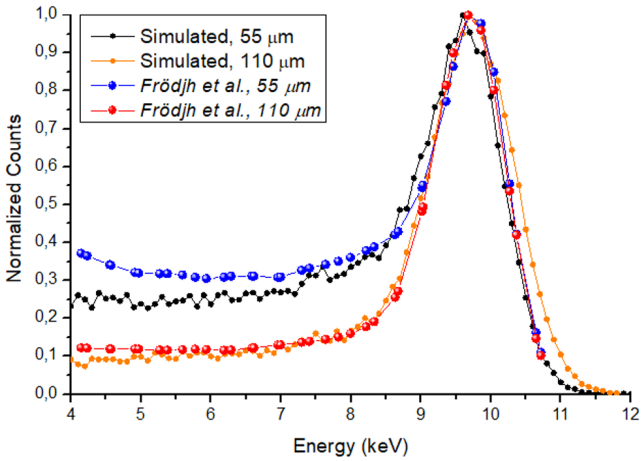

Figure 3.7: Simulated spectra obtained with the charge dispersion implemented algorithm, for two different pixel sizes, and comparison to experimental spectra for the same pixel sizes described in the literature [73].

3.1.5 Modulation Transfer Function Verification

Another possible verification of the functionality of the algorithm and its impact to the image is comparing the Modulation Transfer Function (MTF) of an experimental image obtained from the detector with the simulated image. This function is a widely known method for characterizing a detector's spatial resolution [16, 74, 75]. One possible setup for obtaining this data is the slanted-edge technique [75], where the detector is partially covered by an edge of an absorbing material as sharp as possible, in a slanted position; then a sub-pixel spatial resolution can be obtained based on the edge projections of each covered pixel row, as illustrated in Figure 3.8.

The data processing includes an interpolation of the various pixel rows, which boundary condition is the linearity of the absorbing material. The sum of these projections is the Edge Spread Function. The derivative of the Edge Spread Function provides the Line Spread Function, and its Fourier transform results in the MTF. This results in a actual measurement of the detector's spatial resolution, which is directly affected by the charge dispersion between pixels.

The experimental measurement was performed at the X-ray Absorption, Fluorescence and Spectroscopy beamline XAFS1 at the Brazilian Synchrotron. The beam energy was set to 8 keV. The detector was slightly tilted so the beamline slits could be used as absorption edge. The normalized slanted edge image obtained with the experiment is presented in Figure 3.9(a).

The *Tally Pixelated Imaging Detector* was set to the photon counting mode, and an edge

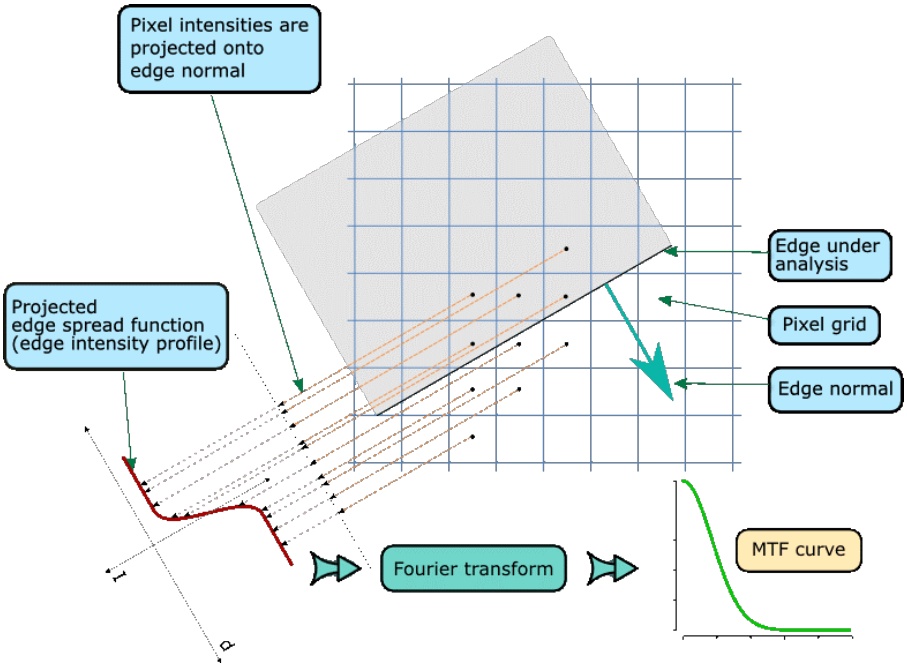

Figure 3.8: Diagram illustrating the MTF measurement setup and the image post-processing, to obtain as a result the MTF curve as a function of the number of line pairs per mm (spatial frequency). Courtesy of Frans van den Bergh.

with the same angle as the experimental image was simulated with and without the charge dispersion algorithm. In this case ($1E+08$ histories) were considered, in an attempt to reproduce the order of magnitude of the quantum noise of the experimental image ($\frac{\sigma}{\mu} = 0.0061$). The normalized slanted edge image obtained by simulation is presented in Figure 3.9(b).

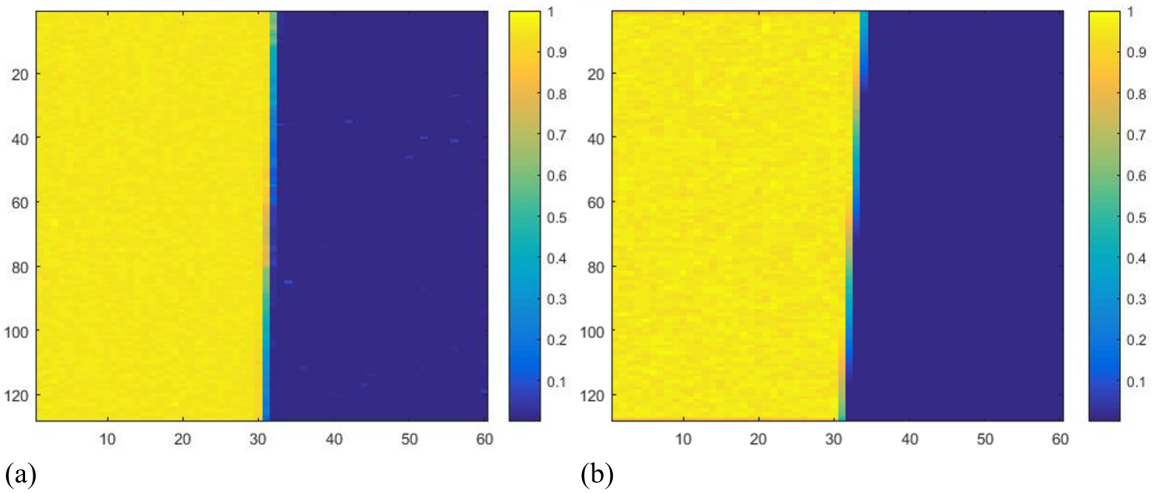

Figure 3.9: (a) Experimental image obtained with Medipix3RX on the XAFS1 beamline, using the beamline slits as shield; (b) Simulated image of the slanted edge, using the photon counting mode and the modified tally for charge dispersion effects consideration.

The Slanted Edge Script routine for MATLAB written by Patrick Granton was used for the data processing [76]. Figure 3.10 exhibits the results for the experimental image, the simulated image with and without dispersion, and the theoretical result expected for a squared-pixel detector, given by the cardinal sinus $sinc(\pi\frac{f}{2})$ [77]. The theoretical curve for the MTF presents higher values than the obtained experimental curve; this result was expected, once it corresponds to the ideal behaviour of the detector, not considering measurement artifacts such as the charge dispersion.

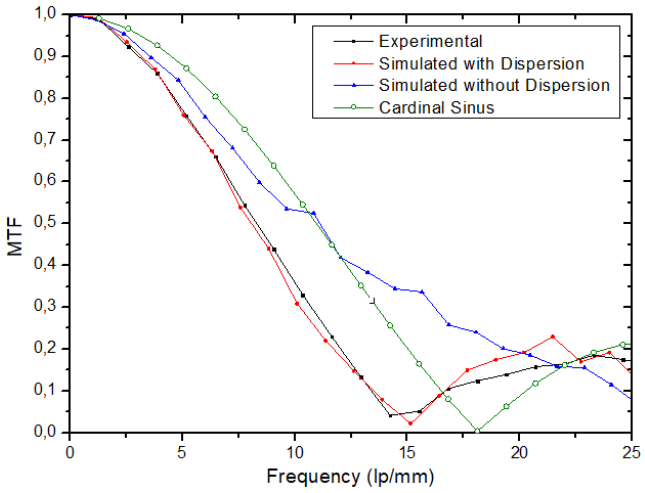

Figure 3.10: Comparison of the obtained MTF curves for the experimental image, the simulated image with and without the charge dispersion algorithm, and the theoretical curve.

Figure 3.10 results demonstrate that the charge-sharing effect simulation was correctly implemented, since the MTF curve obtained from the simulation with dispersion is similar to the experimental MTF curve, which are in agreement with experimentally measured MTF curves for this detector presented by Mir *et al.* [78]. In fact, the MTF curve obtained for the simulation without dispersion doesn't correspond to the theoretical or experimental expected behaviour, which indicates that it is not a good fit for the detector modeling at the simulation tool.

3.1.6 Correlation between Simulation and Experiment

In order to validate the use of the dose deposited at the oxide layers of the ASIC provided by the simulation as an estimation of the real deposited dose value, a comparison between the experimental data provided by the detector with the simulated data was performed. Figure 3.11 exhibits the experimental and the simulated spectrum of the IMX bending magnet white beam

attenuated by 4.05 mm silicon filters, taking into account the charge dispersion effect. The detector energy resolution was measured from a fit of a 8.33 keV monochromatic experimental spectrum and also considered in the simulation.

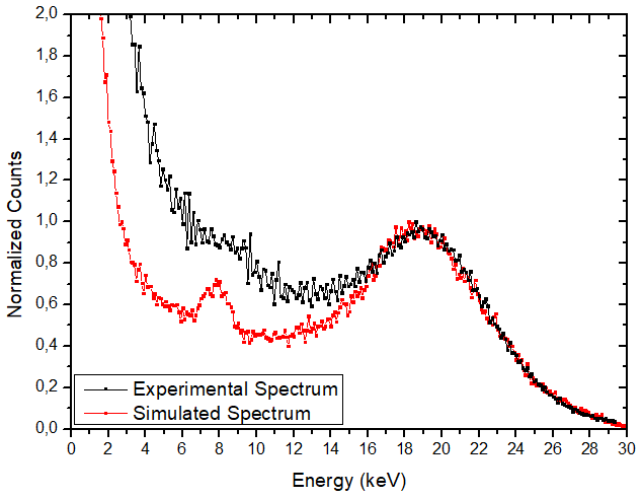

Figure 3.11: Comparison of a spectrum of the IMX filtered white beam obtained experimentally with the spectrum obtained from simulation, after the inclusion of charge dispersion effects to the code.

The charge sharing effect on the simulated spectrum is smaller than the presented by the experimental curve. The 8 keV peak corresponds to the fluorescence of the BEOL copper layers and is also present at the experimental spectrum, although attenuated by the larger charge sharing of the higher energies.

The experimental spectrum is affected by the electronic noise, which increases the number of counts for energies under 3 keV, and this effect is not modeled by the simulation. The simulated spectrum, on the other hand, presents an exponential grow of the counts exploding under 2 keV, which is related to the charge sharing effect.

The difference between the two curves decreases with energy, which points out to detector effect contributions not included in the simulation. Even so, the white beam energy peak and width was correctly modeled by the simulation source, validating the use of its result as an estimation of the reality.

Figure 3.12 exhibits (a) a experimental image obtained with Medipix3RX in Single Pixel Mode in comparison with (b) the simulated image with the *Tally Pixelated Imaging Detector*. It can be inferred that the Gaussian distribution was correctly reproduced. On top of this result, the vertical colimation by the beamline slits was included in the dose calculation by the

beam intensity distribution factor (section 2.2.5).

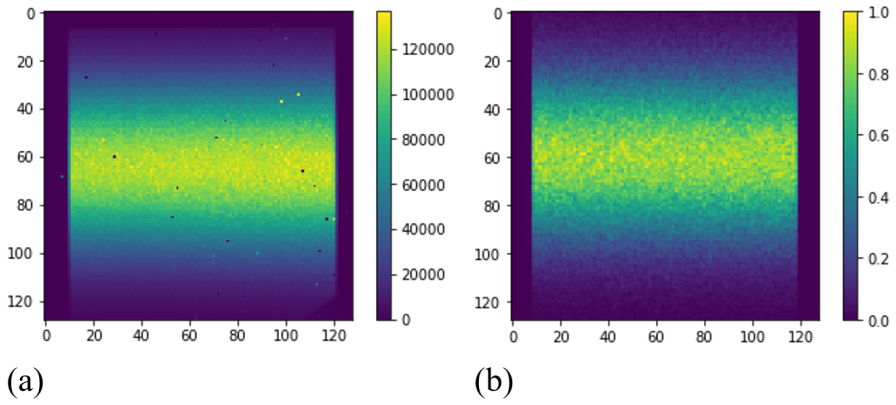

Figure 3.12: Comparison of (a) a experimental image of the IMX white beam, obtained with 4.05 mm filters; and (b) a simulated image obtained with the Tally Pixelated Imaging Detector for this source, replicating the vertical Gaussian distribution.

3.2 Low Dose Experiment

3.2.1 Impacts on Image

The experiment contemplated 30 irradiation steps of variable exposure times, reaching 809± 6 Gy. Figure 3.13 exhibits the noise curve $\frac{\sigma}{\mu}(\mu)$, adjusted for equation 2.3.1, for two distinct dose steps (1.55 ± 0.06 Gy and 293 ± 4 Gy). The appearance of two decay phases on the higher dose curve is observable. For this plots, only the irradiated healthy pixels were considered.

Figure 3.13 suggests an effect on the structural noise parameter k_s, given by the yellow asymptotic curve, with the increase of the deposited dose. However, when comparing the curves for the 30 steps, one can notice that this two-phase appearance occurs in intermediate dose steps: this can be better visualized in Figure 3.14.

The evolution of the relative noise curves with the dose shows the appearance of a discontinuity in the curve for intermediate dose steps, followed by a decrease of such discontinuity and a return to the continuous behavior. This is hypothetically related to a time recovery of the damage. Therefore, the time between exposures is a relevant factor for evaluating the damage. Figure 3.15 exhibits the deposited dose evolution in a timeline of the experiment, measured in minutes since the beginning, and compares with the temporal evolution of k_s parameter, obtained by fitting the first phases of relative noise curves, with counts smaller than 250.

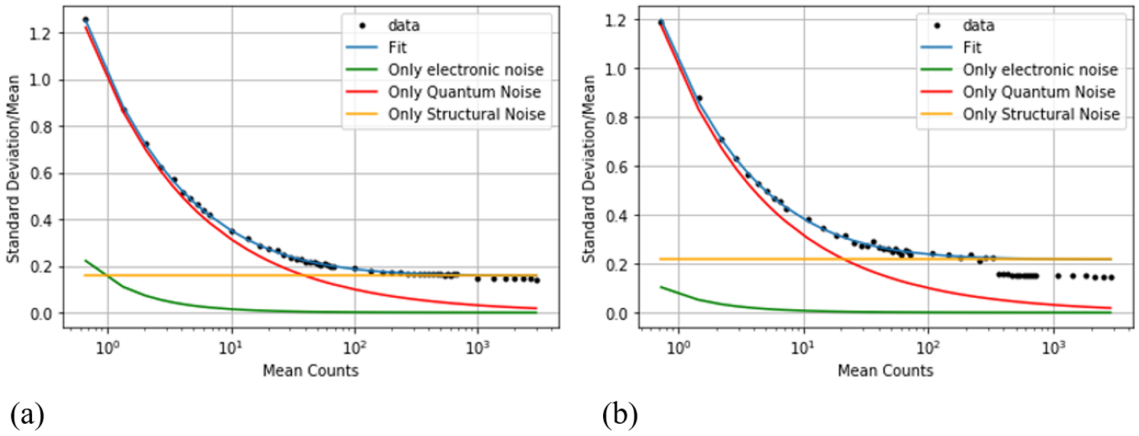

Figure 3.13: Relative noise curve $\frac{\sigma}{\mu}(\mu)$ adjusted for equation 2.3.1 for (a) an initial dose step and (b) an intermediary step, evidencing the occurrence of a split in two phases in curve (b).

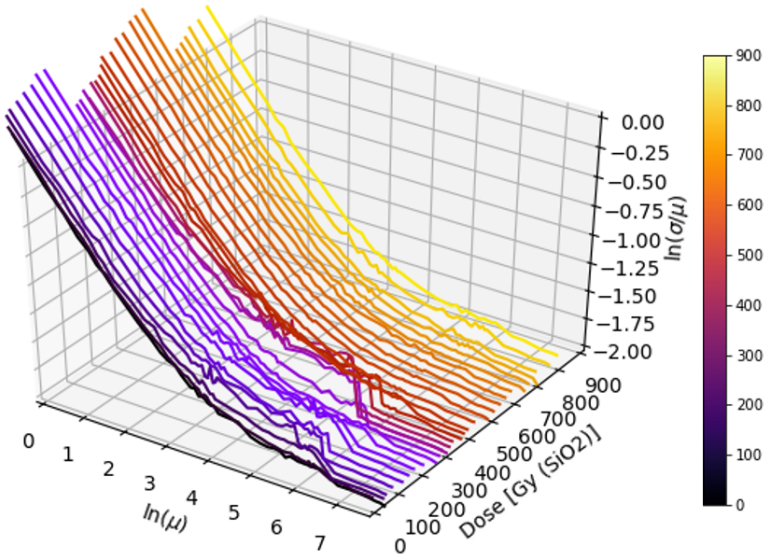

Figure 3.14: Logarithm of the noise curves $\frac{\sigma}{\mu}(\mu)$ as a function of the simulated dose at the oxide, evidencing the appearance of the split at the beginning, increasing around 250 Gy and a return to the normal pattern around 400 Gy.

Figure 3.15 does not present a clear correlation of both curves, statistically resulting in a correlation coefficient of -0.1141. Since the beam has a Gaussian distribution in the vertical direction, the detected counts are not uniform on all exposed area. Thus, in order to minimize the effect of beam heterogeneity, the contribution of structural noise k_s was investigates only for the higher dose region, from $(\frac{-\sigma}{2}, \frac{\sigma}{2})$ of the vertical Gaussian distribution of intensity (2.9), totalling 2640 pixels. The obtained result presented a considerable correlation with the deposited dose, with a correlation coefficient of 0.9607, as shown in Figure 3.16.

Evaluating the tridimensional plot of the noise curves for all dose steps, and comparing with

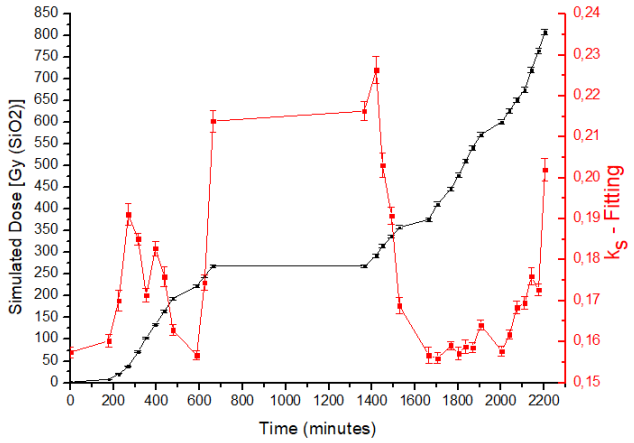

Figure 3.15: Evolution of the structural noise k_s parameter with time obtained from a fitting to equation 2.3.1, in comparison with the time evolution of the dose at the oxide. The line connecting the data points are only for better visualization of the evolution tendency of data, not corresponding to a curve fit.

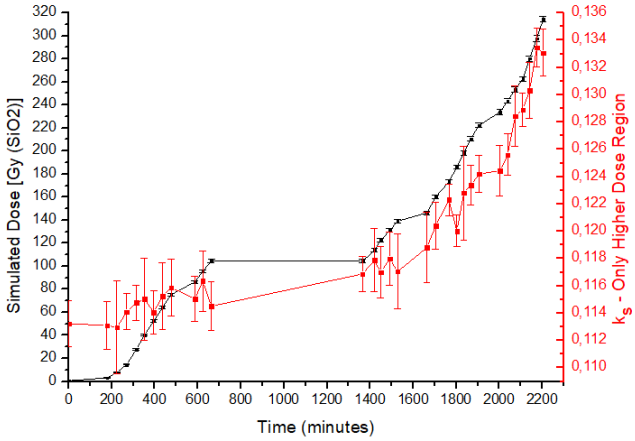

Figure 3.16: Evolution of the structural noise k_s parameter with time obtained from a fitting to equation 2.3.1 only for the higher intensity region, in comparison with the time evolution of the dose at the oxide layers. The line connecting the data points are only for better visualization of the evolution tendency of data, not corresponding to a curve fit.

the relative noise curves for the high intensity area of the beam, it can be verified that, despite the appearance of two phases in the intermediate dose region, the final region (asymptotic) seems to grow with the dose in a similar way for both situations. Figure 3.17 illustrates this behaviour; the increase of dose is represented by the colorbar.

The asymptotic of the noise curve is directly related to the k_s parameter, as can be deduced of equation 2.3.1 and visualized in Figure 3.13. A different approach was considered: a plot of the relative noise value only for high average counts. The images related to an exposure time of 2 seconds were selected. Since all the 4992 irradiated pixels are contained above the

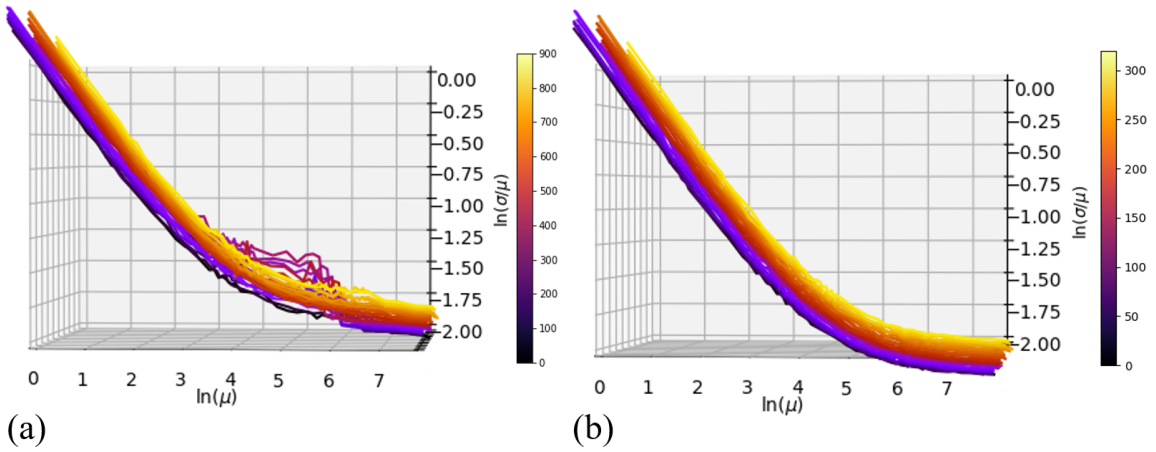

Figure 3.17: Noise curves profile, evidencing a growing behaviour of the asymptotic value of the curves for the higher dose steps, for both (a) all the irradiated region (4992 pixels) and (b) higher intensity region (2640 pixels).

half-maximum of the Gaussian distribution, they were all considered in the calculation, in order to improve statistics of counts. The Gaussian intensity distribution of the beam was considered in the simulation, hence the obtained value for the deposited dose is an average for this distribution.

Data was obtained throughout two days of experiment; it was considered that the ring current presents a 12-hour period decay, when the electrons are then re-injected through the linear accelerator. The synchrotron beam intensity is directly proportional to the ring current. Since it presents a 12-hour period decay and data was obtained throughout two days of experiment, it was taken into account that the ring current could have an effect on dislocating the average counts value for a fixed 2 seconds exposure, and consequently provoking an increase of the noise parameter, since it could correspond no more to the asymptotic value.

To check if this variation had an impact in the noise curve, the noise-to-average rate value was plotted as a function of dose step, and divided in color groups according to the injection period. The result plot can be verified in Figure 3.18.

Figure 3.18 shows that the noise value fluctuation presented no correlation with the ring current shifts, resulting in a correlation coefficient of 0.258. It can be inferred that the noise-to-average rate oscillation is only related to the deposited dose.

The evolution of the k_s parameter for all the irradiated area, obtained by the asymptotic method as (a) a function of deposited dose, and (b) in the experiment timeline in comparison with the deposited dose temporal evolution are presented in Figure 3.19. The parameter k_s

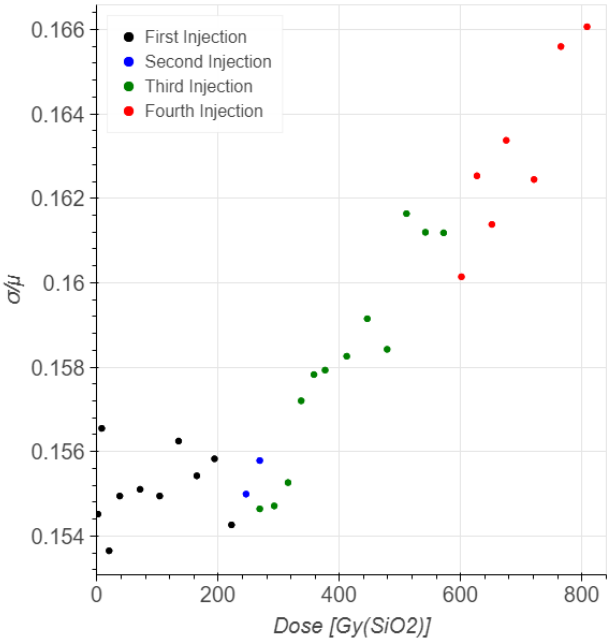

Figure 3.18: Evolution of the $\frac{\sigma}{\mu}$ noise value for 2 seconds acquisitions as a function of the deposited dose at the oxide. The color code separates the synchrotron ring shifts, evidencing that the injections and alterations on the beam intensity does not present impact on the obtained values.

is almost constant within the error limits for doses smaller than 337 ± 4 Gy. After that, it is observed an increase in a rate of $(1.7 \pm 0.2) \times 10^{-5}$ arbitrary units/Gy.

A strong correlation between the k_s parameter and the deposited dose was obtained, resulting in a correlation coefficient of 0.9224. It also presents a tendency of decrease, even though included in the error bars, of the structural noise parameter value after a large time between dose steps between 600 and 1300 minutes of experiment, which is supposed to be related to a recovery effect.

The Euclidean distance was measured from the initial image for a zero dose step, for each of the mono-energetic beam images obtained after the dose steps, always for 2 seconds exposure time. Figure 3.20 shows the results for the temporal evolution of the Euclidean distance, in comparison with the deposited dose timeline.

The Euclidean distance also demonstrates high correlation with dose (0.894), being applicable for measuring the damage effects to the image. This correlation coefficient, however, is smaller than the one obtained for the k_s parameter. This indicates that a specific quantity related to the structural noise may be a better measure of the damage. This result was expected, since the k_s parameter is related to a physical effect.

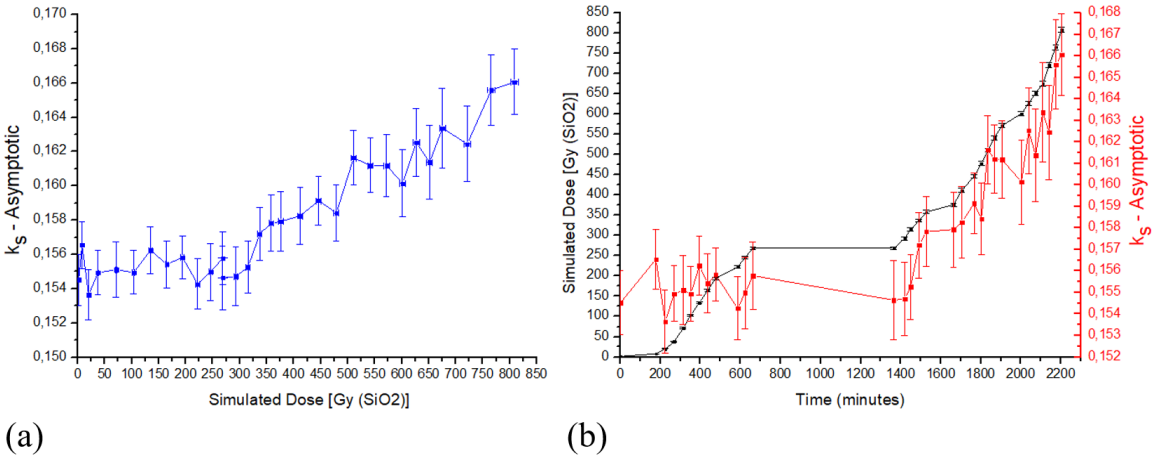

Figure 3.19: Evolution of the structural noise k_s obtained from the asymptotic value of $\frac{\sigma}{\mu}$ for 2 seconds acquisition (a) as a function of the deposited dose at the oxide, and (b) with time, comparing with the dose evolution. A strong correlation is evidenced, including recovery signs when in long periods without irradiation (600 to 1400 minutes). The line connecting the data points are only for better visualization of the evolution tendency of data, not corresponding to a curve fit.

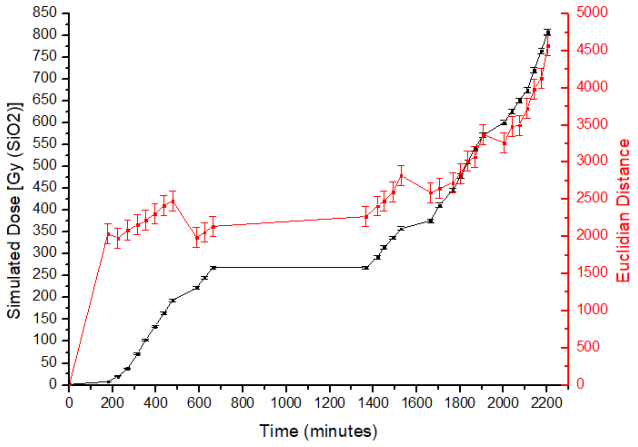

Figure 3.20: Time evolution of the Euclidean distance among the images obtained from the monochromatic beam with the same exposure time and a flatfield ("dose 0" image), as a comparison with the dose evolution at the oxide. The line connecting the data points are only for better visualization of the evolution tendency of data, not corresponding to a curve fit.

3.2.2 Impacts on Spectra

Figure 3.21 exhibits an image of the poly-energetic beam obtained with 4.05 mm Silicon filters before the experiment, illustrating the position of the irradiated pixels. Figure 3.22 exhibits a map of the threshold position of the energy peak of the spectrum for the same energy in each pixel, minus the previous average position for the whole detector ($TH_{pixel} - < TH_{pixel_{dose0}} >$), (a) before and (b) after the experiment. The irradiated region presents a subtle

higher difference, which demonstrates the alteration of these pixels gains.

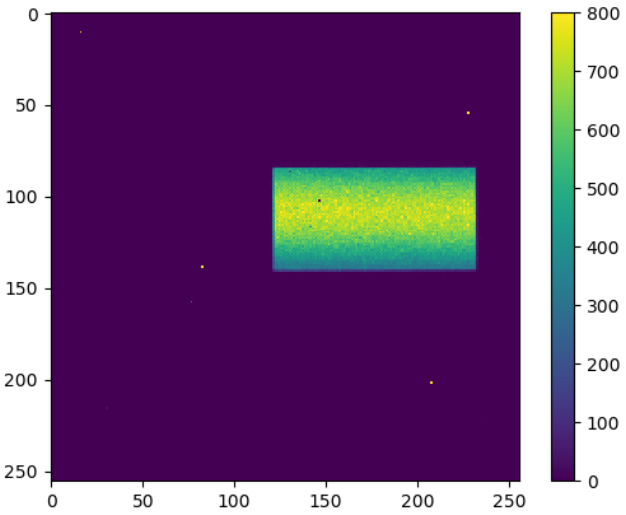

Figure 3.21: White beam image obtained with Medipix3RX, using 4.05 mm Silicon filters, before the experiment.

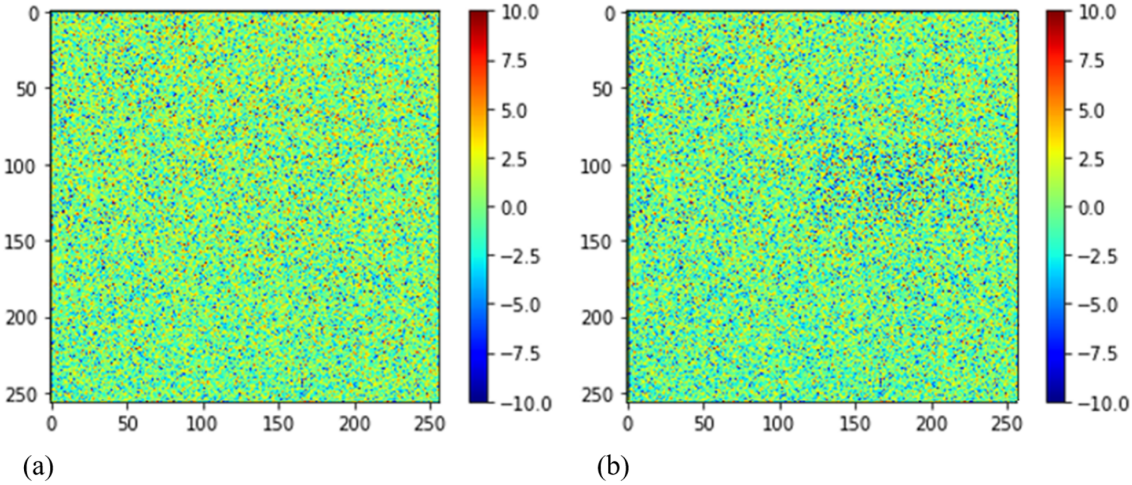

Figure 3.22: Map of the energy peak threshold of each pixel in relation to the mean threshold of the whole detector ($TH_{pixel} - T\bar{H}_0$) (a) before and (b) after the experiment, for the same input energy. The irradiated area at image (b) exhibits a slighter difference.

Figure 3.23 exhibits the peak position evolution with dose and time, obtained by fitting the spectra to a Gaussian function summed to an ERF function. Only the parameters obtained for the Gaussian part of the function are considered. The peak position decreases with dose increasing. This behavior is explained by an analog electronics gain alteration, changing the relation between the threshold current and the photon real energy. This is related to an increase on the leakage current of the transistors at the pixels electronics. A recovery effect

in the timeline region between 600 and 1300 minutes is noticeable. The calculated correlation coefficient is -0.851.

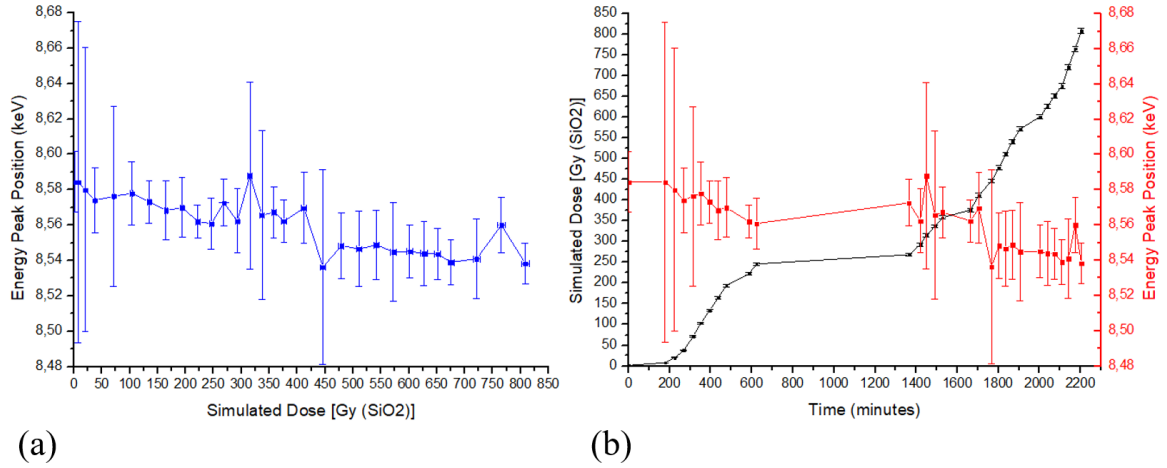

Figure 3.23: Evolution of the energy peak position, in threshold current units, with (a) dose in the oxide, and (b) time of the experiment, comparing to the time evolution of the dose.

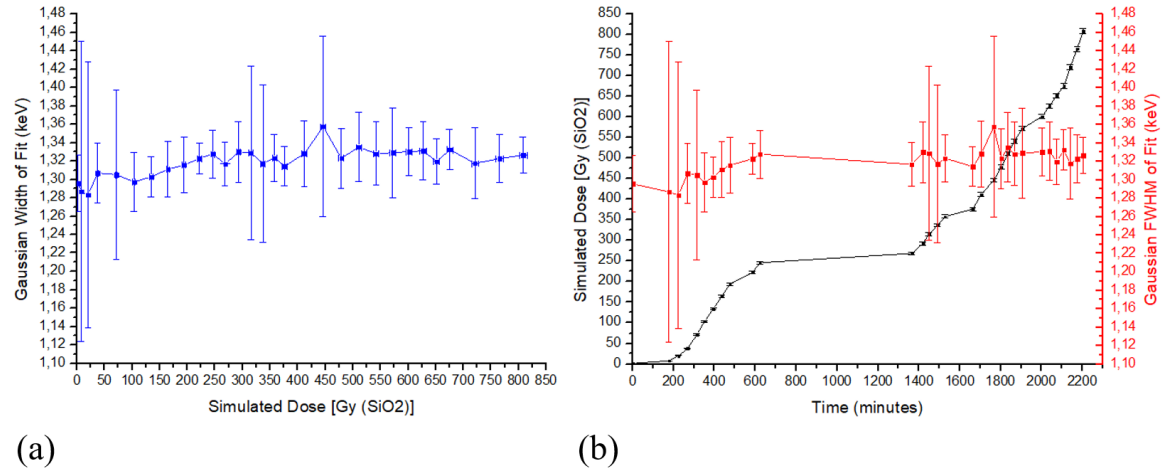

Figure 3.24: Evolution of the energy peak standard deviation, in threshold current units, with (a) dose in the oxide, and (b) time of the experiment, comparing to the time evolution of the dose. The line connecting the data points are only for better visualization of the evolution tendency of data, not corresponding to a curve fit.

Figure 3.24 exhibits the evolution of the Gaussian width with dose and time. The Gaussian width impact was not so evident. The calculated correlation coefficient is 0.675, and its oscillation does not overcome the fitting error. The dose impact in the spectrum has demonstrated to be not so significant at this range of dose.

3.3 High Dose Experiment

3.3.1 Impacts on Image - Position I

During the first position of the high dose experiment, the detector was exposed to 40 dose steps, varying the dose rate and reaching 6178 ± 29 Gy. Figure 3.25(a) exhibits an image obtained with the monochromatic beam at this position for the first dose step, before any polychromatic beam irradiation; Figure 3.25(b) exhibits an image of the same pixel area after the last dose step, for visual comparison.

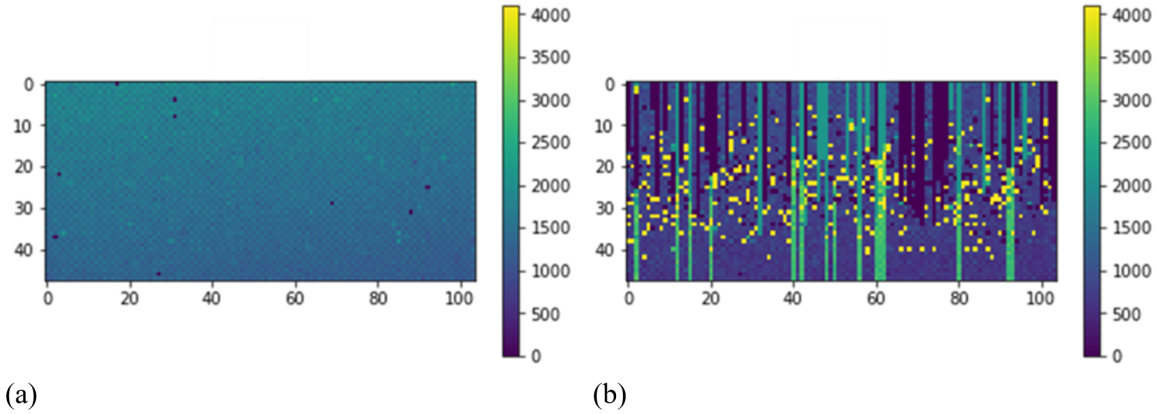

Figure 3.25: Image of the selected area for irradiation, ((a) before the exposure (dose 0) and (b) in the last step of irradiation.

Structural Noise Parameter Evaluation

The method of adjusting the relative noise curve to equation (2.3.1), in order to quantify the contributions of quantum, electronic and structural noise, has already proven to be tricky at the low dose rate; in the high dose data processing it was discarded. Effects similar to the illustrated in Figure 3.13 were observed in the first dose steps and became more discontinuous with the dose increase, not being viable to find a good fit. The asymptotic method for obtaining the structural noise parameter k_s was applied, and the approximation of it's asymptotic value to the structural noise parameter k_s was considered. It is important to emphasize that only healthy pixels were considered for this evaluation, since it refers to more subtle effects.

Similar to the low dose experiment, the impact of the intensity oscillation with the ring current on the noise measurement was evaluated. Figure 3.26 shows the noise-to-average rate evolution with deposited dose at the oxide layers, divided in color groups according to the

injection shift. The increase of intensity provided by the re-injection did not provoke an increase on the relative noise value, discarding the possibility that it would be responsible for the asymptotic region of the curve. On the contrary, it presented a decrease after re-injection, more likely to be related to a time recovery effect during the injection break of 15 minutes.

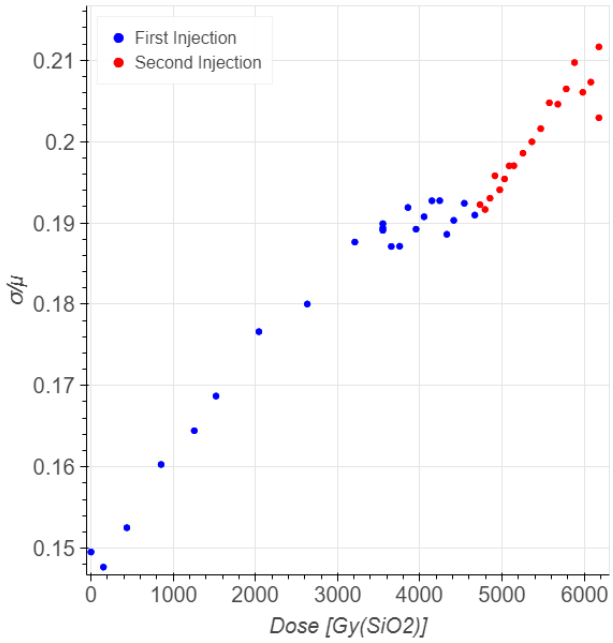

Figure 3.26: Evolution of the structural noise parameter k_s obtained from $\frac{\sigma}{\mu}$ for 2 seconds of acquisition with the dose step, color coded according to the injection beam shift. The increase of intensity provided by the re-injection did not provoke an increase on the relative noise value, discarding the possibility that it would leave the asymptotic region of the curve.

The evolution of this parameter with dose and time was analyzed, in order to consider possible time recovery effects. The results are presented in Figure 3.27. The dose rate effect is observable in these graphs: the k_s parameter grows faster from 0 to 300 minutes of experiment, when the dose rate was higher. The correlation coefficient calculated between the noise parameter and the dose was 0.979.

As in the previous experiment, a measurement of the Euclidean distance related to the undamaged image was obtained for comparison. Figure 3.28 presents its evolution with the experiment timeline, in comparison with the dose temporal evolution. Different than the structural noise parameter, this quantity increased faster after 800 minutes, or 4732 ± 28 Gy.

As in the low dose experiment data processing, the correlation coefficient between the Euclidean distance and the deposited dose is smaller than the k_s metric: 0.735. This corroborates the better performance of the structural noise metric for the analysis.

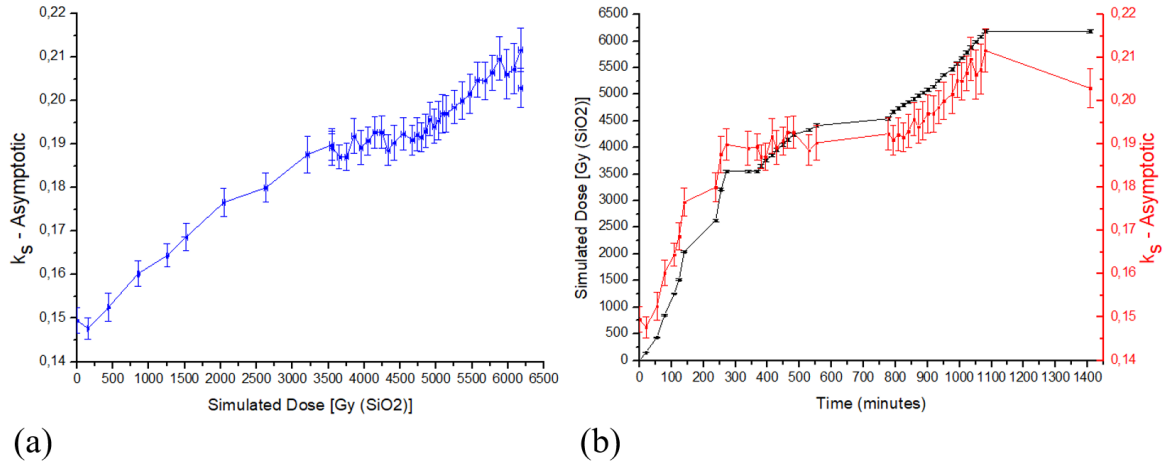

Figure 3.27: Evolution of the structural noise parameter k_s obtained from $\frac{\sigma}{\mu}$ for 2 seconds of acquisition with (a) the deposited dose on the oxide, and (b) with the experiment duration time, in comparison with the time evolution of the dose. A strong correlation can be verified. The line connecting the data points are only for better visualization of the evolution tendency of data, not corresponding to a curve fit.

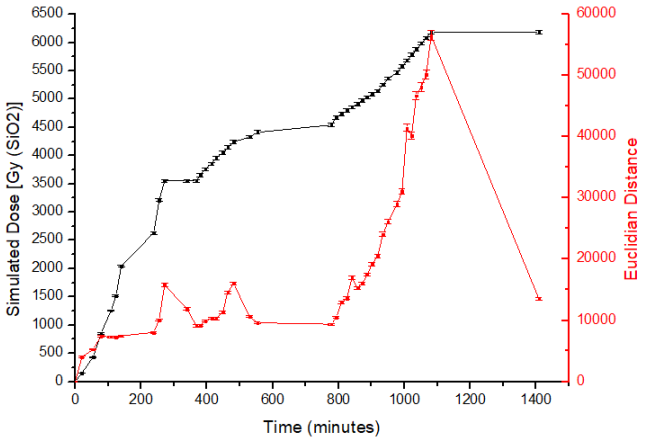

Figure 3.28: Euclidean distance between the characterization images and the "dose 0" image, for the same acquisition time of 2 seconds per frame. The line connecting the data points are only for better visualization of the evolution tendency of data, not corresponding to a curve fit.

Pixel Statistics Evaluation

Other image effects were observed in this experiment, as evidenced in Figure 3.25(b): the increasing number of hot pixels (pixels with counts saturated at 4095, the equivalent to 12 bits in high state); dead pixels (counting 0); and pixels counting intermediate values higher than the average count number, distributed in columns. The histograms of pixel counting values and their evolution with the dose step were evaluated. Figure 3.29 exhibits these histograms, evidencing five distinguishable groups of pixels: G1 - Dead pixels; G2 - Healthy pixels; G3 -

Pixels counting 2159; G4 - Gaussian distributed pixels with higher than expected count value; and G5 - hot pixels. This division eases the analysis of each effect evolution with dose separately.

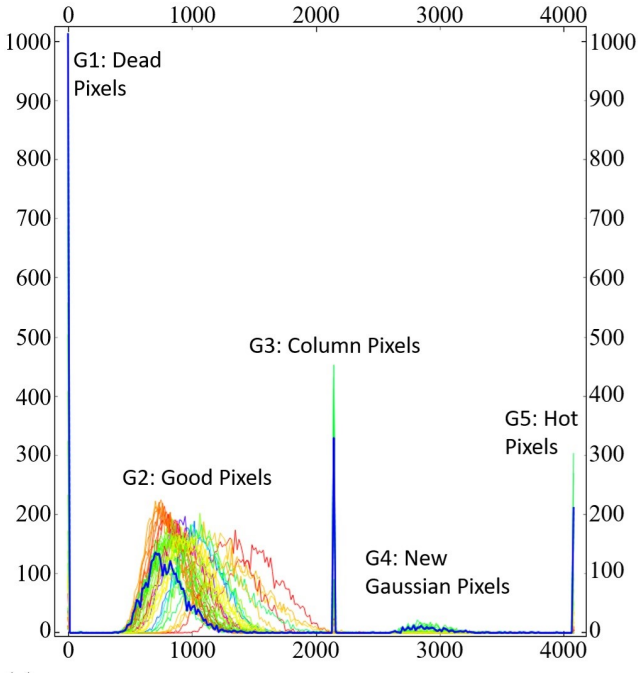

Figure 3.29: Histograms of the irradiated pixels for each dose step evaluated, specifying the division of the pixels in five groups, according to their behaviour. The line connecting the data points are only for better visualization of the evolution tendency of data, not corresponding to a curve fit.

The percentage of pixels from each group was evaluated in the experiment timeline, and compared to the dose evolution. A significant decrease of the healthy pixels percentage starting at 800 minutes of experiment or 4732 ± 28 Gy is observed, in oppose to the increase of all the other groups percentages. The recovery effect is also evident when observing the G2 percentage for the last measurement, after 300 minutes without irradiation. Figure 3.30 shows the evolution of all the groups percentages along the experiment; Figure 3.31 exhibits the comparison between the decay of healthy pixels percentage and the recovery time before each step, to evidence recovery effects.

Dead and hot pixels were expected phenomena, since their occurrence was also reported in other kinds of pixel detectors [45, 69, 79, 80]. They refer to shifts on the analogical DC level of the pulse, previous to the discriminator; a higher background would elevate the electronic noise, provoking an excess of counts (hot pixels); a lower background would decrease the photon current peak in relation to the threshold current, restraining it to be counted.

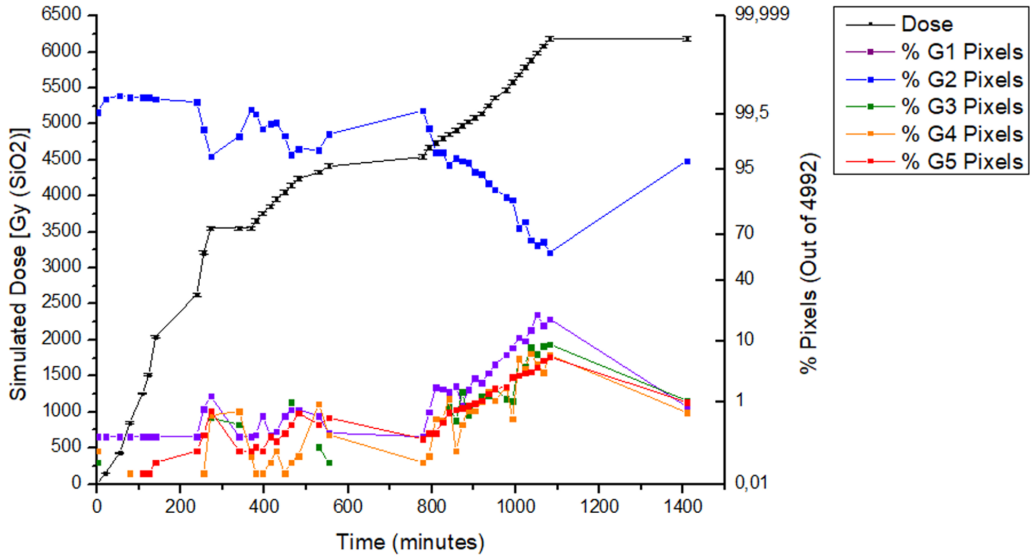

Figure 3.30: Percentage of irradiated pixels belonging to each of the 5 groups as a function of the experiment time, in comparison with the dose temporal evolution.

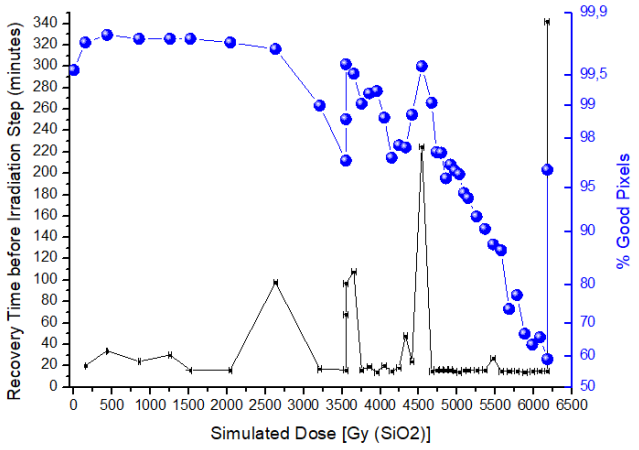

Figure 3.31: Percentage of the healthy pixels (G2) as a function of dose, comparing to the recovery time before each measurement.

The column effect presented by pixel groups G3 and G4 is related to the ASICs architecture: the digital electronics of each pixel, made of shift-register circuits, are connected to its vertical neighbours, to enable the chip cascading readout top to bottom [16]. This provokes the extension of the irradiated pixels damages to the sequential pixels, which can be verified when observing the entire image (Figure 3.32).

The observed cascading effect regarding groups G3 and G4 are transient and correspond to soft errors [39]: they can be inferred to affect only the column connected part of the digital electronics of the pixels, composed of the shift register counters, as expected.

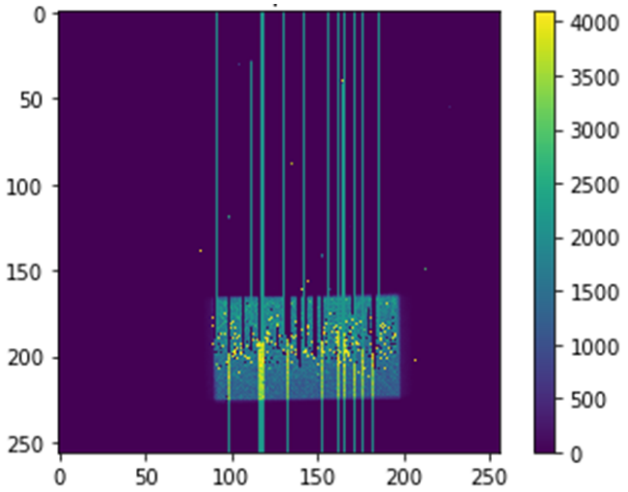

Figure 3.32: Image obtained from the Medipix3RX detector for an intermediate dose step (5882±29 Gy), evidencing the column behaviour of pixels from groups G3 and G4.

Another evidence that effects G3 and G4 happen on the shift-register level is the photon counting value. The shift-register digital circuits are designed as pseudo-random counters [16], which means that their value needs to be interpreted afterwards according to a look-up table for obtaining the correct number of counts. When all the bits of the pseudo-random counter are at the high state, the corresponding look-up table counting value is not 4095, but 2159, which is exactly the value presented by group G4 pixels.

Group G3 pixels distribution presented a Gaussian behaviour similar to group G2, shifted to higher counts. A more detailed analysis of Figure 3.32 suggests that all columns affected by G3 damages are the same as columns presenting G4 effect, but, different than G4 pixels, they are always in the lower part of the strongest irradiated area, considering the readout direction. The raised hypothesis is that these pixels counts are a result of summing the healthy G2 pixels counts to value 2159, which corresponds to the G4 column counts. Figure 3.33(a) shows the average counts of G2 pixels in comparison with the average counts of G3 pixels minus the 2159 G4 value, and their evolution with the ring current (a certain characteristic of the real photon counts). To most of the steps the two values can be considered statistically equivalent. Figure 3.33(b) exhibits the same average values in the experiment temporal evolution context, compared to the dose accumulation. These pixel distribution appeared only for dose steps above 4000 Gy, being composed by few pixels at the first appearances, which justifies the bad correspondence of the average values for the first results presented in Figure 3.33.

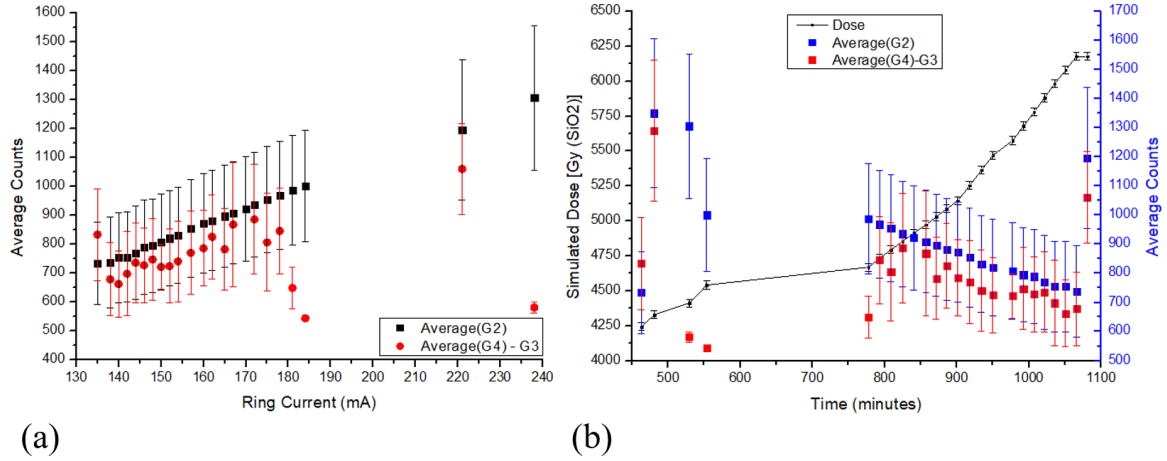

Figure 3.33: Comparison of the mean counts of healthy pixels (group G2) with the mean counts of G4 pixels minus the steady value of G3 pixels, (a) as a function of the ring current, and (b) it's temporal evolution. Their counting value is statistically equivalent.

By analyzing Figure 3.33 one can notice that, even if their difference are smaller than the measurement error, the values related to G3 pixels are always smaller than G2 values. This effect was attributed to the monochromatic beam profile (Figure 3.34): the average number of counts per row decreases in the vertical. Since G3 pixels are always on the lowest half of the beam, it justifies the average counts difference between the plots. For the first dose step measurement, and therefore before any damage, the total average of the pixels is 1530.2, whilst the average of the lower half pixels is 1394.6, a difference closer to the observed in Figure 3.33.

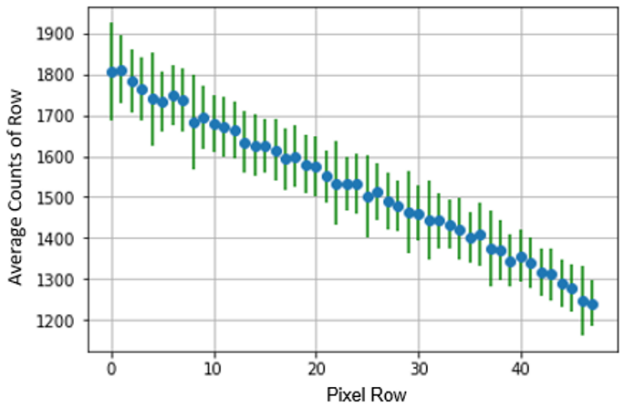

Figure 3.34: IMX monochromatic beam intensity profile, evidencing a vertical decrease in the detector readout direction.

Similar to the counter failures, it can be deduced that effects related to group G5 affect only the electronics previous to the counters: the radiation effects on the electronics provoke positive

charges trapped in the oxide, keeping the transistors in an always-conducting state, regardless the input voltage. They are interpreted as real counts, saturating the physical binary limit of the counters: 4095 corresponds to the maximum number of counts (12 bits full).

Group G1 pixels presented both behaviours: there are isolated dead pixels and, for higher dose values, also dead columns. It can be deduced that both the isolated and the connected digital circuits presented dead pixel effects, and therefore there are actually two distinct groups of pixels counting 0.

The isolated damage group effect should be similar to the G5 pixels damage, but directed to the other counting boundary: the number of interface traps overcomes the number of oxide charges, which provokes the need of a higher voltage than the provided for the transistors to conduct current, and these pixels count nothing. The interconnected damage group, otherwise, set all bits to the low state; different than the saturated bits case, the look-up table value for 0 counts is also 0.

The dead column effect is similar to already related failure behaviours in CCD detectors [69, 79, 80]. However, at these detectors, a real charge transfer happens between pixels during the readout, and the failure is described as "charge transfer traps": electrons from the pixels above are "trapped" in the damaged pixel, which cannot transfer charge any further [80]. At the hybrid-pixel detector case, only bits are transferred between pixels. A shift register failure is more likely; and similarly, the shift register from a specific pixel cannot transfer bits any further, cancelling all the bits of the previous pixels in the column hierarchy.

Recovery Evaluation

The evolution of the G5 number of pixels was followed through short and long time recovery for this experiment. A plot of this evolution with time is presented in Figure 3.35.

The G5 pixels recovery could be well fitted to an exponential function, resulting in a 0.998 χ-square value, and tending to a fixed asymptotic number of 5 to 6 hot pixels that seem to be unrecoverable. Once it fits an exponential behaviour, it was possible to obtain the curve's half-life value, in minutes (equation 3.3.1):

$$\tau_{\frac{1}{2}} = \frac{\ln 2}{R_0} = 110.4 \pm 1.3 \text{ minutes} \tag{3.3.1}$$

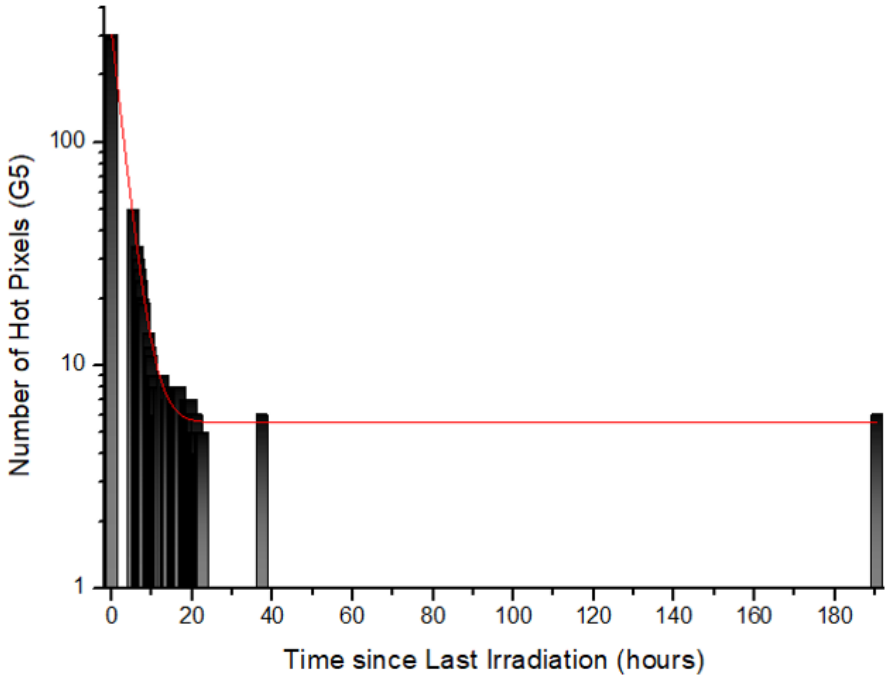

Figure 3.35: Evaluation of the number of G5 pixels in the irradiated area as a function of the recovery time, and it's exponential fit.

3.3.2 Impacts on Image - Position II

The detector was moved so the beam would hit a different, non-irradiated pixel area in the beginning of a new high dose experiment. 51 dose steps were measured at the second position of the beam, reaching a total of 6228 ± 19 Gy. The dose rate variation at this experiment was smaller, maintaining an average of 125±20 Gy per step, or 5.84±0.07 Gy per minute, so the dose rate effect could be analyzed separately. Figure 3.36(a) exhibits an image obtained with the monochromatic beam at this position for the first dose step, before any poly-chromatic beam irradiation; Figure 3.36(b) exhibits an image of the same pixel area after the last dose step, for visual comparison.

Structural Noise Parameter Evaluation

Similar to the previous experiment, the asymptotic method for obtaining the structural noise parameter k_s was applied. Only healthy pixels were considered for this evaluation.

The impact of the intensity oscillation with the ring current on the noise measurement was evaluated for this experiment as well. Figure 3.37 shows the noise-to-average rate evolution with deposited dose at the oxide layers, divided in color groups according to the injection shift.

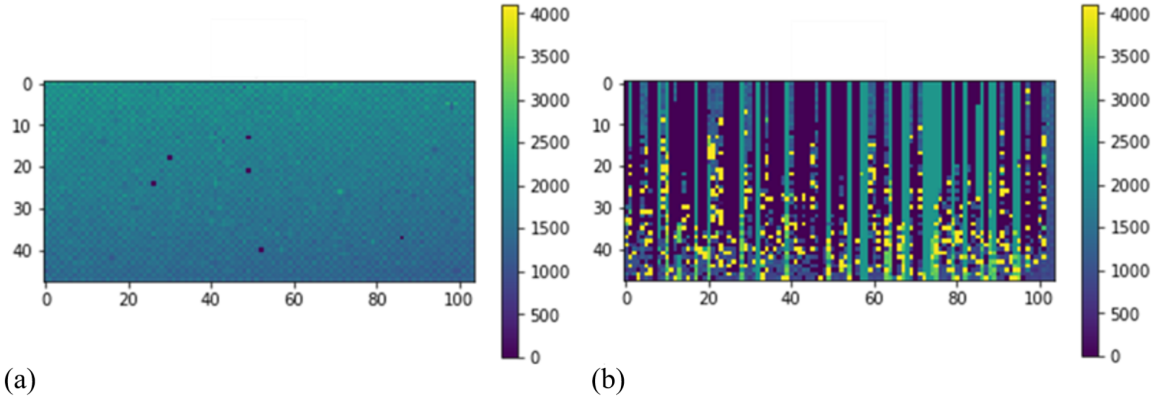

Figure 3.36: Image of the selected area for irradiation, (a) before the exposure (dose 0) and (b) in the last step of irradiation.

A decrease of the relative noise value was also observed at this position, which is consistent to the result for the first position, corroborating the hypothesis of a time recovery effect during the injection break.

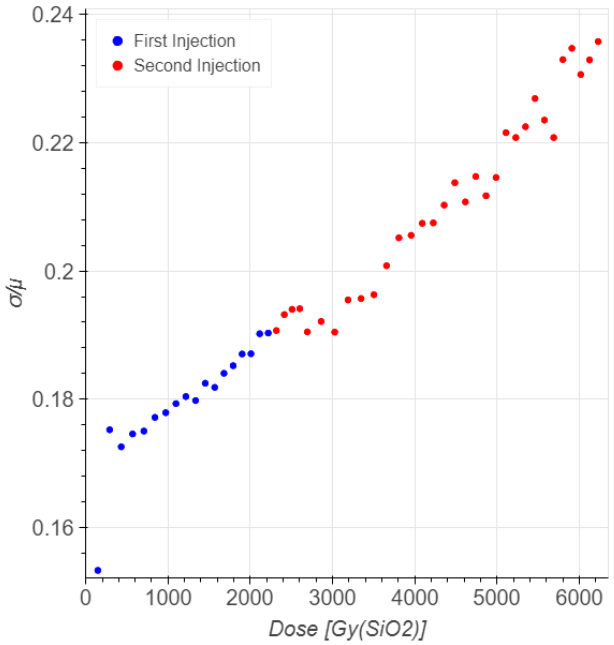

Figure 3.37: Evolution of the structural noise parameter k_s obtained from $\frac{\sigma}{\mu}$ for 2 seconds of acquisition with the dose step, color coded according to the injection beam shift. The increase of intensity provided by the re-injection did not provoke an increase on the relative noise value, discarding the possibility that it would leave the asymptotic region of the curve.

The evolution of this parameter with dose and time was analyzed. The results are presented in Figure 3.38. This experiment present neither dose rate nor recovery effects, maintaining a considerably linear growth with dose: The χ-square of a linear fit resulted 0.9796, calculating

a slope of 0.04258. The correlation coefficient calculated between the k_s noise parameter and the dose was 0.984.

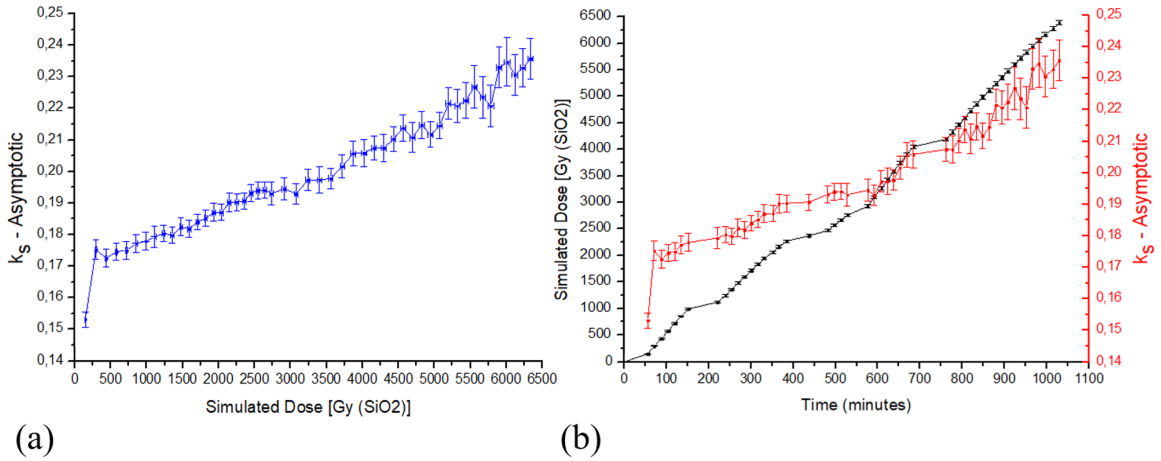

Figure 3.38: Evolution of the structural noise parameter k_s obtained from $\frac{\sigma}{\mu}$ for 2 seconds of acquisition with (a) the deposited dose on the oxide, and (b) with the experiment duration time, in comparison with the time evolution of the dose. A strong correlation can be verified. The line connecting the data points are only for better visualization of the evolution tendency of data, not corresponding to a curve fit.

A measurement of the Euclidean distance related to the undamaged image was obtained for comparison. Figure 3.39 presents its evolution along the experiment timeline, in comparison with the dose temporal evolution. Different than the structural noise parameter, this metric increased faster after 600 minutes of experiment, or 3200 Gy, and presented greater recovery signals between 700 and 800 minutes.

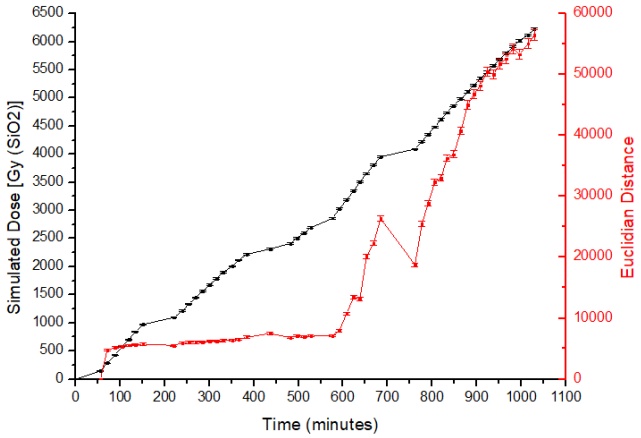

Figure 3.39: Euclidean distance between the characterization images and the "dose 0" image, for the same acquisition time of 2 seconds per frame. The line connecting the data points are only for better visualization of the evolution tendency of data, not corresponding to a curve fit.

The correlation coefficient between the Euclidean distance and the deposited dose was 0.9255, being higher than the calculated for the previous experiments. However, the k_s metric remained presenting a better correlation, which indicates its better performance on this analysis.

Pixel Statistics Evaluation

The histograms of pixel counting values and their evolution with the dose step were evaluated. Figure 3.40 exhibits these histograms, evidencing the same five groups of pixels for this experiment: G1 - Dead pixels; G2 - Healthy pixels; G3 - Pixels counting 2159; G4 - Gaussian distributed pixels with higher than expected count value; and G5 - hot pixels.

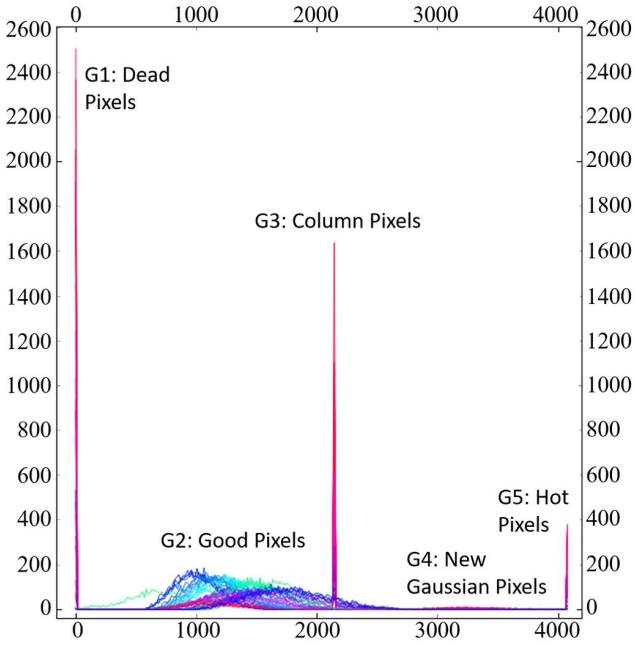

Figure 3.40: Histograms of the irradiated pixels for each dose step evaluated, specifying the division of the pixels in five groups, according to their behaviour.

The percentage of pixels from each group was evaluated in the experiment timeline, and compared to the dose evolution. A decrease of the healthy pixels (G2) percentage can be observed, in oppose to the increase of all the other groups percentages, starting at 528 minutes of experiment or 2600 ± 12 Gy. Figure 3.41 exhibits all the groups percentage evolution with time, and Figure 3.42 exhibits the comparison between the decay of healthy pixels percentage and the recovery time before each step, to point out possible recovery effects.

The same damage behaviours were observed in the two high dose experiment positions,

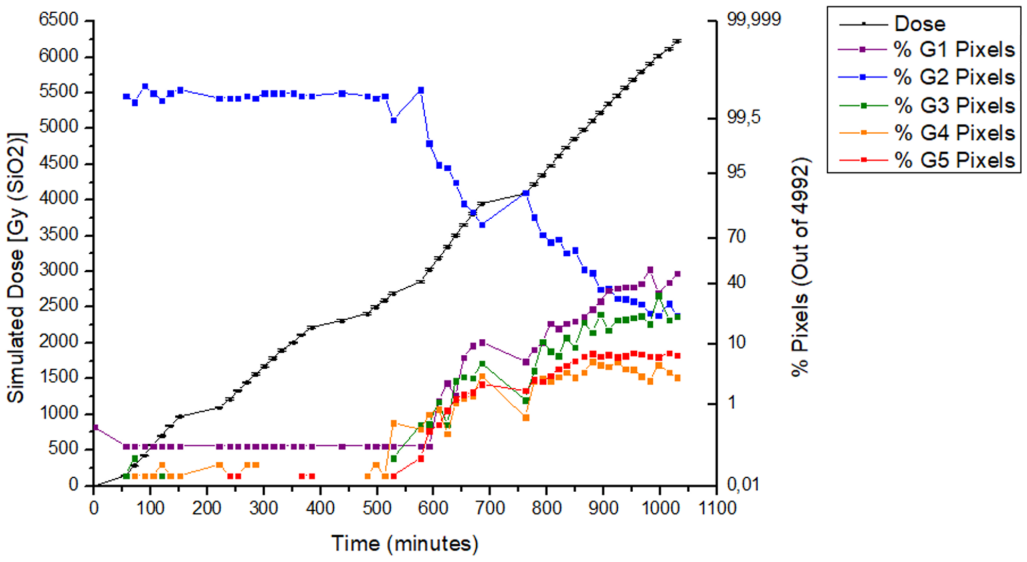

Figure 3.41: Percentage of irradiated pixels belonging to each of the 5 groups as a function of the experiment time, in comparison with the dose temporal evolution. The line connecting the data points are only for better visualization of the evolution tendency of data, not corresponding to a curve fit.

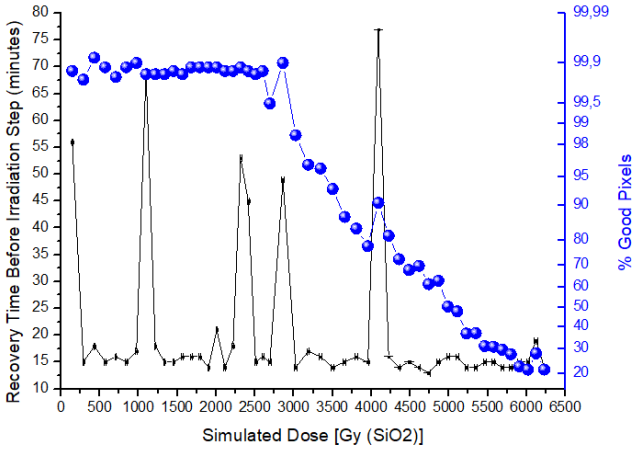

Figure 3.42: Percentage of the healthy pixels (G2) as a function of dose, comparing to the recovery time before each measurement.

like illustrated by Figures 3.52 and 3.32. The hypothesis that G3 pixels counts are a result of summing the healthy G2 pixels counts to the G4 column counts fixed at 2159 was evaluated. Figure 3.44 exhibits plots of the average counts of G2 pixels in comparison with the average counts of G4 pixels, discounting the G4 value (=2159), and their evolution with the ring current. To most of the steps, the two groups average values can be considered statistically equivalent.

The damage effects interpretation and the hypothesis for the locations of their origins for the first position are corroborated by the second experiment.

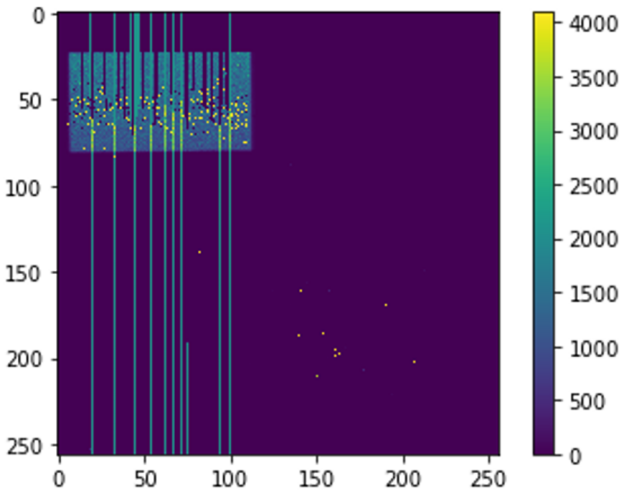

Figure 3.43: Image obtained from the Medipix3RX detector for an intermediate dose step (4485±17 Gy), evidencing the column behaviour of pixels from groups G3 and G4.

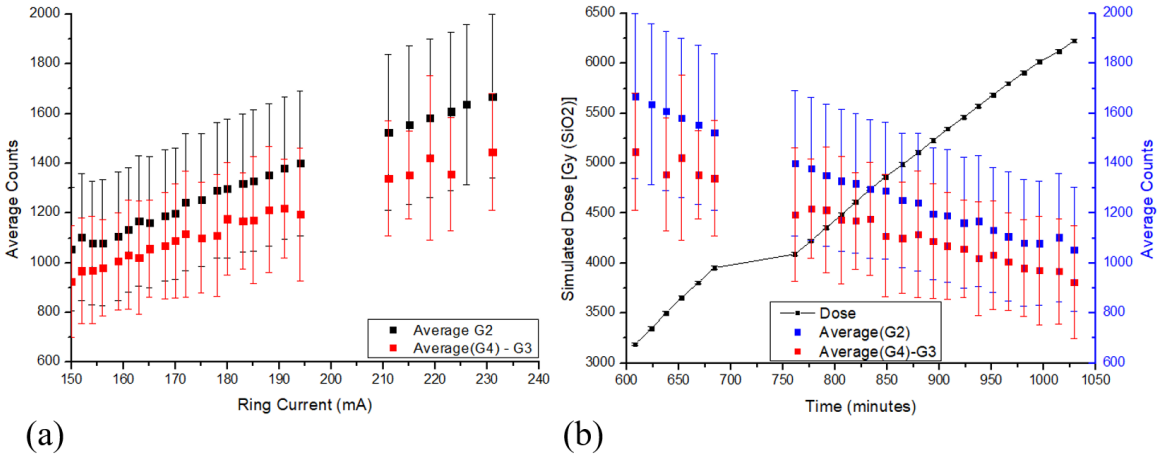

Figure 3.44: Comparison of the mean counts of healthy pixels (group G2) with the mean counts of G4 pixels minus the steady value of G3 pixels, (a) as a function of the ring current, and (b) it's temporal evolution. Their counting values are statistically equivalent.

3.4 Comparison and Discussion

Figure 3.45 exhibits an image of the whole detector field-of-view obtained with a Siemens K710-H X-ray generator of circular output one day after the high dose experiments. The polychromatic synchrotron beam irradiated areas can be clearly distinguished by the rectangular blocks of pixels presenting higher noise (for a better comparison see Figures 3.21, 3.32 and 3.52). The low dose experiment region (pixel rows 85 to 140) seems almost totally recovered, with a much less visible noise than the other irradiated regions. The last irradiated position (pixel rows 30 to 85) still presents G1 column effects, but not G4 column effects, corroborating

the hypothesis that the G1 column effect is a more permanent damage and cannot be classified as a soft error.

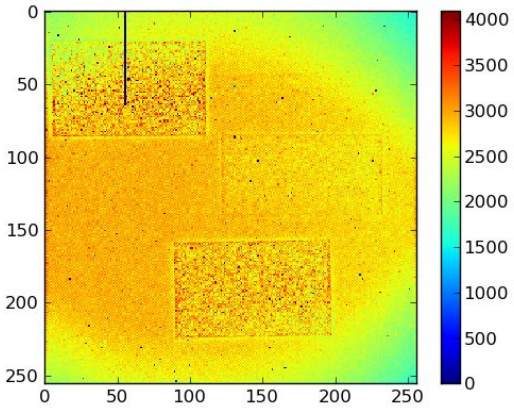

Figure 3.45: Flatfield of the whole detector field-of-view obtained with an X-ray generator, highlighting the irradiated areas.

Figure 3.46 compares the k_s structural noise parameter evolution with dose for each experiment. The low dose plot and the beginning of the first position high dose plot are overlapped, demonstrating a reproducible behaviour of this parameter evolution with the deposited dose at the oxide layers, and also a total recovery of the detector from one experiment to the other. The second position plot is shifted towards higher k_s values for the same dose steps, possibly indicating an influence of the damage even in not irradiated pixels, since the recovery time between the two high dose experiments was very small. Apart from this shift, the growth of the two high-dose presented curves with dose are consistent: the results of linear fits of the plots provided slopes of $(1.043 \pm 0.002) \times 10^{-5}$ for the first position and $(0.924 \pm 0.002) \times 10^{-5}$ for the second position.

The Euclidean distance measurement for the three experiments was also compared, as illustrated in Figure 3.47. Different than the k_s parameter, the two high dose curves are similar at the beginning; both distances start to grow around 3000 Gy. However, their behaviour differences after 3500 Gy present a clear effect of the recovery steps. The first experiment had two considerable recovery breaks, one of them exactly in the 3500 Gy region, decreasing it's Euclidean distance. Even though, both curves reach the same distance value at the last irradiation step, demonstrating an effect of the dose rate difference. The first position recovery gap after that is presented by a decrease of the Euclidean distance, almost to an initial value.

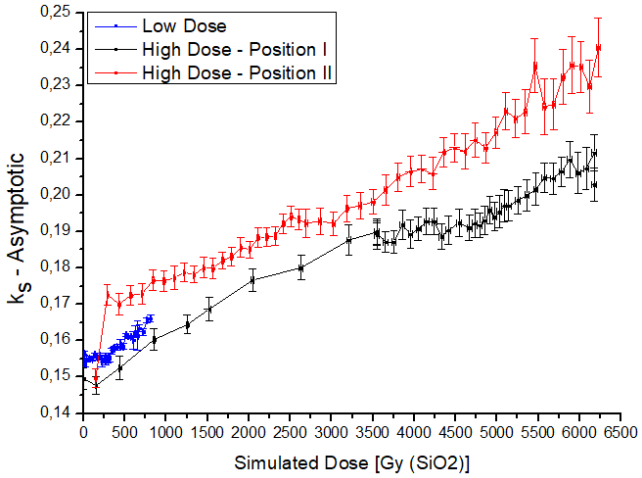

Figure 3.46: Structural noise parameter k_s obtained for the three experiments, for each step, for comparison. The line connecting the data points are only for better visualization of the evolution tendency of data, not corresponding to a curve fit.

The low dose measurement of the Euclidean distance is smaller than both high dose plots for the same dose steps, also indicating a dose rate impact.

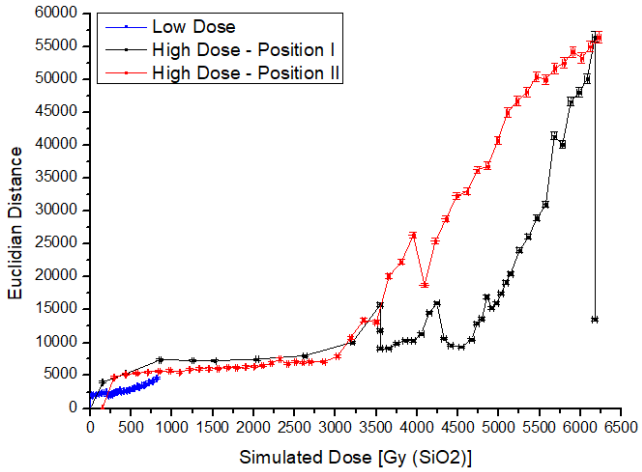

Figure 3.47: Euclidean distance curves calculated for the three experiments, for each step, for comparison. The line connecting the data points are only for better visualization of the evolution tendency of data, not corresponding to a curve fit.

The recovery breaks impact is illustrated in Figure 3.48, in which the percentage of healthy G2 pixels for the two high dose experiments are compared with the break time before each dose step. Higher recovery breaks happened along the first position experiment, and were followed by instant increases on the healthy pixels percentage. This contributed to the higher percentage of good pixels at the final step of this experiment, in comparison with the second position.

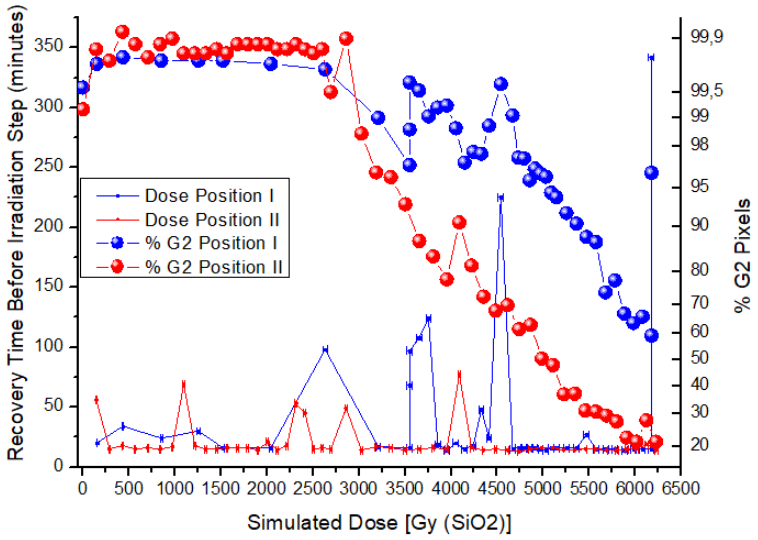

Figure 3.48: Number of healthy pixels (G2) for the two high dose experiments, as a function of the deposited dose in the oxide layers, and comparison with the recovery times before each irradiation step.

The G2 pixels contribution and the Euclidean distance quantity presented a similar behaviour, regarding the differences between the two high dose experiments.

A further evaluation is the measurement of the dead time evolution of the irradiated pixels with the deposited dose. Two measurements of the mono beam in the same condition were made for each step with different filtration, resulting in averages of 8×10^2 and 4×10^3 photons/second/pixel, so an estimation of the slope of the dead time curve could be obtained. Figure 3.49 exhibits the slope of the pixels average for the two filtration setups, compared to the dose 0 measured fluences.

It has been reported that the Medipix3RX limit for 10% piled-up photons is for input fluxes around 10^5 photons/second/pixel [73]. The measured fluences at these experiments are far from this limit, which means that only hard variations on the dead time could be detected. The data presented in Figure 3.49 corroborates this hypothesis, showing greater impact on the slope for the high dose experiments (above 4000 Gy). It also demonstrates the recovery influence of time breaks, presenting spikes matching the percentage of G2 pixels evolution (Figure 3.48) and the Euclidean distance curves (Figure 3.47). Further experiments should be made of this metric, measuring the fluence for several filtration setups between the dose steps, for a more precise evaluation of the dose impact on the dead time curve.

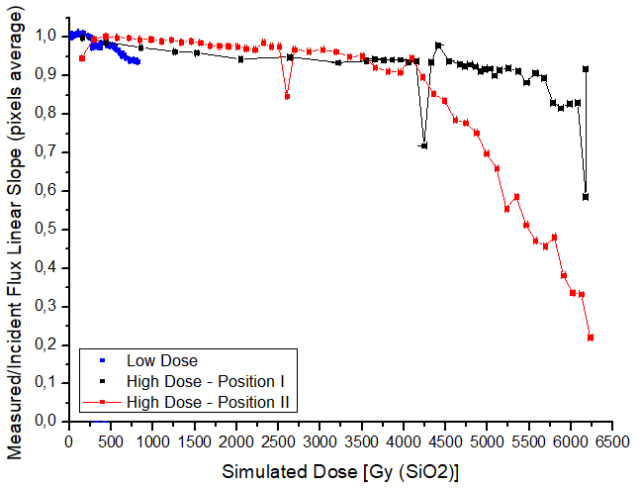

Figure 3.49: Linear slope between measurements of the mono beam for two different filtration setups, measured related to the initial slope for the zero dose fluences. The line connecting the data points are only for better visualization of the evolution tendency of data, not corresponding to a curve fit.

Recovery Evaluation

A comparison of the analogical effects G1 and G5 and their temporal evolution for the two high dose experiments is presented in Figure 3.50. Even if reaching different permanent pixel numbers, the four groups of damaged pixels seems to recover in a similar way, presenting an exponential decay. Only the measurements of G5 pixels on first position were considered for the exponential fit, since several measurements were obtained for this group.

The k_s parameter recovery was also analyzed for both positions. In this case, not enough recovery data was taken for fitting the recovery dependency, as can be concluded from Figure 3.51. One can infer, though, that a plateau was probably reached for both positions before a 40 hours rest since the last irradiation. Though with a huge associated error due to lack of data, the curve's half-life time results in around 9.5 hours, or 570 minutes. This effect shows slower recovery then effects presented in Figure 3.50. It is necessary to take into account that the recovery data was obtained from irradiating the detector with the X-ray generator source, which has a different intensity distribution compared to the beamline source, therefore impacting the noise parameter as a new background. This points out a limitation of this quantity: the beam intensity distribution dependence turns it into a relative measurement.

A new equalization matrix would be expected to decrease the radiation-acquired structural noise, improving the image signal-to-noise ratio [16, 32, 36]. A procedure for fine tuning

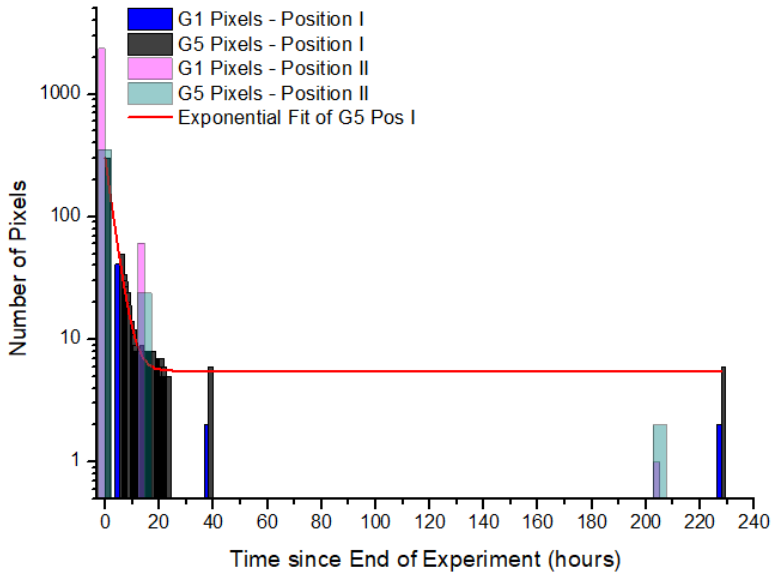

Figure 3.50: Number of G1 and G5 pixels as a function of the recovery time, for the two high dose experiments.

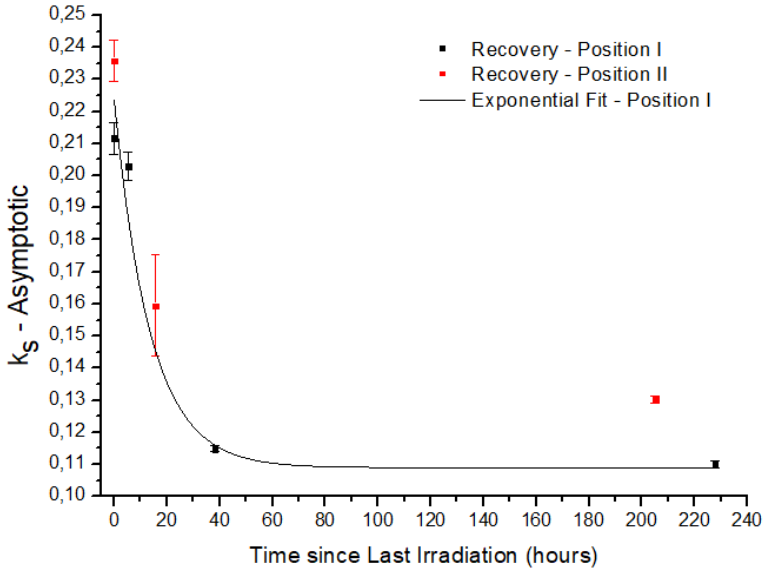

Figure 3.51: Structural noise parameter k_s evolution with the recovery time.

the threshold levels of the pixels was performed before the experiments and remade after, generating a new equalization matrix, according to the method described by Rinkel *et al.* [35]. Noise parameters were compared for images with each matrix. Figure 3.52 exhibits a map of the absolute difference of the two matrix values calculated for each pixel; the irradiated areas presented a higher difference. Table 3.1 contains experimentally obtained k_s parameters with each equalization matrix, illuminating the detector with an X-ray generator source.

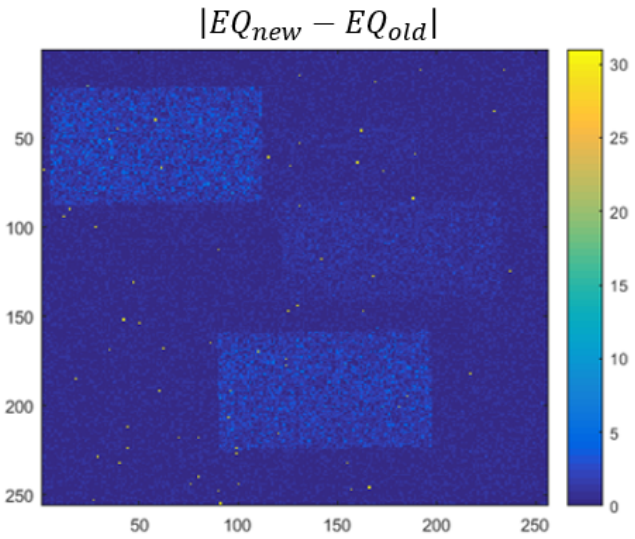

Figure 3.52: Absolute difference between the obtained pixel adjustment bit values from the generated matrix before the irradiation experiment, and for a new generated matrix after the experiment. The irradiated regions present bigger pixel adjustment differences than the preserved pixels.

Table 3.1: Structural noise Parameter Variation with Equalization

	Old Equalization	New Equalization
Low Dose Experiment	0.068±0.001	0.069±0.001
High Dose - Position I	0.103±0.002	0.094±0.004
High Dose - Position II	0.160±0.003	0.151±0.002

It can be observed from table 3.1 that the low-dose irradiated region presented no evolution with the new equalization from the structural noise point of view. Figure 3.52 also illustrates that the pixels from this region are almost unnoticed in comparison with the preserved pixels. The high dose regions were slightly benefited from the new equalization, decreasing its k_s noise parameter value.

The new equalization has also improved the global detector energy resolution. Energy spectra were obtained with the test pulse simulated charge, and the peak width was obtained through the standard deviation value calculated by a Gaussian fit. It initiated in 594±2 eV before the experiment and with the first equalization, increased to 611±3 eV after the irradiation experiment and maintaining the previous equalization, and has now decreased to 574±2 eV. This result corroborates the hypothesis that a periodical update on the equalization is needed, choosing the period according to the irradiation dose rate of the application [35].

Application of the Results

A limit for keeping the k_s parameter constant was observed in the low dose data analysis. The k_s value was kept stable within the error limits until 337 ± 4 Gy.

Based on both high dose experiments, radiation limits could also be estimated. Table 3.2 compares the established limits from each experiment: the radiation dose threshold before visual damage and the threshold for a healthy pixel percentage of 90% were detected.

Table 3.2: Damage limits

	Position I	Position II
Dose Threshold for avoiding damage	2631±23 Gy	2600±12 Gy
Dose Threshold for 90% G2	5364±30 Gy	3585±19 Gy

Although the obtained dose limit for avoiding any damage are relatively similar for the two experiments, a high difference can be noticed between the dose threshold for less 10% pixels loss, where the value was higher for the deposited dose value at position I. This can be related to the recovery gaps along the experiment: the first experiment included time intervals between irradiation steps higher than the calculated half-life value for the G5 pixels (equation 3.3.1). Extrapolating this recovery time for the full recovery of the chip electronics, it can be inferred that the detector recovered to a state related to a 50% smaller deposited dose. This consideration would decrease the limit dose for 10% pixels loss to 3907±43 Gy, closer to the 3585±19 Gy obtained for position II than the previous value. The reminiscent difference between the values can be attributed to a dose rate effect.

Table 3.3 illustrates the dose rate expected for some of the Medipix3RX applications, for comparison with the obtained dose limits. The expected deposited dose at the oxide layers was obtained via simulation Monte Carlo, considering the energy used for each application.

The first four rows presents the expected behaviours of some of the planned Sirius beamlines. Carnaúba will be a nanofocus beamline for ptycography imaging, mainly focused on biological samples. It will be operated in a tender X-ray energy range, avoiding sample damage. Cateretê will be dedicated to Coherent Diffraction Imaging and X-ray Photo-correlation Spectroscopy techniques, based on microscopic beam sizes. Manacá will be fully dedicated to macromolecular crystallography, based on single-crystal X-ray diffraction. Ema will be a higher energy beamline applied for *in situ* analysis of samples under extreme conditions of temperature and pressure,

time-resolving characterizations that specially require a fast detector readout [81]. The fifth row presents the dose rate expected for mammography diagnosis, an usual medical application requiring a large detector area.

A direct beam irradiating one pixel area was simulated. The sensor thicknesses are suggested among the commercial options, according to the energy range, for better efficiency and lower radiation damage to electronics. Most of the applications will not implicate direct irradiation, but a result of this radiation interaction with the sample. Thus, the presented dose is an overestimation. However, each specific application can be based on a fraction of this value.

Table 3.3: Expected Dose Rate for different Medipix3RX Applications.

Application	Sensor	Main Energy (keV)	Flux (ph/s.pixel)	Dose Rate (Gy/s)
Carnaúba	Si 300 μm	15	1×10^{12}	$(3.2 \pm 0.3) \times 10^{5}$
Cateretê	Si 300 μm	9	1×10^{13}	$(2.68 \pm 0.06) \times 10^{5}$
Manacá	Si 300 μm	12.6	1×10^{12}	$(2.22 \pm 0.04) \times 10^{5}$
Ema	Si 675 μm	20	1×10^{12}	$(3.12 \pm 0.03) \times 10^{5}$
Mammography	Si 675 μm	20	1.4×10^{3}	$(3.84 \pm 0.2) \times 10^{-4}$

For the medical application, an estimation of the detector life cycle can be obtained. Comparing to the average dose value for visual damage obtained for both positions, the total time of use for the first signals of damage is expected to be 1890 ± 105 hours, without considering recovery effects. Further considerations on the expected dose rate are still required for a more accurate evaluation.

Chapter 4

Conclusions

The goal of understanding the dose physical effects on the detector and relating them quantitatively to the data damage was accomplished.

Once the dose effect on the image date is fully understood, it can be taken into consideration in Monte Carlo based simulation tools of pixelated imaging detectors, like the *tally Pixel Image Detector* from PENELOPE, based on the deposited dose on oxide layers. The inclusion of other detection artifacts like the charge reflection [82, 83] and the pulse pile-up in the pixel electronics [73] could also be considered for a complete modeling.

The charge-sharing effect simulation behaviour was verified and validated, correlating the experiment and the simulation and supporting the feasibility of using the deposited dose obtained via simulation as an estimation of the experimental dose value. The algorithm has proven to be adequate with the physical response of the sensor. It provides a more accurate approach for analyzing the detected data, and allows an estimation on this effect for different sensor thicknesses and other semiconductor materials. The code is open source and will be available for PENELOPE users around the world.

The implemented algorithm for the charge dispersion effect can be adapted, with a few modifications, for modeling the electron-hole pairs generation in the oxide layers and their recombination rate, which is also influenced by the applied electric field at the gates. Taking the recombination process into account would correspond to a better model of the radiation effect, reaching more accurate values for the deposited dose at these layers.

A comparison of the dose rate expected for several Medipix3RX applications with the established limits was presented. For further studies, an analysis of the dose impact on the detector

dead time can be made with more measurements. The radiation interaction with high-Z sensor materials like Cadmium telluride will require a similar analysis, specially for the high energy beamlines at Sirius.

The acquired knowledge could justify and define periodically maintenance procedures of the detectors. The work also points out the importance of developing a method for radiation protection to the ASIC layers in the near future.

References

1. Fornaini, A., Boerkamp, T., de Oliveira, R. & Visschers, J. L. A tiled array of hybrid pixel detectors for X-ray imaging. *IEEE Transactions on Nuclear Science* **51,** 1824–1828. ISSN: 0018-9499 (Aug. 2004).

2. Delpierre, P. A history of hybrid pixel detectors, from high energy physics to medical imaging. *Journal of Instrumentation* **9,** C05059 (2014).

3. Melzer, T. R. *et al.* Spectroscopic biomedical imaging with the Medipix2 detector. *Australasian Physics Engineering Sciences in Medicine* **31,** 300. ISSN: 1879-5447 (Dec. 2008).

4. Butler, A. *et al.* Bio-medical X-ray imaging with spectroscopic pixel detectors. *Nuclear Instruments and Methods in Physics Research Section A: Accelerators, Spectrometers, Detectors and Associated Equipment* **591.** Radiation Imaging Detectors 2007, 141–146. ISSN: 0168-9002 (2008).

5. Masetti, S., Roma, L., Rossi, P. L., Lanconelli, N. & Baldazzi, G. Preliminary results of a Multi-Energy CT system for small animals. *Journal of Instrumentation* **4,** P06011 (2009).

6. European Organization for Nuclear Research. *Medipix3 Collaboration* <`https://medipix.web.cern.ch/collaboration/medipix3-collaboration`>.

7. European Organization for Nuclear Research. *Medipix: From Particles to Patients* <`https://home.cern/about/updates/2012/01/medipix-particles-patients`>.

8. Pennicard, D. *et al.* in *11th International Conference on Synchrotron Radiation Instrumentation* (eds Susini, J. & Dumas, P.) (2013). doi:`10.1088/1742-6596/425/6/062010`.

9. Ponchut, C. *et al.* MAXIPIX, a fast readout photon-counting X-ray area detector for synchrotron applications. *Journal of Instrumentation* **6.** ISSN: 1748-0221. doi:`10.1088/1748-0221/6/01/c01069` (2011).

10. Jungmann, J. H. *et al.* Fast, High Resolution Mass Spectrometry Imaging Using a Medipix Pixelated Detector. *Journal of the American Society for Mass Spectrometry* **21,** 2023–2030. ISSN: 1044-0305 (2010).

11. Tartoni, N. *et al.* in *2012 Ieee Nuclear Science Symposium and Medical Imaging Conference Record* (ed Yu, B.) 530–533 (2012). ISBN: 978-1-4673-2030-6; 978-1-4673-2028-3.

12. Pinsky, L. S. *et al.* in *2012 Ieee Aerospace Conference* (2012). ISBN: 978-1-4577-0557-1.

13. Ballabriga, R. *et al.* The Medipix3RX: a high resolution, zero dead-time pixel detector readout chip allowing spectroscopic imaging. *Journal of Instrumentation* **8.** ISSN: 1748-0221. doi:10.1088/1748-0221/8/02/c02016 (2013).

14. Liu, L., Milas, N., Mukai, A. H. C., Resende, X. R. & de Sá, F. H. The Sirius project. *Journal of Synchrotron Radiation* **21,** 904–911 (Sept. 2014).

15. Faccio, F. & Cervelli, G. Radiation-induced edge effects in deep submicron CMOS transistors. *Ieee Transactions on Nuclear Science* **52,** 2413–2420. ISSN: 0018-9499 (2005).

16. Ballabriga, R. *The Design and Implementation in 0.13 μm CMOS of an Algorithm Permitting Spectroscopic Imaging with High Spatial Resolution for Hybrid Pixel Detectors* PhD thesis (Universitat Ramon Llull, 2009).

17. Porter, M. *et al.* Soft error reliability improvements for implantable medical devices. *2008 Ieee International Reliability Physics Symposium Proceedings - 46th Annual,* 488–+. ISSN: 1541-7026 (2008).

18. Zhang, J. *et al.* Investigation of X-ray induced radiation damage at the Si-SiO2 interface of silicon sensors for the European XFEL. *Journal of Instrumentation* **7.** ISSN: 1748-0221. doi:10.1088/1748-0221/7/12/c12012 (2012).

19. Knoll, G. *Radiation Detection and Measurement* ISBN: 9780470131480 (John Wiley Sons, 2010).

20. Salvat, F. *PENELOPE-2014: A Code System for Monte Carlo Simulation of Electron and Photon Transport* Book (NEA Data Bank, Barcelona, Spain, 2015).

21. Podgorsak, E. *Radiation Physics for Medical Physicists* ISBN: 9783319253824 (Springer International Publishing, 2016).

22. National Institute of Standards and Technology. *X-ray Mass Attenuation Coefficients: The Mass Attenuation Coefficient,* $\frac{\mu}{\rho}$ <https://physics.nist.gov/PhysRefData/XrayMassCoef/chap2.html>.

23. Medjoubi, K. *et al.* Detective quantum efficiency, modulation transfer function and energy resolution comparison between CdTe and silicon sensors bump-bonded to XPAD3S. *Journal of Synchrotron Radiation* **17,** 486–495 (July 2010).

24. Ashcroft, N. & Mermin, N. *Solid State Physics* ISBN: 9788131500521 (Cengage Learning, 2011).

25. Kittel, C. *Introduction to Solid State Physics* ISBN: 9780471415268 (Wiley, 2004).

26. Klein, C. A. Bandgap Dependence and Related Features of Radiation Ionization Energies in Semiconductors. *Journal of Applied Physics* **39,** 2029–+. ISSN: 0021-8979 (1968).

27. Claude, L. & Pier-giorgio, R. *Silicon Solid State Devices And Radiation Detection* ISBN: 9789814397384 (World Scientific Publishing Company, 2012).

28. Physics & Electronics, R. *Photodiode* <http://www.physics-and-radio-electronics.com/electronic-devices-and-circuits/semiconductor-diodes/>.

29. Nicollian, E. & Brews, J. *MOS (Metal Oxide Semiconductor) Physics and Technology* ISBN: 9780471430797 (Wiley, 2002).

30. Kuphaldt, T. R. *Insulated-gate Field-effect Transistors (MOSFET)* <https://www.allaboutcircuits.com/textbook/semiconductors/chpt-2/insulated-gate-field-effect-transistors-mosfet/>.

31. Fonstad, C. *Microelectronic devices and circuits* ISBN: 9780070214965 (McGraw-Hill, 1994).

32. Kraft, P. *et al.* Characterization and Calibration of PILATUS Detectors. *Ieee Transactions on Nuclear Science* **56,** 758–764. ISSN: 0018-9499 (2009).

33. Marchal, J. & Medjoubi, K. Detective quantum efficiency model of single-X-ray-photon counting hybrid pixel detectors. *Journal of Instrumentation* **7,** P11028 (2012).

34. University of Glasgow. *Medipix - High Energy Physics collaborators deliver technological breakthrough behind world's most advanced X-ray detector* <https://www.gla.ac.uk/schools/physics/research/researchimpact/headline_300603_en.html>.

35. Rinkel, J., Magalhaes, D., Wagner, F., Frojdh, E. & Sune, R. B. Equalization method for Medipix3RX. *Nuclear Instruments and Methods in Physics Research Section a-Accelerators Spectrometers Detectors and Associated Equipment* **801,** 1–6. ISSN: 0168-9002 (2015).

36. Pacciani, L. *et al.* Threshold equalization algorithm for the XAA1.2 ASICs and its application to SuperAGILE X-ray imager. *Nuclear Instruments and Methods in Physics Research Section A: Accelerators, Spectrometers, Detectors and Associated Equipment* **593,** 367–375. ISSN: 0168-9002 (2008).

37. Marinho, F. & Akiba, K. A GEANT4 based simulation for pixelated X-ray hybrid detectors. *Nuclear Instruments and Methods in Physics Research Section a-Accelerators Spectrometers Detectors and Associated Equipment* **772,** 50–51. ISSN: 0168-9002 (2015).

38. Nilsson, H. E., Dubaric, E., Hjelm, M. & Bertilsson, K. Simulation of photon and charge transport in X-ray imaging semiconductor sensors. *Nuclear Instruments and Methods in Physics Research Section a-Accelerators Spectrometers Detectors and Associated Equipment* **487,** 151–162. ISSN: 0168-9002 (2002).

39. Rathod, S. S., Saxena, A. K. & Dasgupta, S. Radiation Effects in MOS-based Devices and Circuits: A Review. *Iete Technical Review* **28,** 451–469. ISSN: 0256-4602 (2011).

40. Moll, M. *Radiation damage in silicon particle detectors: Microscopic defects and macroscopic properties* PhD thesis (Hamburg U., 1999). <`http://www-library.desy.de/cgi-bin/showprep.pl?desy-thesis99-040`>.

41. Oldham, T. R. & McLean, F. B. Total ionizing dose effects in MOS oxides and devices. *Ieee Transactions on Nuclear Science* **50,** 483–499. ISSN: 0018-9499 (2003).

42. Schwank, J. R. *et al.* Radiation Effects in MOS Oxides. *Ieee Transactions on Nuclear Science* **55,** 1833–1853. ISSN: 0018-9499 (2008).

43. Benedetto, J. M. & Boesch, H. E. The relationship between Co-60 and 10 keV X-ray damage in MOS devices. *Ieee Transactions on Nuclear Science* **33,** 1318–1323. ISSN: 0018-9499 (1986).

44. Re, V., Manghisoni, M., Ratti, L., Speziali, V. & Traversi, G. Total ionizing dose effects on the noise performances of a 0.13 mu m CMOS technology. *Ieee Transactions on Nuclear Science* **53,** 1599–1606. ISSN: 0018-9499 (2006).

45. Cester, A. & Paccagnella, A. Ionizing radiation effects on ultra-thin oxide MOS structures. *International Journal of High Speed Electronics and Systems* **14,** 563–574 (2004).

46. Frank, D. J. *et al.* Device scaling limits of Si MOSFETs and their application dependencies. *Proceedings of the Ieee* **89,** 259–288. ISSN: 0018-9219 (2001).

47. Roche, P., Gasiot, G., Forbes, K., O'Sullivan, V. & Ferlet, V. Comparisons of soft error rate for SRAMs in commercial SOI and bulk below the 130-nm technology node. *Ieee Transactions on Nuclear Science* **50,** 2046–2054. ISSN: 0018-9499 (2003).

48. Barnaby, H. J., Mclain, M. & Esqueda, I. S. Total-ionizing-dose effects on isolation oxides in modern CMOS technologies. *Nuclear Instruments and Methods in Physics Research Section B: Beam Interactions with Materials and Atoms* **261.** The Application of Accelerators in Research and Industry, 1142–1145. ISSN: 0168-583X (2007).

49. Prior, C. R. *The Physics of Accelerators (2004)* <`https://cas.web.cern.ch/sites/cas.web.cern.ch/files/lectures/baden-2004/physics-accelerators-2.pdf/`>.

50. Cezar, J. C. *et al.* The U11 PGM beam line at the Brazilian National Synchrotron Light Laboratory. *Journal of Physics: Conference Series* **425,** 072015 (2013).

51. Rinkel, J., Polli, J. M. & Miqueles, E. X. X-ray coherent diffraction imaging: Sequential inverse problems simulation. *Nuclear Instruments and Methods in Physics Research Section A: Accelerators, Spectrometers, Detectors and Associated Equipment.* ISSN: 0168-9002. doi:`https://doi.org/10.1016/j.nima.2017.10.032` (2017).

52. Brazilian Synchrotron Light Laboratory. *Accelerators: Operation and Reliability* <`http://www.lnls.cnpem.br/uvx-en/machine/`>.

53. Sayyar-Rodsari, B. *et al. Parametric modeling of electron beam loss in synchrotron light sources* in *IEEE Particle Accelerator Conference* (2007), 343–+. ISBN: 978-1-4244-0916-7.

54. Decking, W. *Introduction to Accelerator Physics (2009)* <`https://www-zeuthen.desy.de/students/2009/lectures/decking.pdf/`>.

55. Kunz, C. Synchrotron radiation: third generation sources. *Journal of Physics: Condensed Matter* **13,** 7499 (2001).

56. Tyagi, S. *et al. A 130 nm generation logic technology featuring 70nm transistors, dual Vt transistors and 6 layers of Cu interconnects* 567–570. ISBN: 0-7803-6439-2. doi:10.1109/iedm.2000.904383 (2000).

57. Alig, R. C., Bloom, S. & Struck, C. W. Electron-Hole-Pair Creation Energies in Semiconductors. *Bulletin of the American Physical Society* **25,** 175–175. ISSN: 0003-0503 (1980).

58. Kyprianou, L. S., Brackman, G., Myers, K. J., Badal, A. & Badano, A. in *Medical Imaging 2008: Physics of Medical Imaging, Pts 1-3* (eds Hsieh, J. & Samei, E.) (2008). ISBN: 978-0-8194-7097-3. doi:10.1117/12.772878.

59. Box, G. E. P. & Muller, M. E. A Note on the Generation of Random Normal Deviates. *Annals of Mathematical Statistics* **29,** 610–611. ISSN: 0003-4851 (1958).

60. Gimenez, E. N. *et al.* Medipix3RX: Characterizing the Medipix3 Redesign With Synchrotron Radiation. *IEEE Transactions on Nuclear Science* **62,** 1413–1421. ISSN: 0018-9499 (June 2015).

61. Del Rio, M. S. & Dejus, R. J. *XOP: A multiplatform graphical user interface for synchrotron radiation spectral and optics calculations* (eds Takacs, P. Z. & Tonnessen, T. W.) ISBN: 0-8194-2574-5. doi:10.1117/12.295554 (1997).

62. Henke, B. L., Gullikson, E. M. & Davis, J. C. X-Ray Interactions - Photoabsorption, Scattering, Transmission, and Reflection at E=50-30,000 EV, Z=1-92. *Atomic Data and Nuclear Data Tables* **54,** 181–342. ISSN: 0092-640X (1993).

63. Archilla, N. & Schubert, G. *Brazilian Synchrotron IMX Beamline* Private Communication. 2017.

64. Attix, F. *Introduction to Radiological Physics and Radiation Dosimetry* ISBN: 9783527617142 (Wiley, 2008).

65. Atkinson, K. E. *An Introduction to Numerical Analysis, 2nd ed.* ISBN: 978-0-471-50023-0 (John Wiley Sons, New York, 1989).

66. Evans, D. S., Workman, A. & Payne, M. A comparison of the imaging properties of CCD-based devices used for small field digital mammography. *Physics in Medicine and Biology* **47,** 117–135. ISSN: 0031-9155 (2002).

67. Jones, E., Oliphant, T., Peterson, P., *et al. SciPy: Open source scientific tools for Python* [Online; accessed <today>]. 2001–. <http://www.scipy.org/>.

68. Wang, L. W., Zhang, Y. & Feng, J. F. On the Euclidean distance of images. *Ieee Transactions on Pattern Analysis and Machine Intelligence* **27,** 1334–1339. ISSN: 0162-8828 (2005).

69. Chung, J., Chung, M. & O'Leary, D. P. Optimal Filters from Calibration Data for Image Deconvolution with Data Acquisition Error. *Journal of Mathematical Imaging and Vision* **44,** 366–374. ISSN: 0924-9907 (2012).

70. Jorch, H. H. & Campbell, J. L. Analytic Fitting of Full Energy Peaks from Ge(Li) and Si(Li) Photon Detectors. *Nuclear Instruments Methods* **143,** 551–559. ISSN: 0029-554X (1977).

71. Gimenez, E. N. *et al.* Study of charge-sharing in MEDIPIX3 using a micro-focused synchrotron beam. *Journal of Instrumentation* **6,** C01031 (2011).

72. Padgett, R. & Kotre, C. J. Development and application of programs to measure modulation transfer function, noise power spectrum and detective quantum efficiency. *Radiation Protection Dosimetry* **117,** 283–287. ISSN: 0144-8420 (2006).

73. Frojdh, E. *et al.* Count rate linearity and spectral response of the Medipix3RX chip coupled to a 300 mu m silicon sensor under high flux conditions. *Journal of Instrumentation* **9.** ISSN: 1748-0221. doi:10.1088/1748-0221/9/04/c04028 (2014).

74. Fujita, H. *et al.* A Simple Method for Determining the Modulation Transfer-Function in Digital Radiography. *Ieee Transactions on Medical Imaging* **11,** 34–39. ISSN: 0278-0062 (1992).

75. Samei, E., Flynn, M. J. & Reimann, D. A. A method for measuring the presampled MTF of digital radiographic systems using an edge test device. *Medical Physics* **25,** 102–113. ISSN: 0094-2405 (1998).

76. Granton, P. *Slanted Edge Script (2010)* <https://www.mathworks.com/matlabcentral/fileexchange/28631-slant-edge-script/>.

77. Johns, H. E. & Cunningham, J. R. *Physics of Radiology; 4th ed.* (Charles River Media, Hingham, MA, 1983).

78. Mir, J. A. *et al.* Characterisation of the Medipix3 detector for 60 and 80 keV electrons. *Ultramicroscopy* **182,** 44–53. ISSN: 0304-3991 (2017).

79. Raven, C. Numerical removal of ring artifacts in microtomography. *Review of Scientific Instruments* **69,** 2978–2980. ISSN: 0034-6748 (1998).

80. Hainaut, O. *Basic Image Processing (1996)* <`http://www.sc.eso.org/~ohainaut/ccd/`>.

81. Brazilian Synchrotron Light Laboratory. *Sirius: Beamline Project* <`http://www.lnls.cnpem.br/sirius-en/beamlines-projects/`>.

82. Goto, S. Response functions of a Si(Li) detector for photon energies from 1 to 10 keV. *Nuclear Instruments Methods in Physics Research Section a-Accelerators Spectrometers Detectors and Associated Equipment* **333,** 452–457. ISSN: 0168-9002 (1993).

83. Campbell, J. L., McDonald, L., Hopman, T. & Papp, T. Simulations of Si(Li) x-ray detector response. *X-Ray Spectrometry* **30,** 230–241. ISSN: 0049-8246 (2001).